

Kern- und Teilchenphysik

# **Search for couplings of exotic charmonia to light hadron final states involving a $p\bar{p}$ pair at BESIII**

Inaugural-Dissertation  
zur Erlangung des Doktorgrades  
der Naturwissenschaften im Fachbereich Physik  
der Mathematisch-Naturwissenschaftlichen Fakultät  
der Westfälischen Wilhelms-Universität Münster

vorgelegt von  
**MARCEL ANDRE RUMP**  
aus MÜNSTER

Münster 2019



---

Dekan:	Prof. Dr. Gerhard Wilde
Erster Gutachter:	Prof. Dr. Alfons Khoukaz
Zweiter Gutachter:	Prof. Dr. Anton Andronic

Tag der mündlichen Prüfung:

Tag der Promotion:





# Abstract

Based on  $14.7\text{fb}^{-1}$  of data at 17 center-of-mass energies between 3.7730 GeV and 4.5995 GeV collected in  $e^+e^-$  annihilations with the BESIII detector operating at the BEPCII collider in Beijing, a precise determination of Born cross sections of light hadron final states involving a  $p\bar{p}$  pair and a light meson  $m$  was performed.

In the main part of this thesis, a full analysis of the  $p\bar{p}\eta$  and  $p\bar{p}\omega$  states was carried out, including the investigation of statistical and systematic uncertainties. Both the light mesons were reconstructed via their hadronic decays into  $\pi^+\pi^-\pi^0$  and the  $\eta$  meson additionally via its electromagnetic decay into two photons. Reconstruction and selection efficiencies were determined based on an effective partial wave analysis, one of the most sophisticated tools in hadron spectroscopy. Cross sections of the processes  $e^+e^- \rightarrow p\bar{p}m$  were extracted for the first time in this energy regime, utilizing the high luminosity data samples of BESIII. This allowed for the investigation of possible resonant contributions from heavy vector resonances in the charmonium mass region. Since no significant resonant structure above continuum production was found, upper limits were calculated at 90 % confidence level for a variety of different mass and width hypotheses. The most stringent limit was found for an incoherent resonant contribution with mass  $m = 4.176\text{ GeV}/c^2$  and width  $\Gamma = 30\text{ MeV}/c^2$  decaying into  $p\bar{p}\eta$  at a value of 0.42 pb.

In addition, cross sections for the  $p\bar{p}\eta'$  and  $p\bar{p}f_1(1285)$  states have been determined for the first time in this center-of-mass energy region. The  $\eta'$  meson could be clearly identified and it was possible to extract first cross section values. The  $f_1(1285)$  could be identified in the integrated data sample with an overall significance of  $8.6\sigma$ . Individual significant signal contributions were found at 4.0076 GeV and 4.1784 GeV and upper limits were set for all other data sets.



# Contents

<b>1. Introduction</b>	<b>1</b>
<b>2. Theory</b>	<b>5</b>
2.1. Standard Model of Particle Physics . . . . .	5
2.2. Hadron Spectroscopy . . . . .	8
2.2.1. Mesons . . . . .	10
2.2.2. Baryons . . . . .	12
2.2.3. Charmonia . . . . .	13
2.2.4. Exotics . . . . .	13
<b>3. BESIII Experimental Setup</b>	<b>17</b>
3.1. BEPCII Accelerator . . . . .	17
3.2. BESIII Experiment . . . . .	18
3.2.1. Multilayer Drift Chamber (MDC) . . . . .	20
3.2.2. Time-of-Flight System (TOF) . . . . .	21
3.2.3. Electromagnetic Calorimeter (EMC) . . . . .	22
3.2.4. Muon Identifier (MUC) . . . . .	23
3.2.5. Trigger System . . . . .	23
<b>4. Event Selection</b>	<b>25</b>
4.1. Data Samples and Monte Carlo Simulations . . . . .	25
4.2. Initial Track Selection . . . . .	27
4.2.1. Charged Track Selection and Particle Identification . . . . .	27
4.2.2. Photon Candidate Selection . . . . .	29
4.3. Kinematic Fit . . . . .	30
<b>5. Analysis of <math>e^+e^- \rightarrow p\bar{p}\eta</math> and <math>e^+e^- \rightarrow p\bar{p}\omega</math></b>	<b>31</b>
5.1. Background Studies . . . . .	32
5.2. Number of Observed Events . . . . .	38
5.3. Efficiency . . . . .	42
5.4. Partial Wave Analysis . . . . .	42
5.4.1. Basic Concepts and Formalisms . . . . .	42
5.4.2. Analysis Software Package PAWIAN . . . . .	45

5.4.3. PWA Contributions and Results . . . . .	45
5.5. Radiative Correction Factors . . . . .	53
5.6. Born Cross Sections . . . . .	55
5.7. Systematic Uncertainties . . . . .	59
5.7.1. Kinematic Fit . . . . .	59
5.7.2. Signal Region . . . . .	61
5.7.3. Radiative Corrections . . . . .	61
5.7.4. Background Description . . . . .	61
5.8. Cross Check . . . . .	66
5.9. Results . . . . .	70
5.9.1. Upper Limit Determination . . . . .	75
<b>6. Analysis of <math>e^+e^- \rightarrow p\bar{p}\eta'</math> and <math>e^+e^- \rightarrow p\bar{p}f_1</math></b>	<b>77</b>
6.1. Background Studies . . . . .	79
6.2. Number of Observed Events . . . . .	81
6.3. Efficiency . . . . .	83
6.4. Born Cross Sections . . . . .	86
<b>7. Outlook</b>	<b>89</b>
<b>8. Conclusion</b>	<b>91</b>
<b>A. Appendix</b>	<b>95</b>
<b>Bibliography</b>	<b>111</b>
<b>List of Figures</b>	<b>121</b>
<b>List of Tables</b>	<b>125</b>

# 1. Introduction

Over the past century, enormous scientific progress has been achieved, especially in the field of particle physics, through a unique interplay between theory and experiment. It was at the beginning of the 20th century that the idea of atoms as indivisible particles was proven wrong. The discovery of the electron by J. J. Thomson [1], first scattering experiments by E. Rutherford [2] showing a localized central charge within atomic nuclei, as well as the discovery of the neutron by J. Chadwick [3] laid the foundation for what should become one of the most successful branches of natural science. These observations ultimately led to the first quantum theoretical description of atoms consisting of protons and neutrons in the atomic nucleus which itself is surrounded by electrons. Consequently, physicists started questioning whether these particles also have an inner structure. In contrast to the nucleons, i.e., the proton and the neutron, no experimental evidence could be found for inner structure of the electron. Within the following decades, hundreds of new particles were discovered mainly in accelerator-based experiments. This large number of particles called hadrons suggested that these are not elementary particles, but have an inner structure themselves. A first phenomenological model for the classification of hadrons was developed by M. Gell-Mann [4]. In the so-called quark model, hadrons, consisting of quarks and antiquarks, are bound together by the strong interaction. Today, this model is part of the established Standard Model of Particle Physics, a quantum field theory of electroweak and strong interactions. The gravitational force that is not included in the Standard Model is described in Einstein's famous theory of general relativity [5]. Both theories have proven very successful in describing experimental observations, from interactions of subatomic particles to astrophysical phenomena such as gravitational waves [6]. However, many aspects of the Standard Model are not yet fully understood, especially those related to the strong interaction. At low energies, theoretical predictions of Quantum Chromodynamics are technically very challenging. The strength of the coupling simply prohibits the use of perturbation theory and one has to rely on other methods such as lattice calculations.

Within the quark model, strongly interacting particles, i.e., quarks  $q$  and gluons  $g$ , can be bound together into spin-integer mesons and spin-half-integer baryons. The most well-known baryons composed of three quarks are the nucleons, which are the main constituents of all nuclear matter in the universe. On the other hand, the most simple form of a meson consists only of a quark and an antiquark. Combinations of only the

lightest quarks were found, as well as ones including heavier quarks, e.g., a charm quark  $c$ . These so-called D mesons ( $c\bar{q}, \bar{c}q$ ) are of great importance in hadron spectroscopy. Apart from the lightest mesons, there are also flavorless mesons that exclusively contain heavy quarks, such as the charmonia  $c\bar{c}$ . The first charmonium state that was discovered is the  $J/\psi$  [7, 8], the first spin excitation of the  $c\bar{c}$  ground state  $\eta_c$ . In analogy to the already well-known positronium, there unfolded a large spectrum of charmonium states with different masses and widths. In general, states below the  $D\bar{D}$  threshold revealed an almost perfect agreement between theoretical predictions and experimental observations. Above this threshold particles appeared to be much broader, and states like  $\chi_c$  and  $h_c$  are much harder to produce. Until the beginning of the new millennium, it was believed that the whole zoo of existing particles had been well understood.

In 2003, the first exotic meson candidate  $\chi_{c1}(3872)$  [9] has been found, which does not fit the conventional charmonium spectrum. It was observed by the Belle collaboration as a very narrow peak in the invariant mass distribution of the  $\pi^+\pi^-J/\psi$  final state and its decay width is still subject of ongoing investigations. Such narrow resonances above the open charm threshold were not predicted in any conventional theoretical model. Shortly after, another exotic meson candidate  $\psi(4260)$  [10] was discovered by the BaBar collaboration in hadronic transitions to  $J/\psi$ . With the  $Z_c(3900)$  [11, 12], the first charged charmoniumlike state has been reported in  $e^+e^-$  annihilations to  $\pi^+\pi^-J/\psi$ , simultaneously by the Belle and BESIII collaborations. It was seen as a clear enhancement in the  $J/\psi\pi^\pm$  invariant mass, making it undoubtedly exotic. Due to the fact that it carries an electric charge and couples to the charmonium, its minimal quark content was identified as  $c\bar{c}q\bar{q}$ . The plethora of new states has raised the interest in hadron spectroscopy to a new level, both experimentally and theoretically. Various theoretical interpretations have been proposed to classify these states, e.g., as hybrid charmonia ( $c\bar{c}g$ ) [13, 14], tetraquarks ( $qq\bar{q}\bar{q}$ ) [15, 16] or hadronic molecules ( $q\bar{q}q\bar{q}$ ) [17–19], though none of the interpretations is able to describe all of their properties so that their exact composition is still subject of intense debates. A tremendous effort is made by various experiments to search for new particles and to precisely investigate their properties. One of the leading competitors in the field of charmonium spectroscopy is the BESIII experiment. It is operated since 2008 at the BEPCII collider in Beijing, China. Heavy (exotic) vector charmonium resonances can be directly produced in  $e^+e^-$  annihilations, making it the ideal laboratory to study these states in detail. The BESIII collaboration has accumulated high luminosity data in the charmonium mass region at several center-of-mass energies between 3.7730 GeV and 4.5995 GeV. Recent results from BESIII in the channels  $\pi^+\pi^-J/\psi$  [20],  $\pi^+\pi^-\psi(2S)$  [21],  $\pi^+\pi^-h_c$  [22],  $\omega\chi_{c0}$  [23] and  $\pi^+D^0D^{*-}$  [24] have shown that the structure, initially identified as the  $\psi(4260)$  [10, 25–27], actually consists of two structures. The nature of these two states remains unclear for now.

---

One way to gain further understanding of these states is to look for new decay channels, which is the main goal of this thesis. The charmoniumlike state  $\psi(4260)$ , for example, has a coupling to open charm decay modes [13, 28], but a coupling to light hadron final states [13, 29, 30] has not yet been seen. Using the high luminosity data samples collected in  $e^+e^-$  annihilations by the BESIII experiment in the center-of-mass energy range from 3.7730 GeV to 4.5995 GeV, an investigation of the cross section of different light hadron final states involving a  $p\bar{p}$  pair in the form  $e^+e^- \rightarrow p\bar{p}m$  is performed, where  $m$  is a light, unflavored meson. The main part of the analysis presented in this thesis focuses on the precise determination of the Born cross sections  $\sigma^B(e^+e^- \rightarrow p\bar{p}\eta)$  and  $\sigma^B(e^+e^- \rightarrow p\bar{p}\omega)$ . In this context, the tool of partial wave analysis is used for the correct estimation of reconstruction and selection efficiencies. Intermediate states were studied and a cross check was performed with results from a previous analysis of the reaction  $e^+e^- \rightarrow \eta J/\psi$  [31–33]. Additionally, reactions with the pseudoscalar meson  $\eta'$  and the pseudovector meson  $f_1$  are studied. This is the first time these processes are observed in this energy regime. The cross sections are fitted to look for possible  $\psi \rightarrow p\bar{p}m$  decays and upper limits are calculated for different hypotheses of possible resonant contributions from heavy vector resonances.





## 2. Theory

Since the present work exclusively covers topics from one of the most intensely investigated fields, hadron physics, a general understanding of modern particle physics is essential for the experimental analysis that will be described later. The first chapter of this thesis is therefore used to form the theoretical basis, beginning with an introduction to the Standard Model of Particle Physics. As part of this, the concept of hadrons will be explained as well as the associated mesons and baryons.

### 2.1. Standard Model of Particle Physics

The Standard Model is the widely accepted theory of modern particle physics, successfully describing all fundamental interactions except gravity. The gravitational force is described in Einstein's theory of general relativity [5] as a geometric property of spacetime by a set of partial differential equations [34]. Since the relative strength of gravity compared to the other fundamental forces is significantly smaller by many orders of magnitude, it can generally be neglected in particle physics. The other three fundamental interactions, namely the electromagnetic, weak and strong interaction, are incorporated in the Standard Model of Particle Physics [35]. It describes the interactions between elementary particles, i.e., point-like particles with no inner structure. These elementary particles are distinguished by their intrinsic spin, as illustrated in Figure 2.1. Particles with integer spin that obey Bose-Einstein statistics [37,38] are called bosons, while half-odd-integer spin particles obey Fermi-Dirac statistics [39,40] and are called fermions. So far, there are twelve fermions, namely six quarks and six leptons. In addition to each of these twelve particles, there is also an antiparticle with identical mass and spin, but opposite charge-like quantum numbers. Among the leptons, there are three charged particles, the electron  $e$ , the muon  $\mu$  and the tauon  $\tau$ . The remaining three uncharged leptons are the so-called neutrinos ( $\nu_e, \nu_\mu, \nu_\tau$ ), each of which is assigned to one charged lepton, forming a family or generation. Quarks come in six different flavors, which, similar to the classification used for leptons, can be divided into three families: The up and down quark ( $u, d$ ), the charm and the strange quark ( $c, s$ ) as well as the top and bottom quark ( $t, b$ ). Since the Standard Model is a relativistic quantum field theory [41], interactions between these elementary particles are described by the exchange of force-mediating particles, the gauge bosons. Photons, the exchange bosons of the

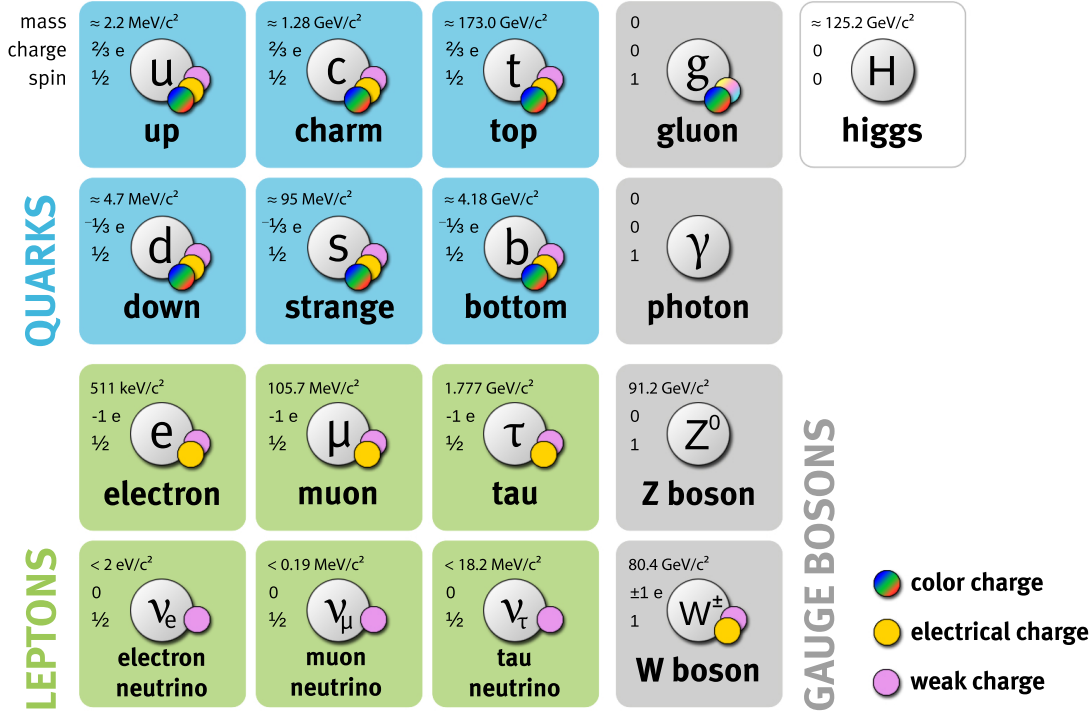


**Figure 2.1.:** Schematic illustration of the Standard Model of Particle Physics, including twelve fermions, namely six quarks and six leptons, the exchange bosons of the electromagnetic, weak and strong interaction as well as the recently discovered Higgs boson. Charges of each elementary particle are represented by differently colored circles. Values are taken from [36].

electromagnetic interaction, couple to the electric charge. This coupling is mathematically described in the theory of Quantum Electrodynamics (QED). The QED Lagrangian, *that can account for nearly all observed phenomena from macroscopic scales down to  $10^{-13}$  cm* [41], is given by

$$\mathcal{L}_{\text{QED}} = \bar{\psi}(i\gamma^\mu D_\mu - m)\psi - \frac{1}{4}F_{\mu\nu}F^{\mu\nu}, \quad (2.1)$$

with Dirac matrices  $\gamma^\mu$ , the gauge covariant derivative  $D_\mu = \partial_\mu + iqA_\mu$  and the electromagnetic field strength tensor  $F_{\mu\nu} = \partial_\mu A_\nu - \partial_\nu A_\mu$ , where  $A_\mu$  is the electromagnetic vector potential,  $q$  is the electric charge and  $\psi$  the bispinor field of a fermion. In 1965, the Nobel Prize in Physics was jointly awarded to Shin'ichirō Tomonaga [42], Julian S. Schwinger [43, 44] and Richard P. Feynman [45–47] for their fundamental work on Quantum Electrodynamics and to overcome the problem of infinities by renormalization. In contrast to the massless photon, there are three massive exchange bosons of the weak interaction, the  $W^\pm$  with  $m_{W^\pm} = 80.379(12) \text{ GeV}/c^2$  and the  $Z^0$  with  $m_{Z^0} = 91.1876(21) \text{ GeV}/c^2$  [36], which couple to the weak isospin  $T$  of a particle. Fermions with negative chirality (left-handed) and antifermions with positive chirality (right-

handed) have  $T = \frac{1}{2}$ . However, right-handed fermions and left-handed antifermions have  $T = 0$  and do not undergo weak interactions. Due to the large masses, the weak interaction is limited to very short distances, while the electromagnetic force acts on infinite ranges. Still it is possible to describe them in a unified way. Sheldon L. Glashow [48], Abdus Salam [49] and Steven Weinberg [50] were honored with the Nobel Prize of Physics 1979 for their unified theory of the electroweak interaction.

Gauge bosons with a non-zero mass can be explained by coupling to an additional complex scalar field, the Higgs field [51, 52]. Spontaneous symmetry breaking, in the case of  $W^\pm$  and  $Z^0$  the electroweak symmetry breaking, causes the bosons to acquire mass by interacting with the Higgs field, which has a non-vanishing vacuum expectation value. This mechanism implied the existence of a scalar Higgs boson, first observed in 2012 by the ATLAS [53] and CMS [54] experiments at the Large Hadron Collider (LHC). Shortly after the discovery of this particle, the Nobel Prize in Physics 2013 was awarded to François Englert and Peter W. Higgs for the theoretical description of the Higgs mechanism.

The third and last interaction within the Standard Model is the strong interaction described by Quantum Chromodynamics (QCD). The gauge bosons of the strong interaction are the gluons which couple to the color charge. Three color charges exist, red, green and blue, as well as three corresponding anticolors. A unique property of quarks is that they do not exist as isolated particles, but exclusively in color-neutral systems, a phenomenon called confinement. The Lagrangian of QCD [36] is given by

$$\mathcal{L}_{\text{QCD}} = \sum_q \bar{\psi}_{q,a} (i\gamma^\mu \partial_\mu \delta_{ab} - g_s \gamma^\mu t_{ab}^C \mathcal{A}_\mu^C - m_q \delta_{ab}) \psi_{q,b} - \frac{1}{4} F_{\mu\nu}^A F^{A\mu\nu}, \quad (2.2)$$

where  $\psi_{q,a}$  are quark-field spinors for a quark of flavor  $q$ , mass  $m_q$  and color  $a$ . In general, the interaction of gluons with a quark can be interpreted as the rotation of the quark's color in  $\text{SU}(3)$  color space, a special unitary group of the underlying gauge theory. The  $t_{ab}^C$  are the generators of this group, a set of  $3 \times 3$  matrices, where  $C$  runs from 1 to 8. The  $\mathcal{A}_\mu^C$  correspond to the eight gluon fields,  $g_s$  is the coupling constant of QCD and  $F_{\mu\nu}^A$  is the gluon field tensor given by

$$F_{\mu\nu}^A = \partial_\mu \mathcal{A}_\nu^A - \partial_\nu \mathcal{A}_\mu^A - g_s f_{ABC} \mathcal{A}_\mu^B \mathcal{A}_\nu^C, \quad (2.3)$$

where  $f_{ABC}$  are the structure constants. The last term allows for gluon self-interactions, which is not permitted in QED. While photons are electrically neutral, gluons carry color charge themselves. Due to this gluon-gluon coupling, the effective range of the strong force

is limited to very short distances, even though gluons are massless particles. An empirical parameterization of the QCD potential in first order of perturbation theory is given by

$$V(r) = -\frac{4}{3} \cdot \frac{\alpha_s(r)\hbar c}{r} + k \cdot r \quad \text{with} \quad \alpha_s(Q^2) = \frac{12\pi}{(33 - 2n_f) \cdot \ln(Q^2/\Lambda^2)}, \quad (2.4)$$

where  $\alpha_s$  is the coupling constant,  $n_f$  is the number of quark flavors and  $\Lambda$  a scale parameter. Unlike the coupling constant of the electromagnetic interaction  $\alpha \approx \frac{1}{137}$ ,  $\alpha_s$  strongly depends on the four-momentum transfer  $Q$ . At large values of  $Q^2 \gg \Lambda^2$  the strong coupling becomes very small and the quarks can be considered as quasi-free particles, which is called asymptotic freedom. In 2004, the Nobel Prize in Physics was jointly awarded to David J. Gross, Frank Wilczek [55] and H. David Politzer [56] for the discovery of asymptotic freedom in the theory of the strong interaction. On the other side, for small  $Q^2$ , i.e., large distances  $r$ , the potential increases linearly. Thus, separating quarks requires increasing amounts of energy. At a certain point the energy is large enough to produce additional quark antiquark pairs from the vacuum, which is known as hadronization. The Standard Model, as a quantum field theory of almost everything [57], has proved very successful in providing self-consistent experimental predictions and should eventually be complemented by the incorporation of a quantum field theory of gravity. But there are phenomena that cannot be explained with the Standard Model, such as neutrino oscillations [58] and the existence of dark matter [59] with associated astrophysical observations, such as rotational curves of galaxies [60] or gravitational lensing [61]. These beyond standard model phenomena are among the most intensively studied topics in modern particle physics.

## 2.2. Hadron Spectroscopy

As briefly mentioned in the previous chapter, quarks and gluons are confined to color-neutral states, so-called hadrons. Color neutrality can be achieved either by the combination of all three color charges or by combining a color and its corresponding anticolor. Apart from color confinement, there are no further restrictions on how strongly interacting elementary particles can be combined into hadrons. An essential part of hadron spectroscopy is to characterize these states very precisely and to provide important information for tests of QCD in the non-perturbative regime. There are several approaches that try to solve QCD to make predictions about physical quantities, such as Lattice QCD [62], quark model [4] and QCD sum rules [63]. Within the quark model, hadrons are usually classified according to their valence quarks, the quarks and antiquarks which give rise to a series of quantum numbers, the total angular momentum  $J$ , parity  $P$ , charge conjugation  $C$ , baryon number  $\mathcal{B}$  as well as flavor quantum numbers, the strong isospin  $I$ ,

strangeness  $S$ , charm  $C$ , bottomness  $B$  and topness  $T$ . A parity transformation reverses spatial coordinates  $\mathbf{x}$  so that

$$\hat{P}\psi(t, \mathbf{x}) = \psi(t, -\mathbf{x}) , \quad (2.5)$$

where  $\hat{P}$  is the parity operator acting on the wave function  $\psi$  of a particle. By convention, quarks have positive parity, while antiquarks have negative parity. The charge conjugation operator  $\hat{C}$  transforms all particles into their corresponding antiparticles  $\hat{C}\psi = \bar{\psi}$ , and thus changes the sign of all charges. Beside these multiplicative quantum numbers, quarks have the additive baryon number  $\mathcal{B} = \frac{1}{3}$ , while antiquarks have  $\mathcal{B} = -\frac{1}{3}$ , as well as additive flavor quantum numbers for the three generations of quarks. Thus, states with baryon number  $\mathcal{B} = 1$  are called baryons, whereas states with  $\mathcal{B} = 0$  are called mesons. For the sake of simplicity, all but the two simplest types of hadrons ( $q\bar{q}, qq\bar{q}$ ) will be referred to as exotic. Due to the similar masses of up and down quarks, an isospin symmetry is introduced. The two quarks can be distinguished by their third component of the isospin  $I$ , where the up quark has  $I_3 = +\frac{1}{2}$  and the down quark has  $I_3 = -\frac{1}{2}$ . By convention, the flavor of a quark has the same sign as its electrical charge  $Q$  [36]. Therefore, the strange quark has strangeness  $S = -1$ , the charm quark has  $C = 1$ , the bottom quark has  $B = -1$  and the top quark has  $T = 1$ , as summarized in Table 2.1. Over the past decades, a whole zoo of new particles has been discovered. Most of these particles could be identified as mesons or baryons, whose classification within the quark model is described in the following chapters. However, QCD theoretically allows for particle compositions of quarks and even gluonic degrees of freedom other than mesons and baryons, which will also be discussed in more detail.

**Table 2.1.:** Additive quantum numbers of the quarks: Electrical charge  $Q$ , isospin  $I$  and its third component  $I_3$ , strangeness  $S$ , charm  $C$ , bottomness  $B$  and topness  $T$ .

	d	u	s	c	b	t
$Q$	$-\frac{1}{3}$	$+\frac{2}{3}$	$-\frac{1}{3}$	$+\frac{2}{3}$	$-\frac{1}{3}$	$+\frac{2}{3}$
$I$	$\frac{1}{2}$	$\frac{1}{2}$	0	0	0	0
$I_3$	$-\frac{1}{2}$	$+\frac{1}{2}$	0	0	0	0
$S$	0	0	-1	0	0	0
$C$	0	0	0	+1	0	0
$B$	0	0	0	0	-1	0
$T$	0	0	0	0	0	+1

### 2.2.1. Mesons

In the quark model, mesons are quark-antiquark ( $q\bar{q}$ ) bound states. A state is usually classified using the spectroscopic notation  $J^{PC}$ , which contains information about its quantum numbers. The total angular momentum  $J$  is given by  $|L - S| \leq J \leq |L + S|$ , where spin  $S$  is 0 (antiparallel quark spins) or 1 (parallel quark spins) and  $L$  is the orbital angular momentum of the quark-antiquark pair. Eigenvalues of the parity and charge conjugation operators are given by  $P = (-1)^{L+1}$  and  $C = (-1)^{L+S}$ , respectively.  $C$  parity can be generalized to the  $G$  parity for mesons with isospin  $I = 1$  or  $I_3 = 0$  [36]. The operator  $\hat{G}$  is given by

$$\hat{G} = \hat{C}e^{i\pi\hat{I}_2}, \quad (2.6)$$

where  $I_2$  is the second component of the isospin and eigenvalues are  $G = (-1)^{I+L+S}$ . Additionally, mesons can be distinguished by their quark content, e.g., their isospin or strangeness. Considering only the three lightest quarks ( $u, d, s$ ), nine  $q\bar{q}$  combinations can be formed. Following  $U_L(3) \times U_R(3)$  symmetry, they are grouped into an octet and a singlet  $\mathbf{3} \otimes \bar{\mathbf{3}} = \mathbf{8} \oplus \mathbf{1}$ . The multiplet of the pseudoscalar mesons with  $J^{PC} = 0^{-+}$  is graphically depicted in Figure 2.2. Within this  $SU(3)$  representation, the quark content of the kaons ( $K^+, K^-, K^0, \bar{K}^0$ ) and the charged pions ( $\pi^+, \pi^-$ ) can be easily identified

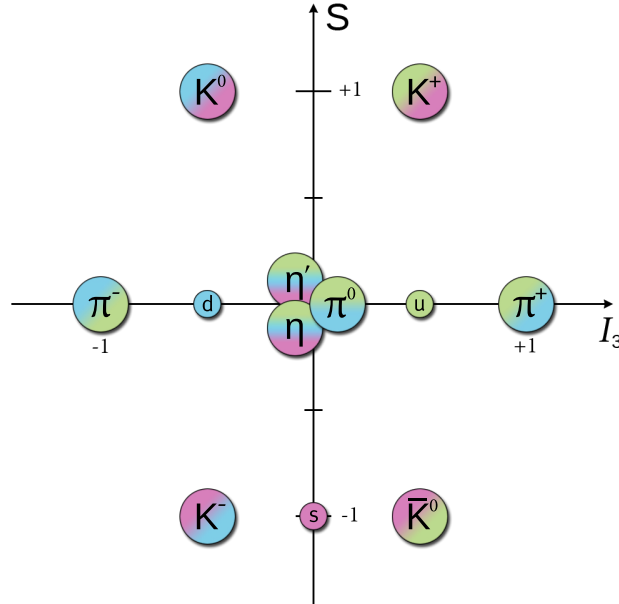


**Figure 2.2.:** Schematic representation of the nonet of pseudoscalar mesons,  $q\bar{q}$  pairs with  $J^{PC} = 0^{-+}$ , depending on the third component of their isospin  $I_3$  (abscissa) and their strangeness  $S$  (ordinate). Colors indicate different quark flavors of the three lightest quarks,  $u$  (green),  $d$  (blue) and  $s$  (magenta). The three mesons in the center ( $I_3 = 0$ ) are mixtures of  $u\bar{u}$ ,  $d\bar{d}$  and  $s\bar{s}$ , while the other six mesons are quark-antiquark combinations with different flavors.

**Table 2.2.:** Quark content of the lightest pseudoscalar mesons  $\mathbf{m}$ , where  $\psi_f$  is the flavor wave function.

$\mathbf{m}$	$\psi_f$
$\pi^+$	$u\bar{d}$
$\pi^-$	$d\bar{u}$
$K^+$	$u\bar{s}$
$K^-$	$s\bar{u}$
$K^0$	$d\bar{s}$
$\bar{K}^0$	$s\bar{d}$
$\pi^0$	$\frac{1}{\sqrt{2}}(u\bar{u} - d\bar{d})$
$\eta_8$	$\frac{1}{\sqrt{6}}(u\bar{u} + d\bar{d} - 2s\bar{s})$
$\eta_1$	$\frac{1}{\sqrt{3}}(u\bar{u} + d\bar{d} + s\bar{s})$

as listed in Table 2.2. The remaining pseudoscalar mesons ( $\pi^0$ ,  $\eta_8$ ,  $\eta_1$ ) share the same quantum numbers ( $I_3, S$ ) and can be mixtures of  $u\bar{u}$ ,  $d\bar{d}$  and  $s\bar{s}$ . In general, particles with open strangeness like the charged kaons are much heavier ( $m_{K^\pm} = 493.677(16) \text{ MeV}/c^2$ ) than particles without, such as the charged pions ( $m_{\pi^\pm} = 139.57061(24) \text{ MeV}/c^2$ ) [36]. Since the  $\pi^0$  is the lightest meson ( $m_{\pi^0} = 134.9770(5) \text{ MeV}/c^2$ ) [36], it is assumed that it contains no  $s\bar{s}$  contribution. Its flavor wave function can be written as

$$\psi_{\pi^0} = \frac{1}{\sqrt{2}}(u\bar{u} - d\bar{d}) , \quad (2.7)$$

and the remaining two SU(3) wave functions can be defined to be orthogonal to the others given by

$$\psi_8 = \frac{1}{\sqrt{6}}(u\bar{u} + d\bar{d} - 2s\bar{s}) \quad \text{and} \quad \psi_1 = \frac{1}{\sqrt{3}}(u\bar{u} + d\bar{d} + s\bar{s}) . \quad (2.8)$$

However, the physically observed  $\eta$  and  $\eta'$  mesons are mixtures of these two states and can be described by

$$\begin{pmatrix} \psi_\eta \\ \psi_{\eta'} \end{pmatrix} = \begin{pmatrix} \cos \theta_P & -\sin \theta_P \\ \sin \theta_P & \cos \theta_P \end{pmatrix} \cdot \begin{pmatrix} \psi_8 \\ \psi_1 \end{pmatrix} . \quad (2.9)$$

where the pseudoscalar mixing angle  $\theta_P$  is measured to be between  $-10^\circ$  and  $-20^\circ$  [36]. Besides the pseudoscalar mesons, which can be regarded as  $q\bar{q}$  ground states, also meson excitations exist with different quantum numbers, e.g., higher spin  $S$  or orbital momentum  $L$  as well as radial excitations denoted by the principal quantum number  $n$ . Coupling a quark-antiquark pair with parallel spin alignment creates a multiplet of vector mesons ( $J^{PC} = 1^{--}$ ). Comparing these states to the pseudoscalar mesons, pions are replaced by the  $\rho$  mesons and kaon excitations are marked with an asterisk  $K^*$ .

Similar to the  $\eta$  and  $\eta'$  mesons, the  $\phi$  and  $\omega$  mesons are mixtures of the octet and singlet states. However, the vector meson mixing angle  $\theta_V$  is nearly ideal, i.e., the  $\phi$  is almost a pure  $s\bar{s}$  state. Adding one heavier quark (c, b) one obtains the so-called D or B mesons. Due to the large mass difference of the quarks, it is significantly easier to identify mesons that contain at least one heavier quark. The D mesons are of great importance for charmonium spectroscopy and the investigation of exotic charmonia, which will be described in the upcoming sections.

### 2.2.2. Baryons

In general, baryons are composed of three quarks and therefore have half-odd-integer spin and baryon number  $\mathcal{B} = 1$ . Considering only the three lightest quarks, the flavor wave functions of baryon states can be constructed as members of multiplets  $\mathbf{3} \otimes \mathbf{3} \otimes \mathbf{3} = \mathbf{10} \oplus \mathbf{8} \oplus \mathbf{8} \oplus \mathbf{1}$ , as illustrated in Figure 2.3 for the  $J^P = \frac{3}{2}^+$  decuplet and the  $J^P = \frac{1}{2}^+$  octet. The baryon octet contains the nucleons N, i.e., the proton p (uud) and the neutron n (udd), which are the main constituents of all nuclear matter in the universe. Similar to mesons, there is a rich spectrum of excited baryon states. Although many of these resonances are already known, the fundamental degrees of freedom underlying the baryon excitation spectrum are still poorly understood [64].

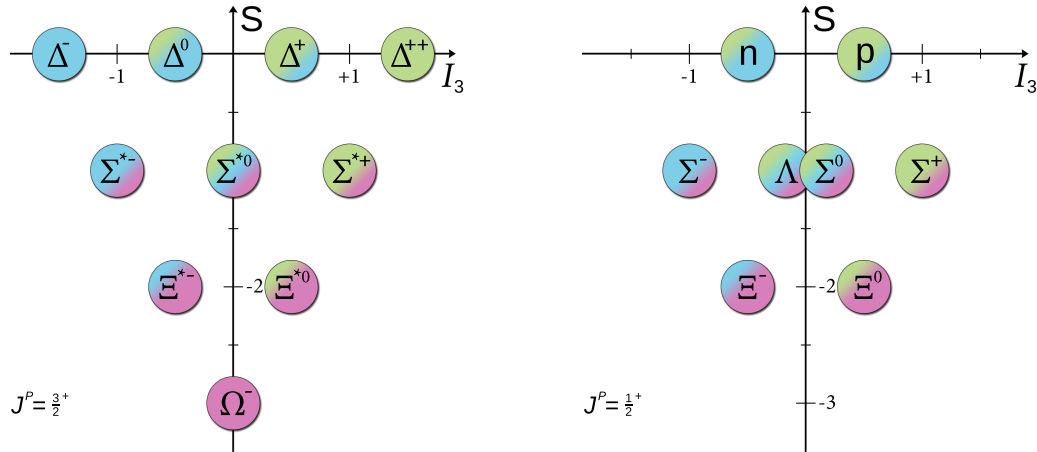


**Figure 2.3.:** Schematic representation of the baryon decuplet (**left**) and the baryon octet (**right**), combinations of three quarks (qqq) with  $J^P = \frac{3}{2}^+$  and  $J^P = \frac{1}{2}^+$ , respectively. The third component of the isospin  $I_3$  is shown on the abscissa and the strangeness  $S$  on the ordinate. Colors indicate different quark flavors of the three lightest quarks, u (green), d (blue) and s (magenta).



### 2.2.3. Charmonia

Apart from the mesons discussed so far, there are also flavorless mesons that exclusively contain heavy quarks. In analogy to the positronium, these  $q\bar{q}$  states are called quarkonium, that is, e.g., charmonium ( $c\bar{c}$ ) and bottomonium ( $b\bar{b}$ ). An equivalent toponium state does not exist. Due to its high mass, the top quark decays very quickly through the weak interaction before a bound state can be formed. Two well-known examples for charmonia are the ground state  $\eta_c$  ( $0^{-+}$ ) and the vector charmonium  $J/\psi$  ( $1^{--}$ ). The latter was the first charmonium state to be experimentally observed in 1974, simultaneously by Burton Richter [7] and Samuel C. C. Ting [8]. It is also the longest living charmonium state with a mean lifetime of  $7.1(2) \times 10^{-21}$  s, i.e., it has a very narrow decay width of 92.9(28) keV [36] due to the so-called OZI rule, a consequence of quantum chromodynamics [65–68]. Above the open charm threshold, charmonium states can decay strongly into a pair of D mesons by spontaneous creation of a light quark-antiquark pair. Below this threshold, the decay proceeds mainly via the exchange of three gluons and is therefore OZI-suppressed by the characteristic form of the QCD coupling constant and the higher number of interaction vertices. The  $J/\psi$  meson can be directly produced in  $e^+e^-$  annihilations via a virtual photon, ideal for the investigation of light hadron spectroscopy with experiments such as BESIII, which recently finished accumulating the world’s largest  $J/\psi$  resonance data set of about 10 billion events [69]. Above these two resonances unfolds a large spectrum of charmonium states, as graphically depicted in Figure 2.4, which cover the mass range from  $\sim 3$  to  $5 \text{ GeV}/c^2$  and is therefore an ideal probe for investigations of the transition region between perturbative and non-perturbative QCD. Aside from the experimentally confirmed charmonia, there are still some states which are theoretically predicted in the non-relativistic quark model [70], but which have not yet been discovered. Moreover, recent observations have shown states that do not fit the conventional charmonium spectrum. One way to describe these are so-called exotic mesons, which will be discussed in the upcoming section.

### 2.2.4. Exotics

As previously mentioned, QCD theoretically allows for particle compositions of more than two or three quarks. Examples for these exotic hadrons are tetraquarks ( $qq\bar{q}\bar{q}$ ), molecules ( $q\bar{q}q\bar{q}$ ) or pentaquarks ( $qqqq\bar{q}$ ). Due to gluon-gluon interactions, even systems with constituent gluonic degrees of freedom are possible, such as hybrids ( $q\bar{q}g$ ) as well as glueballs, consisting purely of gluons ( $gg, ggg, \dots$ ). Within the last two decades, several exotic meson candidates have been observed, such as the  $\chi_{c1}(3872)$  [9] and  $\psi(4260)$  [10], which do not fit the conventional charmonium spectrum. Although mainly seen via initial-state radiation processes in hadronic transitions to  $J/\psi$  and  $\psi'$ , most of their features

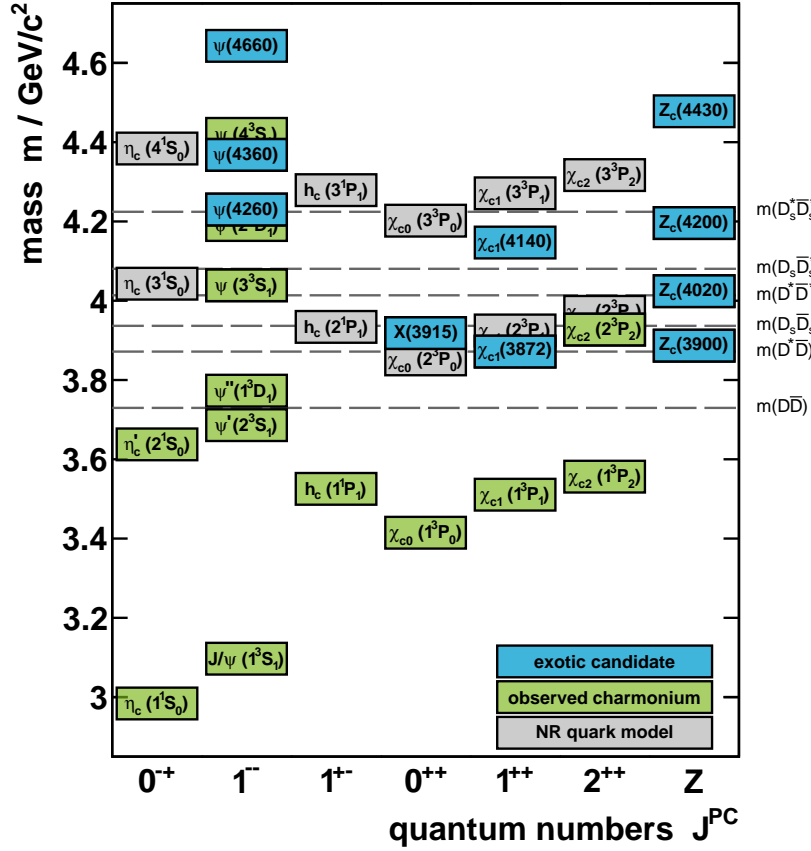


**Figure 2.4.:** Schematic representation of the charmonium spectrum in the mass region available at BESIII with quantum numbers in spin-parity notation  $J^{PC}$ . Charged charmoniumlike states  $Z$  are shown in a separate column, since they are not conventional charmonium states ( $c\bar{c}$ ). States predicted in the non-relativistic quark model but not yet discovered are represented by gray boxes. Experimentally confirmed states are shown by green boxes, while blue boxes represent exotic candidates that do not fit the conventional charmonium spectrum. Dashed lines indicate different open charm thresholds.

exclude interpretations as excited charmonium states. In general, conventional vector charmonia above the open charm threshold are expected to have significant coupling to open charm decay modes. While the  $\psi''$ , for example, decays almost exclusively into a pair of D mesons, the  $\psi(4260)$  does not [36]. Many different models have been proposed to interpret the  $\psi(4260)$  as a tetraquark [16], a hadronic molecule of  $\bar{D}D^*$  [71] or  $\omega\chi_{c0}$  [72], a hybrid state [14] or just an interference effect [73]. However, the question of whether these mesons are tetraquarks, molecules or hybrids is subject to intense debates, and the nature of these states remains unclear for now. One way to further classify these states is to study their properties, for example by looking for different decay channels, which is the main goal of this work.

With the  $Z_c(3900)$ , the first charged charmoniumlike state has been found [11, 12]. The fact that it carries an electric charge and couples to charmonium makes it undoubtedly exotic. Another clearly exotic state would be one that carries exotic quantum numbers, e.g.,  $0^{--}$ ,  $0^{+-}$ ,  $1^{-+}$  and  $2^{+-}$ , which cannot be constructed for a conventional quark-antiquark pair. The plethora of new states has raised the interest in hadron spectroscopy to a new level, both experimentally and theoretically. A tremendous effort is made by various experiments to search for new particles and to precisely investigate their properties [74, 75]. One of them is the BESIII experiment [76] which will be presented in the following chapter.



### 3. BESIII Experimental Setup

The data sets that were analyzed in this work have been collected with the BEijing Spectrometer (BESIII), an upgrade of the former experiments BES and BESII located at the Beijing Electron-Positron Collider II (BEPCII). The accelerator, detector components as well as the trigger system used for the acquisition of huge amounts of data are explained in more detail in the following sections.

#### 3.1. BEPCII Accelerator

BEPCII is a major upgrade from its predecessor BEPC at the Institute of High Energy Physics (IHEP) in Beijing, China. After four years (2004-2007) of construction and commissioning [77], the symmetric double-ring  $e^+e^-$  collider was installed, serving as a collider for high-energy physics and as a synchrotron radiation source. Both electrons and positrons are pre-accelerated to energies between 1.89 GeV and 2.5 GeV by a linear accelerator with a length of 202 m and then injected into two separate storage rings. The beams are brought to collision under a small angle of  $2 \times 11$  mrad at a well-defined interaction point (IP) which is surrounded by the BESIII detector. Two distinct beam pipes are used to maintain beam currents of up to 910 mA with 93 bunches per beam, necessary to achieve the design luminosity of  $1 \cdot 10^{33} \text{ cm}^{-2} \text{ s}^{-1}$  at a beam energy

**Table 3.1.:** Relevant operational parameters of BEPCII compared to its predecessor BEPC [78].

Parameter	Unit	BEPCII	BEPC
Center-of-mass energy	GeV	2 – 4.6	2 – 5
Circumference	m	237.5	240.4
Peak luminosity (at $2 \times 1.89$ GeV)	$\text{cm}^{-2} \text{s}^{-1}$	$\sim 10^{33}$	$\sim 10^{31}$
Number of bunches		$2 \times 93$	$2 \times 1$
Beam current	A	$2 \times 0.91$	$2 \times 0.035$
Bunch spacing	m/ns	2.4/8	–
Bunch length $\sigma_z$	cm	1.5	$\sim 5$
Bunch size ( $\sigma_x \times \sigma_y$ )	$\mu\text{m} \times \mu\text{m}$	$\sim 380 \times 5.7$	$\sim 840 \times 37$
Relative energy spread		$5 \cdot 10^{-4}$	$5 \cdot 10^{-4}$
Crossing angle	mrad	$\pm 11$	–

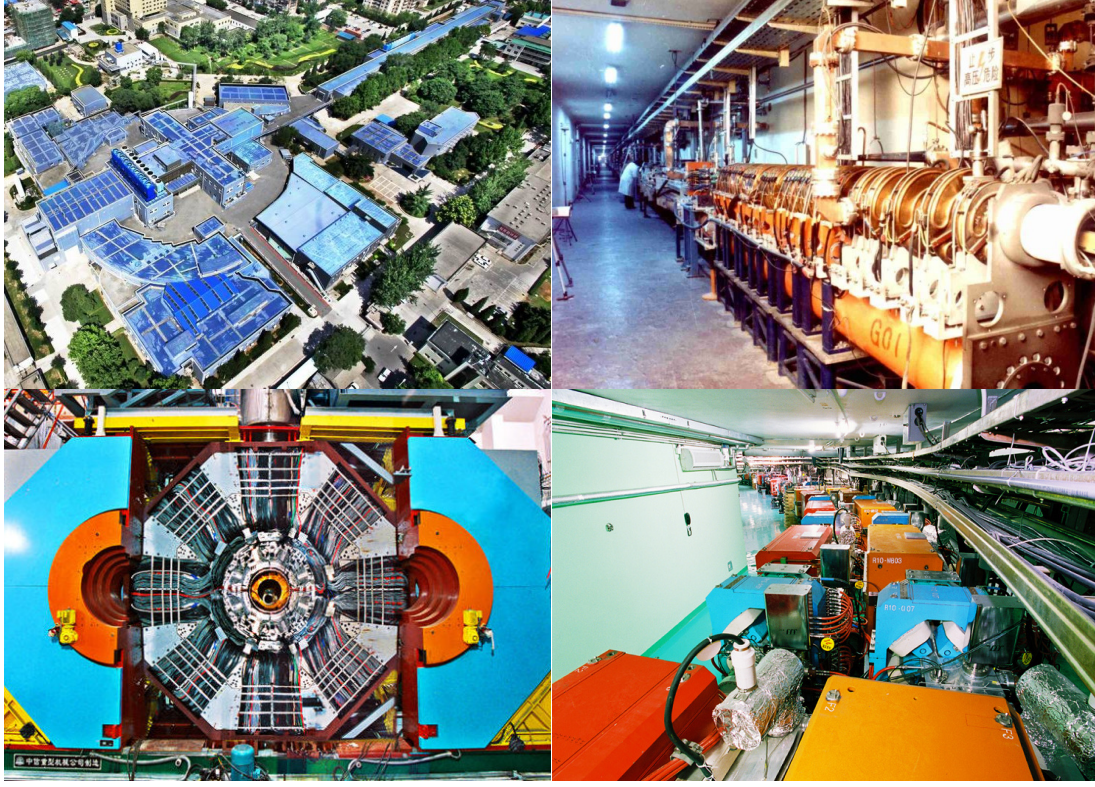


**Figure 3.1.:** Pictures of the BESIII and BEPCII facilities. An overview of the experimental site (**top left**), the linear accelerator (**top right**) and the two storage rings (**bottom right**) as well as the front view of the BESIII detector (**bottom left**). Images are taken from [79, 80].

of 1.89 GeV corresponding to the center-of-mass energy of the  $\psi(2S)$  and to meet the requirements for the BESIII physics program [76, 78]. An overview of the BEPCII facility is shown in Figure 3.1 and relevant operational parameters are summarized in Table 3.1.

## 3.2. BESIII Experiment

With the improvements to the BEPC collider, the former BESII detector has also been upgraded to take full advantage of the increased luminosity of BEPCII. The BESIII detector was completely redesigned and constructed with advanced detection and computation technologies [78] providing 93% geometrical acceptance of the full solid angle. It is composed of four main components: A small-cell, helium-based (60 % He, 40 %  $C_3H_8$ ) multilayer drift chamber (MDC) surrounded by a solenoid magnet that provides a 1 T magnetic field within the tracking volume. The time-of-flight system (TOF) based on plastic scintillators. An electromagnetic calorimeter (EMC) to measure photons and the muon identifier (MUC) to effectively distinguish muons from charged pions and other

hadrons. In experiments like BESIII, where the center-of-mass system of the projectiles is approximately at rest, detector components are arranged cylindrically symmetric around the interaction point. Figure 3.2 shows a schematic drawing of the BESIII detector and its components, which will be further described in the upcoming sections. All detector specific parameters as well as a much more detailed description of the components can be found in the design and construction report by the BESIII collaboration [78].

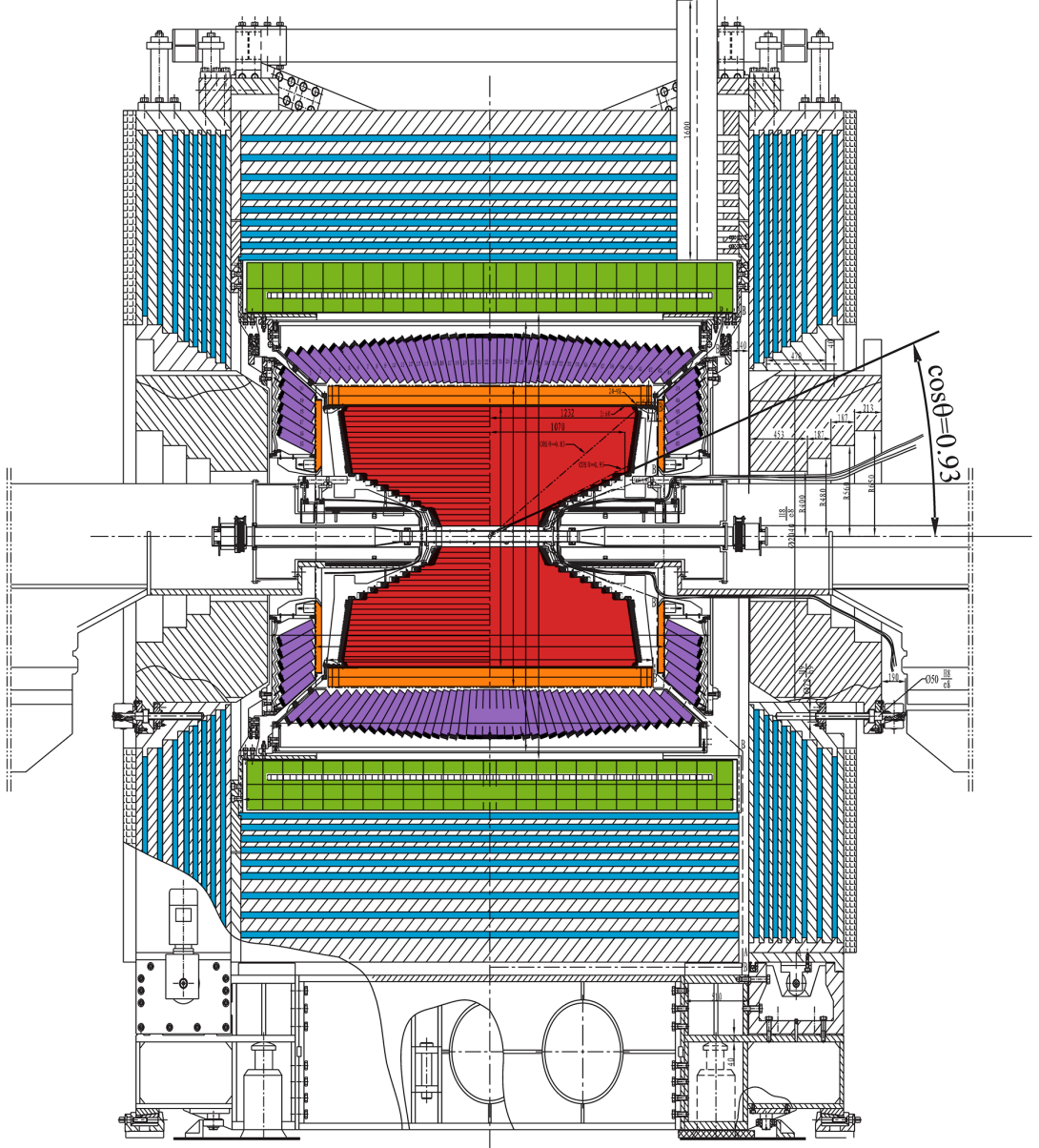


**Figure 3.2.:** Schematic drawing of the BESIII detector and its main components, the multilayer drift chamber (**red**), time-of-flight system (**orange**), electromagnetic calorimeter (**purple**), the superconducting solenoid magnet (**green**) and the muon identifier (**blue**). The beam line goes horizontally through the central part of the detector. Image edited from its original version [78].



### 3.2.1. Multilayer Drift Chamber (MDC)

The MDC is the innermost component of the detection system. After penetrating the beryllium beam pipe, particles produced in  $e^+e^-$  annihilations traverse the main drift chamber, a cylindrical chamber used to measure momentum and energy of electrically charged particles. The chamber has an inner radius of 59 mm, an outer radius of 810 mm and a maximum length of 2.582 m. The end plates of the chamber have a stepped conical shape to make space for the beam focusing quadrupoles. With this geometry, a minimal polar angle coverage of  $|\cos\vartheta| \leq 0.83$  and a solid angle coverage of  $\Delta\Omega/4\pi = 93\%$  is achieved. The chamber is divided into 43 layers of small drift cells, containing a total of 6796 sense wires and 21844 additional field wires. Sense wires are made of gold plated tungsten-rhenium with a diameter of  $25\mu\text{m}$  and are arranged with specific alternating orientations to allow for a three-dimensional track reconstruction, as visualized in Figure 3.3. Gold plated aluminium field wires with a diameter of  $110\mu\text{m}$  are used to form a homogeneous electric field. The volume is filled with a gas mixture of helium (60 %) and propane  $\text{C}_3\text{H}_8$  (40 %), which is ionized along the trajectory of the charged particles passing through the detector. Ions and electrons start drifting within the electric field and produce electric signals at the corresponding wires. The momentum  $p$  of a charged particle can be calculated from the curvature of its trajectory within a 1 T magnetic field. The momentum resolution is mainly determined by two factors: multiple scattering on the material inside the drift chamber volume and the single sense wire

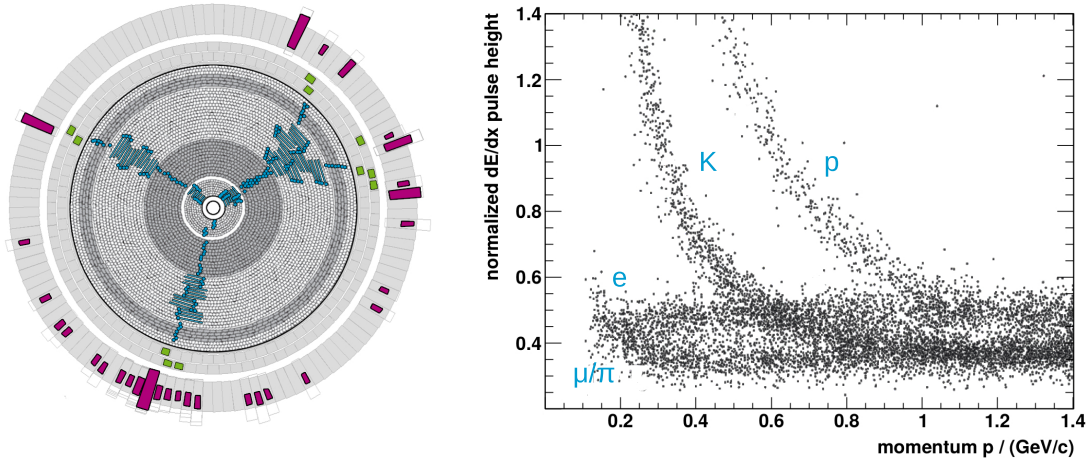


**Figure 3.3.:** **Left:** Visualization of hits in  $xy$  plane of the inner detection systems of BESIII for a simulation of the reaction  $e^+e^- \rightarrow p\bar{p}\eta$  within the BESIII Event Display framework. MDC sense wire signals along trajectories of charged particles (blue), time-of-flight signals (green) and energy deposits in crystals of the electromagnetic calorimeter (magenta) are shown. **Right:** Specific energy loss  $dE/dx$  in the MDC versus incident momentum of charged particles used for particle identification. Image edited from its original version [81].



position resolution. Multiple scattering is minimized by the use of thin field wires and a specific helium-based gas mixture with a radiation length of 550 m. The single wire position resolution is expected to be  $\sim 130 \mu\text{m}$  in  $r\varphi$  plane and  $\sim 2 \text{ mm}$  in  $z$  direction, which gives a momentum resolution of  $\sigma_p/p < 0.5\%$  at  $1 \text{ GeV}/c$ . MDC information is also used to distinguish between different types of particles. There are mainly five types of charged particles that can be considered stable within the dimensions of the MDC, i.e., electrons  $e^\pm$ , muons  $\mu^\pm$ , pions  $\pi^\pm$ , kaons  $K^\pm$  and protons  $p$  or antiprotons  $\bar{p}$ . The electric charge of a particle can be easily identified by the curvature of its trajectory in the magnet field. Measuring the specific energy loss  $dE/dx$  of a particle within the gas volume helps to identify the particle species. A simulation of the normalized pulse height of MDC wire signals, which is directly proportional to the energy loss of a particle, is shown in Figure 3.3. Protons can be clearly separated from all other particles up to a momentum of  $\sim 1 \text{ GeV}/c$ . Pions can be isolated from electrons above  $0.4 \text{ GeV}/c$  and a  $3\sigma$   $\pi/K$  separation is achieved up to  $0.6 \text{ GeV}/c$ .

### 3.2.2. Time-of-Flight System (TOF)

The TOF is used as a supplementary detection system to improve the particle identification efficiency. It is divided into a barrel part and two endcaps, mounted directly on the outside of the MDC. The barrel part consists of two layers, each with 88 plastic scintillation bars of  $2.3 \text{ m}$  length and a trapezoidal cross section with a thickness of  $50 \text{ mm}$ . Photomultipliers are attached to both ends, providing a dual side readout of the scintillation light produced in each TOF segment. Furthermore, the two layers are offset to prevent gaps between the detection elements, covering a polar angle range of  $|\cos\vartheta| < 0.83$ . The two endcaps contain only a single layer of 48 fan-shaped scintillation counters,  $480 \text{ mm}$  in length and  $50 \text{ mm}$  thick. They are read out by a single photomultiplier tube attached to the far end of each segment. Thus, the endcaps cover the polar angle regions with  $0.85 < |\cos\vartheta| < 0.95$ . A small gap between barrel and endcaps is needed for the mechanical support frame of the MDC. Achieved time resolutions in the barrel and end cap regions are  $\sigma_t \approx 100 \text{ ps}$  and  $\sigma_t \approx 110 \text{ ps}$ , respectively. The mass  $m$  of a charged particle can be calculated [81] by

$$m^2 = p^2 \cdot \frac{1 - \beta^2}{\beta^2} \quad \text{with} \quad \beta = \frac{L}{ct}, \quad (3.1)$$

where  $p$  is the momentum of the charged particle measured in the MDC with corresponding path length  $L$ ,  $t$  is the measured time-of-flight and  $c$  the speed of light in vacuum. The start time is determined from reconstructed tracks of charged particles in the MDC [82]. A typical mass square distribution for different particle species and the  $\pi/K$  separation

efficiency is shown in Figure 3.4. The TOF provides clear separation capabilities of pions and kaons for particle momenta of up to 1 GeV/c, depending on the polar angle.

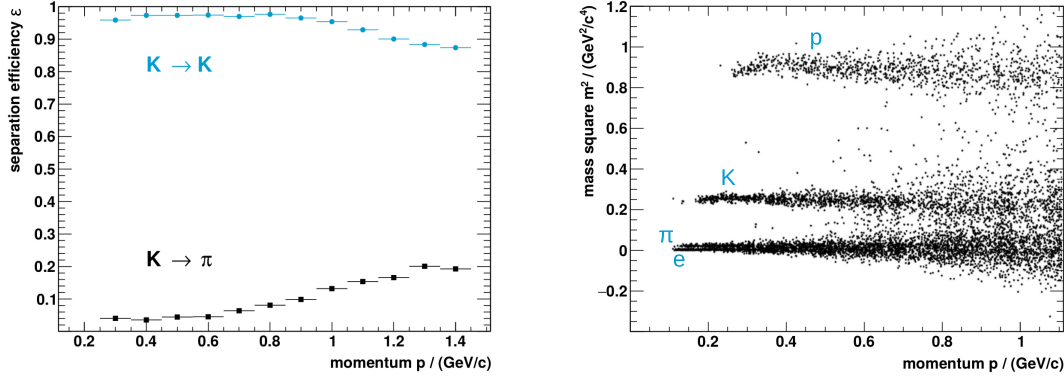


**Figure 3.4.:** Expected  $\pi/K$  misidentification rate (left) and mass square distribution (right) of the time-of-flight system for a simulation of different charge particle momenta  $p$ . Images edited from their original versions [78, 81].

#### 3.2.3. Electromagnetic Calorimeter (EMC)

The third and final detection system inside the coil of the superconducting solenoid magnet is an electromagnetic calorimeter, which is also the only detection system sensitive to photons. Photons play an important role not only in the present analysis, but for hadronic physics experiments in general. A requirement on the detection threshold is given by the energy range of the photons. While photons from decays of short-lived particles such as  $\pi^0$  and  $\eta$  typically have only a small amount of energy, the maximum energy that has to be measured is essentially given by the beam energy to measure processes like  $e^+e^- \rightarrow \gamma\gamma$ . To cover the energy range from  $\sim 20$  MeV up to 2.3 GeV the EMC is equipped with 6240 thallium doped caesium iodide CsI(Tl) crystals. Each crystal has a length of 28 cm, which corresponds to 15.1 radiation lengths  $X_0$  of CsI. Front and rear faces have a typical size of  $5.2 \text{ cm} \times 5.2 \text{ cm}$  to  $6.4 \text{ cm} \times 6.4 \text{ cm}$ , respectively. Similar to the TOF, the EMC is divided into a cylindrical barrel part and two endcaps. A total of 5280 crystals arranged in 44 layers make up the barrel part and each endcap is composed of 480 crystals arranged in 6 layers. All crystals are slightly tilted by  $\sim 1.5^\circ$ , pointing to a region  $\pm 10 \text{ cm}$  off the interaction point to avoid missing photons that could pass exactly between two crystals. The EMC polar angle coverage of the barrel and endcaps is  $|\cos \vartheta| < 0.82$  and  $0.83 < |\cos \vartheta| < 0.93$ , respectively. Energy deposition is also a valuable information for particle identification. For example, while muons and pions lose almost no energy passing through the EMC, electrons and positrons are stopped completely and deposit all their energy, as shown in Figure 3.5. The EMC provides an energy resolution of  $\sigma_E/E \leq 2.5\%$ .

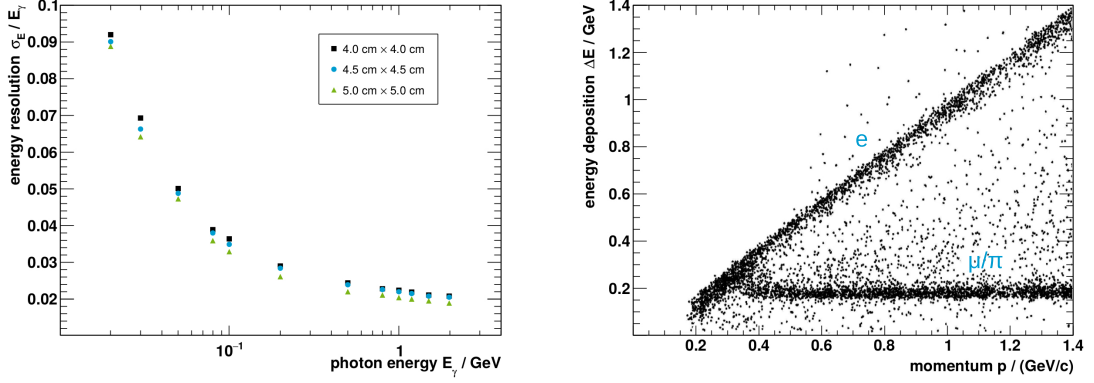


**Figure 3.5.:** Energy resolution for different lateral crystal dimensions depending on the incident photon energy (**left**) and particle identification capabilities by measuring the energy deposition in the EMC (**right**). Images edited from their original versions [78, 81].

### 3.2.4. Muon Identifier (MUC)

Although the three detection systems described above all have excellent resolution and particle identification capabilities, they cannot distinguish between pions and muons. Both particles share very similar properties, such as mass and electric charge. Hence, they produce almost the same specific energy loss and time-of-flight signals. However, most pions are stopped either in the electromagnetic calorimeter or in the coil of the superconducting solenoid. Muons, on the other hand, can penetrate large amounts of heavy material and most of them even escape the whole detector. Therefore, the muon identifier consists of resistive plate counters (RPC), embedded in the steel plates of the magnetic flux return yoke. The steel barrel is divided into nine layers and both endcaps include eight layers of RPC modules, covering  $\sim 89\%$  of the full solid angle. The active detector volume is filled with a gas mixture of Argon Ar, Tetrafluoroethane  $C_2F_4H_2$  and n-Butan  $C_4H_{10}$  (50%/42%/8%), providing an average single gap RPC efficiency of 96% at a working voltage of 8 kV and a dark current of less than  $1 \mu A/m^2$ . The muon identifier effectively distinguishes muons from pions and other hadrons above a cutoff momentum of 0.4 GeV/c.

### 3.2.5. Trigger System

The BESIII trigger system is a two-stage system consisting of a hardware trigger (L1) and a software event filter (L3). The L1 trigger is designed to select interesting physics events and to reduce cosmic ray and beam related backgrounds. Signals from the MDC, TOF and EMC are continuously buffered to the L1 field-programmable gate array (FPGA) driven front-end boards for at least 6.4  $\mu s$ . This L1 decision latency is mainly caused by the EMC signal shaping. The event time of charged tracks is determined by the TOF to

a precision of  $\sim 30$  ns. Once a signal is accepted by the L1 trigger logic, the complete readout buffer is transmitted to an online event filter. The L3 trigger further reduces the background rate based on various event filters, such as MDC track finding and EMC cluster shaping algorithms. After an event is accepted, it is permanently stored to disk with approximately 42 Mb/s during normal operation, which corresponds to an event rate of about 3 kHz. Expected event rates and typical background sources are summarized in Table 3.2.

**Table 3.2.:** Expected event rate of the BESIII trigger system at a center-of-mass energy corresponding to the  $J/\psi$  mass. Values are taken from [78].

Processes	Event rate (kHz)	After L1 (kHz)	After L3 (kHz)
Physics	2	2	2
Bhabha	0.8	Pre-scaled	Pre-scaled
Cosmic ray	$< 2$	$\sim 0.2$	$\sim 0.1$
Beam background	$> 10^4$	$< 2$	$< 1$
Total	$> 10^4$	4	3

## 4. Event Selection

The analysis presented in this work focuses mainly on the exclusive reconstruction of light hadron final states with topology  $p\bar{p}m$ , where  $m$  is a light meson, such as  $\eta$  or  $\omega$ . Light mesons are reconstructed via hadronic or electromagnetic decays into pions and photons, which can be measured by the BESIII detection system. The enormous amount of events that is produced and recorded in high-energy physics experiments like BESIII renders it necessary to pre-sort the data. An overview of the data sets that are analyzed within the scope of this thesis and applied pre-selection criteria is given in the following.

### 4.1. Data Samples and Monte Carlo Simulations

The BESIII experiment recorded its first hadronic event in July 2008 [78] and has continuously increased its available database of physics events ever since. Besides the world's largest  $J/\psi$  and  $\psi'$  resonance data sets, the BESIII collaboration has invested great effort to collect data at various center-of-mass energies between 2 GeV and 4.6 GeV in order to cover its broad physics program [76, 83]. The analysis in this work is based on data sets above 3.7 GeV, as shown in Figure 4.1, that are mainly used in searches for exotic states and D meson physics. A previous investigation of  $e^+e^- \rightarrow p\bar{p}\pi^0$  [87] has shown that the cross section for light hadron final states in this energy regime is expected to be rather small. Hence, this analysis could potentially be limited by the low statistics remaining after applying all selection criteria. In 2017, the BESIII collaboration initiated a systematic scan to precisely study the line shape of exotic candidates such as the  $\psi(4260)$  [20] by accumulating high luminosity ( $\sim 0.5 \text{ fb}^{-1}$ ) data sets at 10 MeV intervals starting at about 4.190 GeV. In the last run period this scan continued and was extended by eight new data samples. It should be noted that a final calibration of this data is still in progress, so it should not yet be used in any physics analysis. Therefore, only the high luminosity data samples at 17 center-of-mass energies  $\sqrt{s}$  between 3.7 GeV and 4.6 GeV with a total integrated luminosity  $L$  of  $14.7 \text{ fb}^{-1}$  are studied, as listed in Table 4.1. Integrated luminosities were measured based on the Bhabha scattering process  $e^+e^- \rightarrow (\gamma)e^+e^-$  [88]. The data is reconstructed and analyzed in the object-oriented software framework BOSS (BESIII Offline Software System) [89], which is based on the GAUDI framework [90], providing tools for event and detector simulation, data processing as well as physics analysis. The GEANT4-based [91] simulation software BOOST (BESIII object-oriented

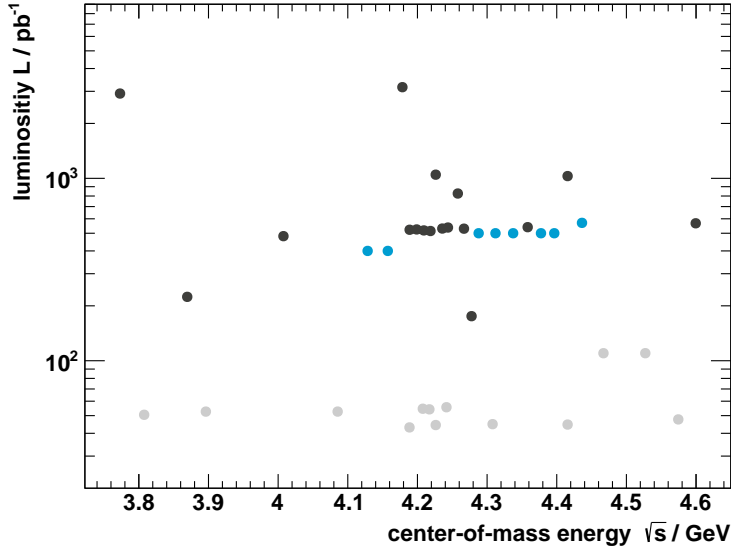


**Figure 4.1.:** Luminosities of various BESIII data sets at center-of-mass energies above 3.7 GeV. The 17 data samples that are used in this work (**black**), recently added high luminosity data sets (**blue**) and scan data (**gray**). Values are taken from [84–86].

simulation tool) [92] includes a geometric description of the BESIII detector, its response as well as performance and running conditions. For each energy point and for each analyzed final state, an additional one million signal events are simulated with the Monte Carlo (MC) generator software package ConExc [93]. The generator is constructed in the framework of BesEvtGen [94], an adaptation of the EvtGen [95] package, incorporating initial-state radiation (ISR) and vacuum polarization (VP) effects up to second order accuracy. Although BesEvtGen offers a variety of models to simulate the decay of intermediate hadronic resonances with correct angular distributions, all signal MC events in this work are generated evenly distributed in phase space. This allows for a simple one-dimensional estimation of the reconstruction and selection efficiencies. An effective description of the data is achieved with a partial wave analysis (PWA), as discussed in Section 5.4. To investigate possible background processes, a generic MC sample is used. The sample is provided by the BESIII collaboration and was generated with ConExc and KKMC [96] at 4.1784 GeV. It corresponds to an equivalent integrated luminosity of about 40 times the data luminosity, including open charm processes, continuum production of hadrons as well as QED and initial-state radiation processes. Known decay modes are generated with BesEvtGen with branching fractions set to world average values from the Particle Data Group (PDG) [36], while the remaining unmeasured decay modes are generated with the Lund Area Law Model [97, 98].

**Table 4.1.:** Center-of-mass energies  $\sqrt{s}$  [85, 86] and integrated luminosities  $L$  [84, 86] of the data samples studied in this analysis. The first uncertainty is statistical, the second is systematic. Uncertainties for the data set at 3.8695 GeV have not yet been published.

$\sqrt{s} / \text{GeV}$	$L / \text{pb}^{-1}$
3.7730	$2931.8 \pm 0.20 \pm 13.80$
3.8695	224.0
4.0076	$482.0 \pm 0.10 \pm 4.82$
4.1784	$3189.0 \pm 0.19 \pm 31.89$
4.1888	$524.6 \pm 0.10 \pm 5.25$
4.1989	$526.0 \pm 0.10 \pm 5.26$
4.2092	$518.0 \pm 0.10 \pm 5.18$
4.2187	$514.6 \pm 0.10 \pm 5.15$
4.2263	$1056.4 \pm 0.14 \pm 10.56$
4.2357	$530.3 \pm 0.10 \pm 5.30$
4.2438	$538.1 \pm 0.10 \pm 5.38$
4.2580	$828.4 \pm 0.13 \pm 8.28$
4.2668	$531.1 \pm 0.10 \pm 5.31$
4.2777	$175.7 \pm 0.10 \pm 1.76$
4.3583	$543.9 \pm 0.10 \pm 5.44$
4.4156	$1043.9 \pm 0.13 \pm 10.43$
4.5995	$586.9 \pm 0.11 \pm 5.87$

## 4.2. Initial Track Selection

As already mentioned, it is necessary to pre-sort the available data and reduce the number of events to a size that is appropriate for further offline analysis. Charged tracks and neutral showers in each event are reconstructed with a track fitting algorithm [99] based on the Kalman filter method [100] and must satisfy certain criteria before being combined to one of the analyzed final states.

### 4.2.1. Charged Track Selection and Particle Identification

Hadronic resonances involved in any of the final states analyzed in this work decay via the strong interaction and have only a very short lifetime. Thus, all charged particles detected in the MDC are expected to have a common point of origin. Therefore, a vertex fit is performed, varying the reconstructed track parameters  $(d_\rho, \phi_0, \kappa, d_z, \lambda)$  within their measured uncertainties. This helix parameterization contains the distance  $d_\rho$  of the helix from the pivotal point in  $xy$  plane, the azimuthal angle  $\phi_0$  to specify the pivotal point with respect to the helix center, the signed reciprocal transverse momentum  $\kappa$  so that

$\kappa = Q/p_t$  and  $\rho = \alpha/\kappa$ , with  $Q$  being the charge,  $\rho$  the signed radius of the helix and  $\alpha = 1/cB$  the magnetic field dependent constant,  $d_z$  is the distance of the helix from the pivotal point in  $z$  direction and  $\lambda$  is the dip angle [101]. The fit minimizes the distance  $d$  between the common vertex, i.e., the point with the smallest distance to all charged particle trajectories, and the run dependent interaction point, as illustrated in Figure 4.2. It is convenient to define a reference frame with the interaction point as its origin and the  $z$  axis in the direction of the homogeneous magnetic field. In this system, reasonable constraints on the point of closest approach  $\mathbf{v} = (v_x, v_y, v_z)$  of each track to the interaction point are given by

$$v_r = \sqrt{v_x^2 + v_y^2} < 1 \text{ cm} ,$$

$$|v_z| < 10 \text{ cm} .$$

Due to the geometry of the MDC, the polar angle of each track has to fulfill  $|\cos \vartheta| < 0.93$ .

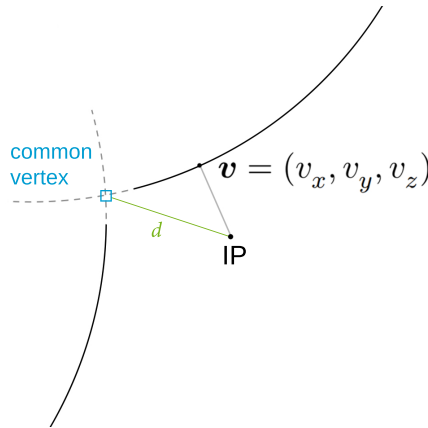


**Figure 4.2.:** Illustration of the trajectories of two charged tracks. The distance  $d$  between their common vertex and the run dependent interaction point (IP) is minimized by a vertex fit. The point of closest approach  $\mathbf{v}$  is used to define constraints on the charged tracks of the ejectiles of short-lived resonances.

Particles are identified utilizing the Particle Identification system (PID) of BESIII [76]. The response of a detector element to each particle is given by a probability density function (PDF), which, written as  $\mathcal{P}(x; \mathcal{H})$ , describes the probability that a charged particle of species  $\mathcal{H} \in \{e^\pm, \mu^\pm, \pi^\pm, K^\pm, p, \bar{p}\}$  leaves a signature  $x$  described by a vector of measurements  $(dE/dx, t, m^2, \Delta E/p, \dots)$ . This vector can describe a single measurement in one detector element or several measurements of the detection system. The measurements may be correlated for a single particle hypothesis. At BESIII, the time-of-flight  $t$  and the specific ionization deposit  $dE/dx$  of a charged particle traversing the MDC are most essential for hadron separation. Since these variables have almost no influence on each other, relative likelihoods provide the most powerful discrimination



between particle hypotheses  $\mathcal{H}$ . In the present analysis, protons and pions are identified by comparing the corresponding probabilities

$$\begin{aligned} \mathcal{P}(p) &> \mathcal{P}(\pi) , & \mathcal{P}(p) &> \mathcal{P}(K) , & \mathcal{P}(p) &> 10^{-5} , \\ \mathcal{P}(\pi) &> \mathcal{P}(p) , & \mathcal{P}(\pi) &> \mathcal{P}(K) , & \mathcal{P}(\pi) &> 10^{-5} . \end{aligned}$$

A minimal probability is required to reduce the background with tracks, where the PID system is unable to determine a clear candidate.

If variables are highly correlated, such as  $\Delta E/p$  and the shower shape of electrons in the EMC, near-optimal discrimination variables may be constructed using neural networks. An artificial neural network [102] is a computing system inspired by biological neural processing. It can be applied to the BESIII PID algorithm and is implemented in ROOT [103, 104] as a multilayer perceptron (MLP) neural network.

#### 4.2.2. Photon Candidate Selection

A photon produces an electromagnetic shower in one or more crystals of the EMC. Geometrically adjacent hits are combined by a cluster finding algorithm [99]. The position of the primary hit is calculated as the weighted average of the energy deposits. To suppress background photons in the EMC, a minimal energy deposit  $\Delta E$  is required

$$\begin{aligned} \Delta E &> 25 \text{ MeV in the barrel region } |\cos \vartheta| < 0.8 , \\ \Delta E &> 50 \text{ MeV in end-cap regions } 0.86 < |\cos \vartheta| < 0.92 . \end{aligned}$$

The higher threshold for photon detection in the endcaps is set to reduce low-energetic photons from beam backgrounds. A cut on the timing information  $T$  from the EMC with respect to the event start time further suppresses electronic noise and energy deposits unrelated to the event

$$0 \text{ ns} \leq T \leq 700 \text{ ns} .$$

Additionally, a cut is applied on the angle between straight lines from the vertex to the position of the shower and the extrapolated position of the closest charged track  $t$  in the EMC, with a more stringent cut for antiprotons due to the larger shower size in antiproton annihilation with the detector material

$$\angle(t, \gamma) > 10^\circ , \quad \angle(\bar{p}, \gamma) > 30^\circ .$$

### 4.3. Kinematic Fit

After the initial track selection, particles are combined to different final states, as listed in Table 4.2. Subsequent  $\pi^0$  and  $\eta$  decays are reconstructed via their electromagnetic decays into two photons. Due to noise in the EMC, the number of photons is only restricted to being greater than or equal to the number of photons in the final state. For each combination a kinematic fit is performed, a method similar to the vertex fit. While a vertex fit varies the helix parameters, a kinematic fit varies the components of the reconstructed four-vectors of all particles. Fits are performed within the BOSS software framework and are based on the Lagrange multiplier method [105]. A common set of kinematic constraints is given by energy and momentum conservation. In an exclusive reconstruction of a final state, the sum of four-vectors of all final-state particles must be equal to the four-vector of the initial state. In the following, a fit that only uses these constraints is called a four-constraint (4C) fit. Additional constraints  $m$  may be specified, e.g., on the invariant mass of two photon candidates, which can be required to correspond to the mass of the  $\pi^0$  or  $\eta$  meson. If there is more than one combination in an event, the one yielding the smallest  $\chi^2$  value is kept for further analysis.

**Table 4.2.:** Branching fractions  $\mathcal{Br}$  [36] and reconstruction patterns of the analyzed final states as well as the number of additional mass constraints  $m$  used in the kinematic fit.

mode $i$	$\mathcal{Br} (\Gamma_i/\Gamma)$	$N_{\mathbf{p}}$	$N_{\bar{\mathbf{p}}}$	$N_{\pi^+}$	$N_{\pi^-}$	$N_{\gamma}$	$m$
$\eta \rightarrow \gamma\gamma$	$(39.41 \pm 0.20) \%$	1	1	0	0	$\geq 2$	0
$\rightarrow \pi^0\pi^0\pi^0$	$(32.68 \pm 0.23) \%$	1	1	0	0	$\geq 6$	3
$\rightarrow \pi^+\pi^-\pi^0$	$(22.92 \pm 0.28) \%$	1	1	1	1	$\geq 2$	1
$\omega \rightarrow \pi^+\pi^-\pi^0$	$(89.2 \pm 0.7) \%$	1	1	1	1	$\geq 2$	1
$\eta' \rightarrow \eta\pi^+\pi^-$	$(42.6 \pm 0.7) \%$	1	1	1	1	$\geq 2$	1
$f_1 \rightarrow \eta\pi^+\pi^-$	$(35 \pm 15) \%$	1	1	1	1	$\geq 2$	1

## 5. Analysis of $e^+e^- \rightarrow p\bar{p}\eta$ and $e^+e^- \rightarrow p\bar{p}\omega$

In the following, a full analysis of the data is presented regarding the cross section of the  $p\bar{p}\eta$  and  $p\bar{p}\omega$  final states in  $e^+e^-$  annihilations at BESIII and the search for exotic resonances. This includes the determination of various observables required to calculate the total cross section as well as investigating the respective statistical and systematic uncertainties. In general, the Born cross section, which is described in more detail in Section 5.5, can be calculated by

$$\sigma^B(e^+e^- \rightarrow p\bar{p}m) = \frac{N_{\text{obs}}}{L \cdot (1 + \delta_r) \cdot (1 + \delta_v) \cdot \varepsilon \cdot \mathcal{B}r} , \quad (5.1)$$

where  $N_{\text{obs}}$  is the number of observed events,  $L$  the integrated luminosity,  $(1 + \delta_r)$  and  $(1 + \delta_v)$  are correction factors for initial-state radiation and vacuum polarization,  $\varepsilon$  the detection efficiency and  $\mathcal{B}r$  is the product branching ratio of the full decay chain. The first step is to correctly identify all final-state particles. Protons  $p$  and antiprotons  $\bar{p}$  are measured with the BESIII detection system and leave a rather clear signature, as described in Chapter 3. Light, short-lived mesons  $m$ , on the other hand, cannot be detected directly, but have to be reconstructed via hadronic or electromagnetic decays into charged pions and photons. The  $\eta$  meson is reconstructed in three decay modes, namely  $\eta \rightarrow \gamma\gamma$ ,  $\eta \rightarrow \pi^0\pi^0\pi^0$  and  $\eta \rightarrow \pi^+\pi^-\pi^0$ , covering 95 % of the total branching fraction. The  $\omega$  meson has a very dominant decay mode into three pions ( $\pi^+\pi^-\pi^0$ ) with a branching fraction of 89.2(7) % [36]. After a kinematic fit is applied, as described in Section 4.3, the  $\eta$  and  $\omega$  mesons are identified by the invariant mass of their decay products. In order to greatly reduce background that is not related to an  $\eta$  or  $\omega$  event, wide mass windows are applied given by

$$0.4 \text{ GeV}/c^2 \leq m(\eta) \leq 0.7 \text{ GeV}/c^2 , \quad (5.2)$$

$$0.6 \text{ GeV}/c^2 \leq m(\omega) \leq 1.1 \text{ GeV}/c^2 , \quad (5.3)$$

where  $m(\eta)$  and  $m(\omega)$  represent the invariant mass of their respective decay particles. The resulting invariant mass distributions are shown in Figure 5.1. Clear peaks are observed at the nominal positions of the  $\eta$  mass ( $m_\eta = 547.862(17) \text{ MeV}/c^2$ ) [36] and the  $\omega$  mass ( $m_\omega = 782.65(12) \text{ MeV}/c^2$ ) [36] on top of a small background. Further analysis steps rely heavily on the understanding of the background contributions.

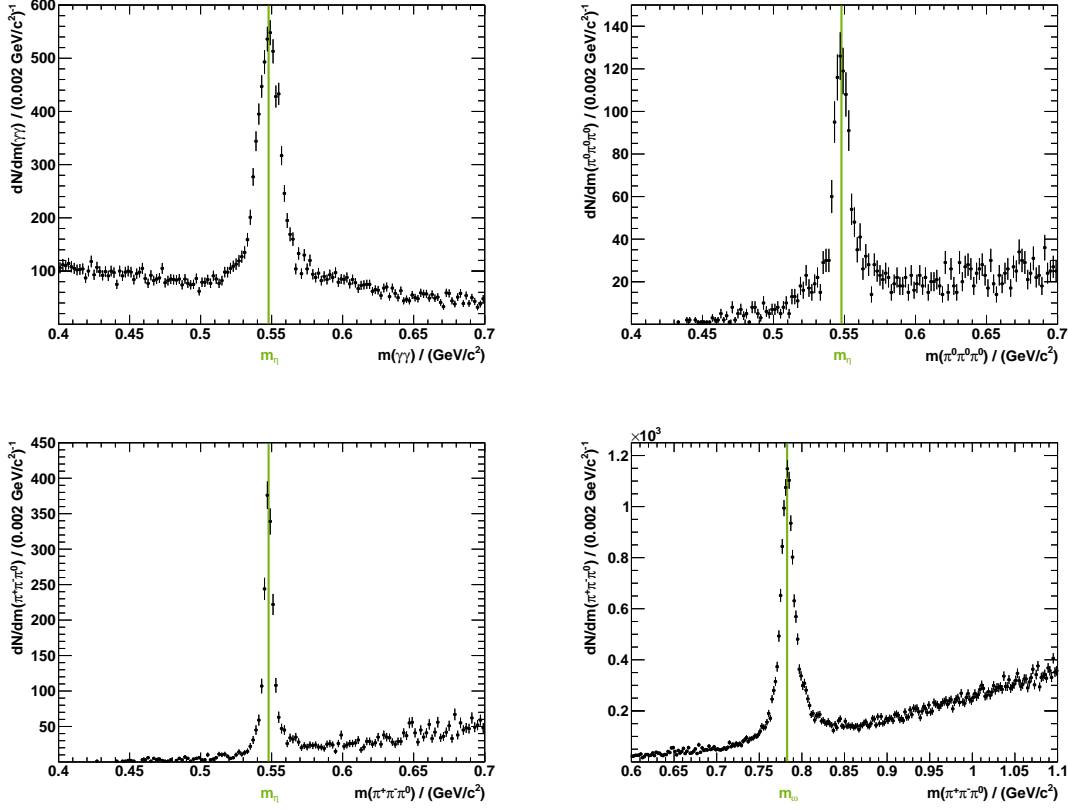


**Figure 5.1.:** Invariant mass distributions of the  $\eta$  and  $\omega$  systems for various decay modes:  $\eta \rightarrow \gamma\gamma$  (top left),  $\eta \rightarrow \pi^0\pi^0\pi^0$  (top right),  $\eta \rightarrow \pi^+\pi^-\pi^0$  (bottom left) and  $\omega \rightarrow \pi^+\pi^-\pi^0$  (bottom right). Black dots represent the data summed up over all 17 data sets, and green lines indicate the nominal positions of the  $\eta$  and  $\omega$  mass.

## 5.1. Background Studies

Possible background contributions are studied in more detail using the generic MC sample provided by BESIII. To minimize statistical uncertainties, this sample was generated with a size corresponding to 40 times the data luminosity and has to be scaled down to fit the data. One should note however, that the cross sections of most of the processes which are included in this data sample are still very poorly measured, if at all, and are therefore affected by large uncertainties. Due to this, the relative number of events from different reactions within the generic MC sample does not necessarily have to match the data. In addition, there are many reactions that have not yet been measured and their influence is estimated with the Lund model. The generic MC sample is therefore scaled using two separate scale parameters, one each for signal and background, which are determined by a fit to the data. The invariant masses of the  $\eta$  and  $\omega$  systems at a center-of-mass energy of  $4.1784 \text{ GeV}$  are presented in Figures 5.2 and 5.3, showing a good agreement between data and MC. For example, the invariant mass of the three pions  $m(\pi^+\pi^-\pi^0)$

is described almost perfectly regarding the signal as well as the integrated background distribution. In both cases, i.e., the  $\eta$  and the  $\omega$  decay, the background consists mostly of mixtures of  $\Delta$  baryons, nucleons,  $\rho$  mesons and pions as listed in Tables 5.1 and 5.2. The peaking structure in the invariant mass distribution of the two photons is nicely reproduced by the  $p\bar{p}\eta$  signal part. However, according to the MC sample, the background comes almost exclusively from  $p\bar{p}$  production. This is very surprising, since the cross section  $\sigma(e^+e^- \rightarrow p\bar{p})$  at such high center-of-mass energies is  $0.7(7)$  pb [106, 107] and the detection efficiency is in the order of 1 % due to the two missing photons in the final state. With a luminosity of  $3189.0 \text{ pb}^{-1}$  at 4.1784 GeV the number of expected  $p\bar{p}$  events is only about 22 compared to the 1432 events seen in the generic MC sample. These numbers are obviously not compatible with each other and one needs to be careful when interpreting the relative background composition. Investigations of the invariant mass of systems other than the light meson decay system reveal additional discrepancies between data and MC. The  $p\eta$  invariant mass distributions show a significant underestimation of the data at low invariant masses, which is particularly visible in the  $\eta \rightarrow \gamma\gamma$  decay mode thanks to the large statistics. Such an enhancement in data could be explained by additional nucleon resonances  $N^*$  with substantial branching fractions to  $N\eta$  final states, as the  $N(1535)$  [36].

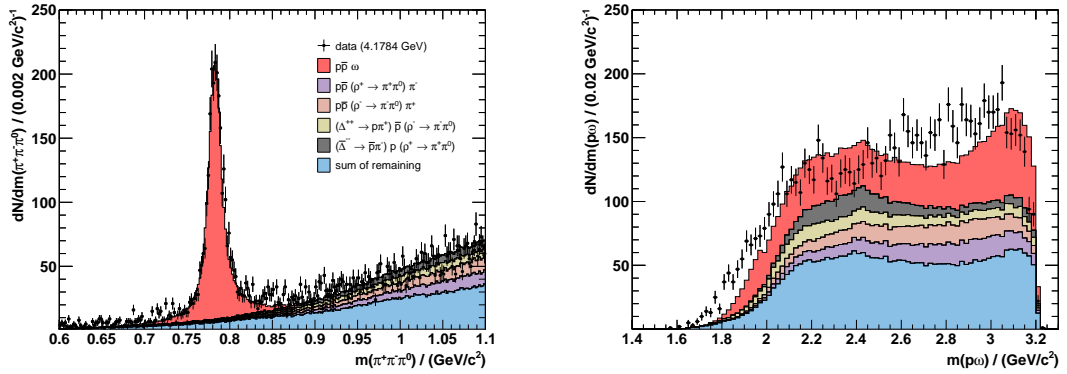


**Figure 5.2.:** Invariant mass distributions of the  $\pi^+\pi^-\pi^0$  (left) and  $p\omega$  (right) systems for the reconstructed decay  $\omega \rightarrow \pi^+\pi^-\pi^0$ , showing data at 4.1784 GeV (black dots) in comparison to differently colored, stacked contributions from the generic MC sample: The  $p\bar{p}\omega$  signal (red), the four most dominant background contributions, as well as the sum of all remaining background processes (blue). An overall scaling factor as well as the signal to background ratio have been determined using a fit.

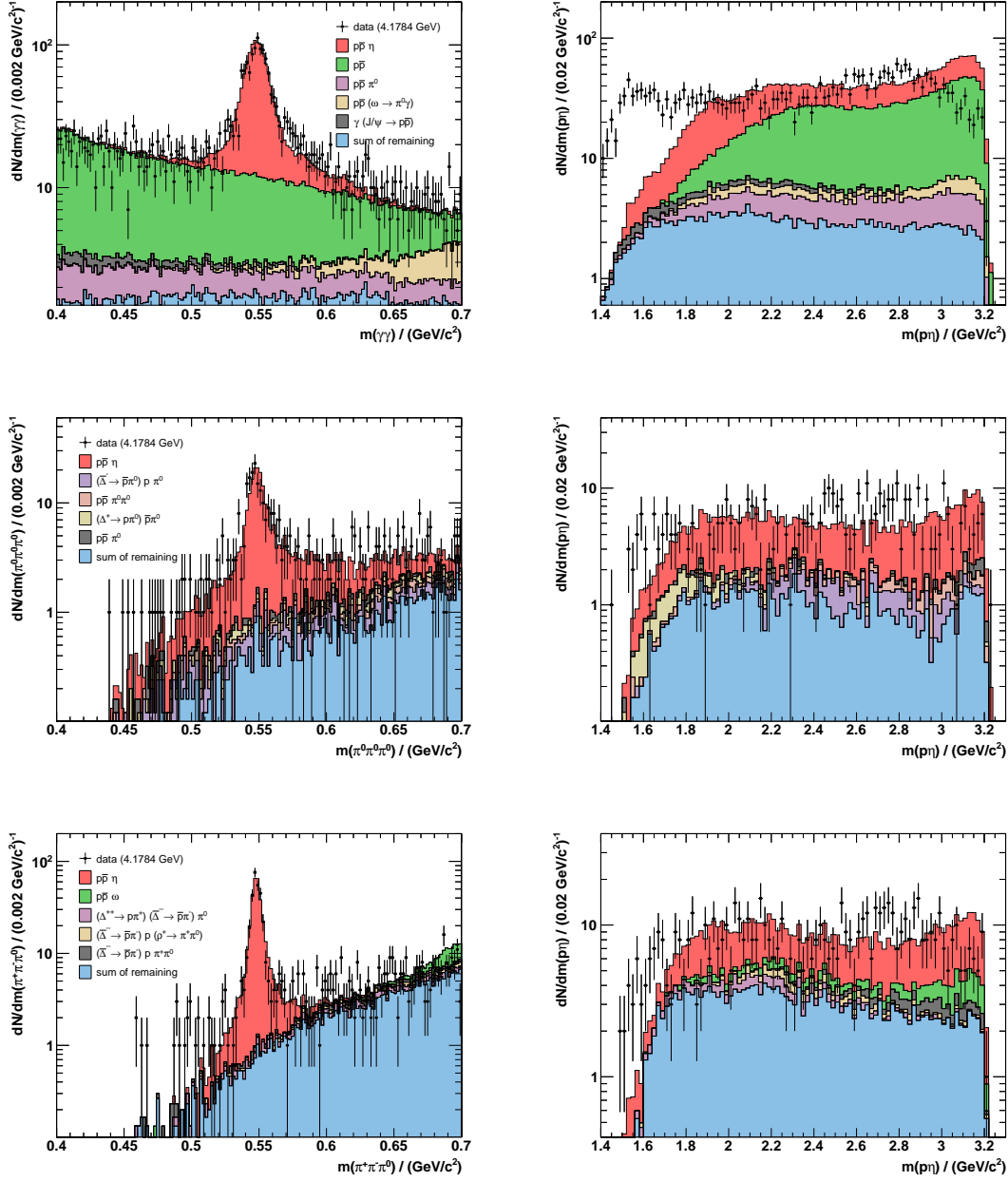


**Figure 5.3.:** Invariant mass distributions of the  $\eta$  (left) and  $p\eta$  (right) systems for three reconstructed  $\eta$  decay modes:  $\eta \rightarrow \gamma\gamma$  (top),  $\eta \rightarrow \pi^0\pi^0\pi^0$  (middle) and  $\eta \rightarrow \pi^+\pi^-\pi^0$  (bottom). Black dots represent the data at 4.1784 GeV compared to differently colored, stacked contributions from the generic MC sample: The  $p\bar{p}\eta$  signal (red), the four most dominant background contributions, as well as the sum of all remaining background processes (blue). An overall scaling factor as well as the signal to background ratio have been determined using a fit.

**Table 5.1.:** Topology of events from the generic MC sample at 4.1784 GeV, which survived all selection criteria in the reconstruction of the  $p\bar{p}\eta$  final state. The list is subdivided by the three decay modes of the  $\eta$  meson:  $\eta \rightarrow \gamma\gamma$  (**top**),  $\eta \rightarrow \pi^0\pi^0\pi^0$  (**middle**) and  $\eta \rightarrow \pi^+\pi^-\pi^0$  (**bottom**). The signal processes are highlighted in green above the most dominant background channels that are ordered by occurrence, where  $N$  is the scaled number of events.

Process	Final state	$N$
$p\bar{p}(\eta \rightarrow \gamma\gamma)$	$p\bar{p}\gamma\gamma$	1112
$(\eta \rightarrow \gamma\gamma)(J/\psi \rightarrow p\bar{p})$	$p\bar{p}\gamma\gamma$	95
$p\bar{p}$	$p\bar{p}$	1432
$p\bar{p}\pi^0$	$p\bar{p}\gamma\gamma$	133
$p\bar{p}(\omega \rightarrow \pi^0\gamma)$	$p\bar{p}\gamma\gamma\gamma$	64
$\gamma(J/\psi \rightarrow p\bar{p})$	$p\bar{p}\gamma$	33
sum of remaining		257
$p\bar{p}(\eta \rightarrow \pi^0\pi^0\pi^0)$	$p\bar{p}\pi^0\pi^0\pi^0$	249
$(\eta \rightarrow \pi^0\pi^0\pi^0)(J/\psi \rightarrow p\bar{p})$	$p\bar{p}\pi^0\pi^0\pi^0$	22
$(\bar{\Delta}^- \rightarrow \bar{p}\pi^0)p\pi^0$	$p\bar{p}\pi^0\pi^0$	27
$p\bar{p}\pi^0\pi^0$	$p\bar{p}\pi^0\pi^0$	16
$(\Delta^+ \rightarrow p\pi^0)\bar{p}\pi^0$	$p\bar{p}\pi^0\pi^0$	15
$p\bar{p}\pi^0$	$p\bar{p}\pi^0$	11
sum of remaining		81
$p\bar{p}(\eta \rightarrow \pi^+\pi^-\pi^0)$	$p\bar{p}\pi^+\pi^-\pi^0$	300
$(\eta \rightarrow \pi^+\pi^-\pi^0)(J/\psi \rightarrow p\bar{p})$	$p\bar{p}\pi^+\pi^-\pi^0$	30
$p\bar{p}(\omega \rightarrow \pi^+\pi^-\pi^0)$	$p\bar{p}\pi^+\pi^-\pi^0$	48
$(\Delta^{++} \rightarrow p\pi^+)(\Delta^{--} \rightarrow \bar{p}\pi^-)\pi^0$	$p\bar{p}\pi^+\pi^-\pi^0$	28
$(\bar{\Delta}^{--} \rightarrow \bar{p}\pi^-)p(\rho^+ \rightarrow \pi^+\pi^0)$	$p\bar{p}\pi^+\pi^-\pi^0$	19
$(\bar{\Delta}^{--} \rightarrow \bar{p}\pi^-)p\pi^+\pi^0$	$p\bar{p}\pi^+\pi^-\pi^0$	19
sum of remaining		245

Despite these discrepancies, there is a lot of useful information to be gained from the generic MC sample. None of the background contributions shows a peaking behavior that could occur due to a misidentification of protons or processes with additional particles, such as  $\gamma p\bar{p}\eta$ . In fact, in the case of the decay of  $\eta$  into two photons, only 11 events are found out of 3126 total events where the proton or antiproton was falsely identified, so that this background is negligible.

The signal of the  $\eta$  decaying into three neutral pions has a very broad distribution, due to the reconstruction via six photons. This makes it difficult to apply some of the analysis techniques used when evaluating observables, such as number of observed events  $N_{\text{obs}}$  or detection efficiencies  $\varepsilon$ , as described in the upcoming sections. Since the statistics for the  $\eta \rightarrow \pi^0\pi^0\pi^0$  decay mode is also very small, it is excluded from the rest of the analysis.

**Table 5.2.:** Topology of events from the generic MC sample at 4.1784 GeV, which survived all selection criteria in the reconstruction of the  $\rho\bar{\rho}\omega$  final state. Background channels are ordered by their occurrence, where  $N$  is the scaled number of events, and the signal is highlighted in green.

Process	Final state	$N$
$\rho\bar{\rho}(\omega \rightarrow \pi^+\pi^-\pi^0)$	$\rho\bar{\rho}\pi^+\pi^-\pi^0$	2604
$\rho\bar{\rho}(\rho^+ \rightarrow \pi^+\pi^0)\pi^-$	$\rho\bar{\rho}\pi^+\pi^-\pi^0$	727
$\rho\bar{\rho}(\rho^- \rightarrow \pi^-\pi^0)\pi^+$	$\rho\bar{\rho}\pi^+\pi^-\pi^0$	725
$(\Delta^{++} \rightarrow \rho\pi^+)\bar{\rho}(\rho^- \rightarrow \pi^-\pi^0)$	$\rho\bar{\rho}\pi^+\pi^-\pi^0$	578
$(\bar{\Delta}^{--} \rightarrow \bar{\rho}\pi^-)\rho(\rho^+ \rightarrow \pi^+\pi^0)$	$\rho\bar{\rho}\pi^+\pi^-\pi^0$	575
$\rho\bar{\rho}(\rho^0 \rightarrow \pi^+\pi^-)\pi^0$	$\rho\bar{\rho}\pi^+\pi^-\pi^0$	470
sum of remaining		4993

Additionally, the generic MC sample can be used to optimize selection criteria to further reduce the background. A common variable to constrain is the  $\chi^2$  value of the kinematic fit. It determines the goodness of the fit, where small values are expected for signal and large values for background events. In particular, this variable is not affected by missing  $N^*$  resonances, since it is only sensitive to the final state and the correct composition of the intermediate states is irrelevant. A figure of merit (FOM) is defined as

$$f(\chi_{\text{cut}}^2) = \frac{S}{\sqrt{S+B}} \ , \quad (5.4)$$

where  $S$  and  $B$  are the scaled number of signal and background events left after applying a cut to the  $\chi^2$  value. The FOM is used to optimize the significance of the signal. Results are presented in Figure 5.4. For the  $\eta \rightarrow \gamma\gamma$  decay mode,  $f$  has a maximum at a  $\chi^2$  value of 30. In the other two cases, i.e.,  $\eta \rightarrow \pi^+\pi^-\pi^0$  and  $\omega \rightarrow \pi^+\pi^-\pi^0$ , the background consists mostly of processes forming the exact same final state as the signal itself. Hence, a 5C kinematic fit cannot distinguish between signal and background. An additional constraint on the mass of the meson could change this situation, but it would introduce a bias. Therefore, a cut is only applied for the electromagnetic decay mode of the  $\eta$  meson.

However, the discrepancies between data and MC make it necessary to crosscheck the results. Here a sideband approach is used. The background distributions can be described by a first or second order polynomial, depending on the channel the meson is reconstructed in. In particle physics one often has to deal with low statistics and must account for the Poisson nature of the data. In the present case, some of the invariant mass bins contain only a very small amount of events. Therefore binned maximum likelihood fits are performed to the invariant mass distributions of the meson candidates within



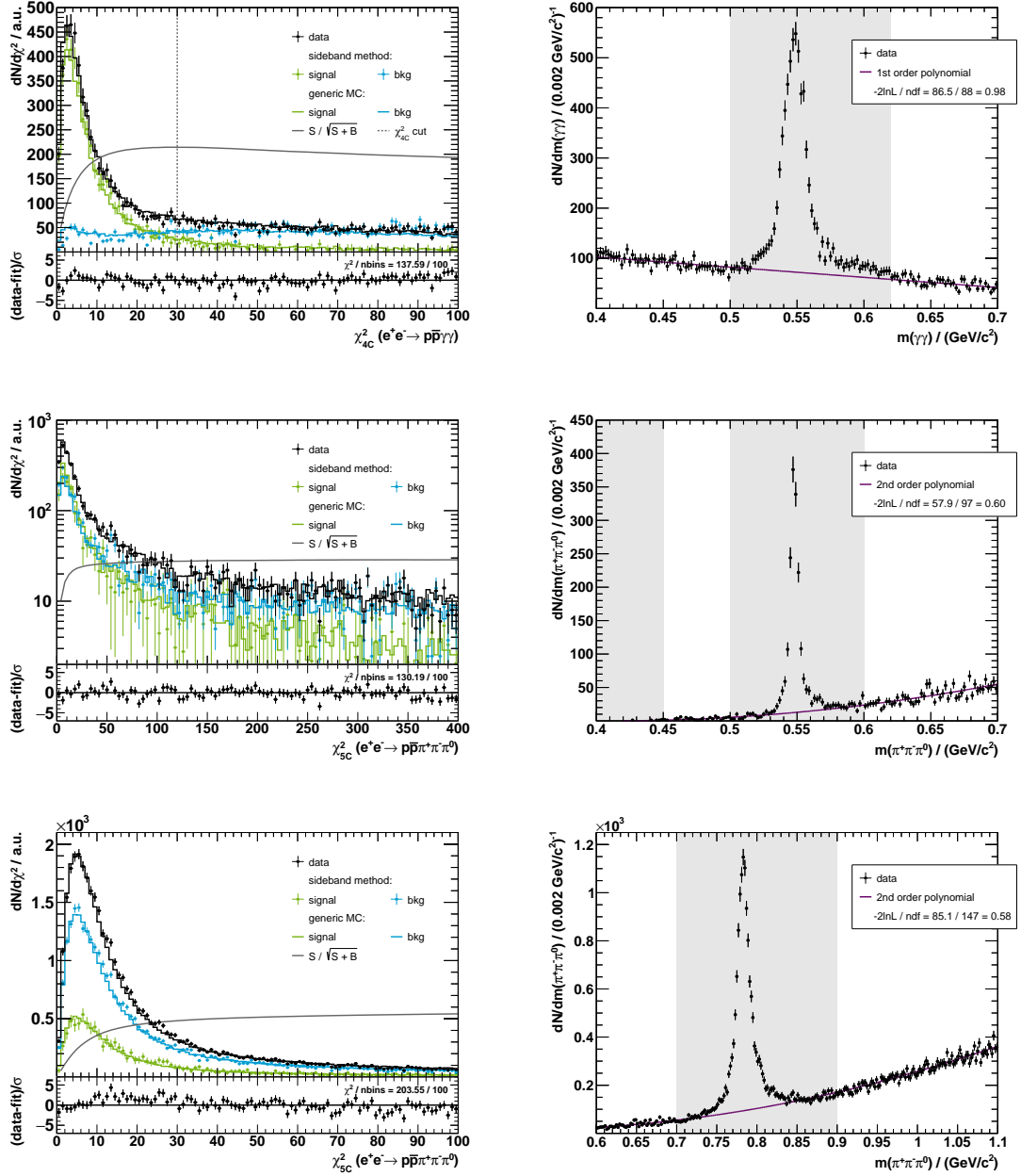


**Figure 5.4.: Left:**  $\chi^2$  distributions of the kinematic fits to the  $p\bar{p}m$  final states for three different meson decay modes:  $\eta \rightarrow \gamma\gamma$  (**top**),  $\eta \rightarrow \pi^+\pi^-\pi^0$  (**middle**) and  $\omega \rightarrow \pi^+\pi^-\pi^0$  (**bottom**). Black dots represent the data, summed up over all 17 high luminosity data sets. Signal (green) and background (blue) contributions are obtained from the generic MC sample (solid lines) or determined by a sideband approach (dots). The dashed lines indicate cuts on the  $\chi^2$  value and the figures of merit (gray solid lines) are arbitrarily scaled for better visibility. **Right:** Corresponding invariant mass distributions and the fits to the background distributions, as described in more detail in Section 5.1. Gray shaded areas are excluded from the fits.

two generously chosen sidebands excluding the peak region, as shown in Figure 5.4. A likelihood is defined based on Poisson statistics as

$$\mathcal{L} = \prod_i P_i = \prod_i \frac{\mu_i^{n_i} e^{-\mu_i}}{n_i!} , \quad (5.5)$$

where  $n_i$  is the number of events in the  $i$ -th invariant mass bin and  $\mu_i$  is the expected number of events in the same bin. The likelihood is maximized, or rather the negative log-likelihood is minimized with the MINUIT2 software package [108]. The  $\chi^2$  distribution of sideband events is scaled according to the fit to account for the background under the peak. Signal contributions are obtained by subtracting the scaled sidebands from the total  $\chi^2$  distributions as shown in Figure 5.4. Results of the sideband approach and from the generic MC sample agree with each other within their statistical uncertainties.

## 5.2. Number of Observed Events

The number of observed events  $N_{\text{obs}}$  for each final state can be determined by a fit to the invariant mass distributions. The signal is described using the signal Monte Carlo shape  $h(x)$  as input convolved with a Gaussian  $g(x)$  to account for a possible underestimation of the momentum resolution. The convolution is given by

$$f_{\text{sig}}(x) = \int h(x)g(x - \tau)d\tau , \quad (5.6)$$

where  $f_{\text{sig}}(x)$  is the signal part of the total fit function and  $x$  is the invariant mass of the meson system. It is calculated using a Fast Fourier Transform (FFT) algorithm built into the ROOT software package [103]. Background contributions of the  $\gamma\gamma$  and  $\pi^+\pi^-\pi^0$  decay modes are considered by a first and second order polynomial, respectively. A maximum likelihood fit is performed, first to the sum of all 17 data samples. Results are shown in Figure 5.5, that accurately describe the data in all three cases. In particular, the resolution of the peaks is correctly reproduced in each fit. Due to its unique properties, the  $\eta$  meson has a very small decay width of  $\Gamma_\eta = 1.31(5) \text{ keV}/c^2$  [36]. Hence, the width of the peak seen in data in the  $\eta \rightarrow \gamma\gamma$  reconstruction of about  $8.0(2) \text{ MeV}/c^2$  is determined solely by the detection resolution of the two photons in the EMC. The signal MC distribution has a width of  $7.50(1) \text{ MeV}/c^2$  and the difference between data and MC is accounted for in the fit by an additional Gaussian distribution with  $\sigma = 2.3(4) \text{ MeV}/c^2$ . In the reconstruction of  $\eta \rightarrow \pi^+\pi^-\pi^0$  the peaking structure has a width of  $3.4(1) \text{ MeV}/c^2$  due to the better momentum resolution of the MDC as well as the kinematic fit.

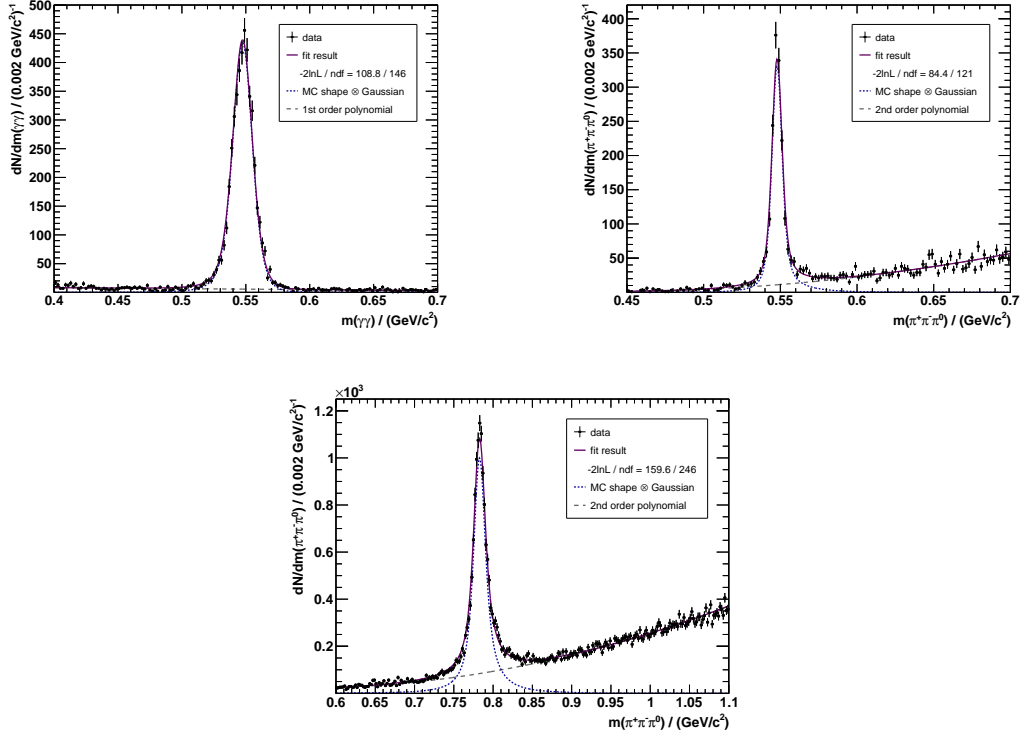


**Figure 5.5.:** Invariant mass distributions of the  $\eta$  and  $\omega$  meson decay systems for  $\eta \rightarrow \gamma\gamma$  (**top left**),  $\eta \rightarrow \pi^+\pi^-\pi^0$  (**top right**) and  $\omega \rightarrow \pi^+\pi^-\pi^0$  (**bottom**) after applying all selection criteria. Black dots represent data, summed up over all 17 data samples. The results of the fits, as described in the text, are shown by solid lines and the signal and background components are indicated by blue dotted and gray dashed lines, respectively.

The resolution of the two photons from the subsequent  $\pi^0$  decay is significantly improved by an additional mass constraint, as described in Section 4.3. The peak in the reconstruction of  $\omega \rightarrow \pi^+\pi^-\pi^0$  is slightly broader due to the decay width of the  $\omega$  meson ( $\Gamma_\eta = 8.49(8) \text{ MeV}/c^2$ ) [36].

In a second step, a maximum likelihood fit is performed for each data set individually, as shown exemplarily in Figure 5.6 for the high statistics data sample at 3.7730 GeV and the one with the smallest statistics at 4.2777 GeV. Figures of all other data sets can be found in Appendix A. Due to the low statistics in some data samples, the background shape is fixed to the result of the overall fit. The signal distribution can be obtained by subtracting the background portion of the fit from data. The uncertainty of the new bin-content is given by

$$\Delta n_{\text{sig}} = \sqrt{(\Delta n)^2 + (\Delta f_{\text{bkg}})^2}, \quad (5.7)$$

where  $\Delta n_{\text{sig}}$  is the uncertainty of the Poisson distributed remaining bin-content and  $\Delta f_{\text{bkg}}$  is the uncertainty of the background part of the fit given by

$$\Delta f_{\text{bkg}} = \sqrt{\sum_{i,j} \frac{\partial f}{\partial a_i} \cdot \frac{\partial f}{\partial a_j} \cdot \text{cov}_{ij}}, \quad (5.8)$$

where the double sum runs over all background fit parameters,  $\frac{\partial f}{\partial a_i}$  is the partial derivative of the fit function with respect to parameter  $a_i$  and  $\text{cov}_{ij}$  is an element of the covariance matrix given by  $\text{cov}_{ij} = \Delta a_i \cdot \Delta a_j \cdot \text{cor}_{ij}$ , with correlation matrix elements  $\text{cor}_{ij}$ . It should be noted that correlations between  $\Delta n$  and  $\Delta f_{\text{bkg}}$  are not taken into account. Therefore, the uncertainty  $\Delta n_{\text{sig}}$  will be slightly overestimated. The number of observed events  $N_{\text{obs}}$  is determined by integrating the background subtracted signal distributions within the so-called signal region, which contains 95 % of the signal events. Two additional sideband regions are defined that are used in the amplitude analysis for the efficiency determination described in the upcoming section.

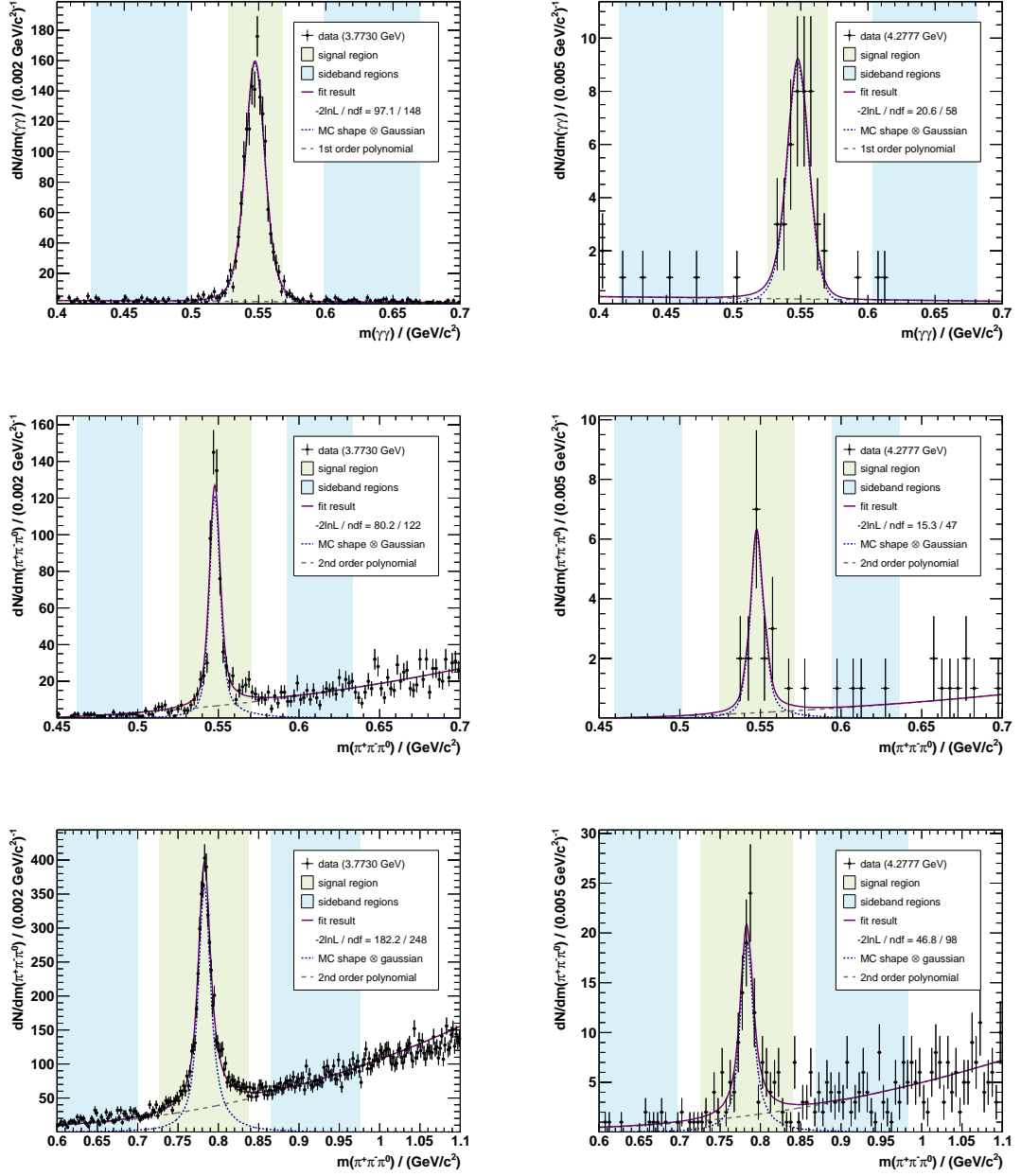


**Figure 5.6.:** Invariant mass of the meson system in the reconstruction of the  $\eta \rightarrow \gamma\gamma$  (**top**),  $\eta \rightarrow \pi^+\pi^-\pi^0$  (**middle**) and  $\omega \rightarrow \pi^+\pi^-\pi^0$  (**bottom**) decay modes for the high statistics data set at 3.7730 GeV (**left**) and the one with smallest statistics at 4.2777 GeV (**right**), fitted with the signal MC shape convolved with a Gaussian and a first or second order polynomial. Additionally the signal (green) and sideband regions (blue) are shown.

### 5.3. Efficiency

As briefly mentioned in Chapter 4, the signal Monte Carlo simulations could, naively, be used for a simple one-dimensional estimation of the reconstruction and selection efficiencies. The efficiency  $\varepsilon$  is calculated by

$$\varepsilon = \frac{N_{\text{acc}}}{N_{\text{gen}}} , \quad (5.9)$$

where  $N_{\text{gen}}$  is the number of generated events and the number of accepted events  $N_{\text{acc}}$  is determined by integrating the invariant mass distribution of the MC sample within a signal region that contains 95 % of the signal. However, as shown during background studies in Section 5.1, the data is not evenly distributed in phase space. Hence, it is necessary to carry out a multidimensional efficiency determination. One possibility would be to create a multidimensional efficiency map. In case of the  $p\bar{p}\eta$  final state the system is completely determined by seven coordinates, i.e., five angles and two invariant masses. If these coordinates were divided into 10 bins each, the map would already have  $10^7$  total bins. The sheer amount of MC events needed to achieve a sufficiently small statistical uncertainty in each bin is virtually unavailable. Therefore, a partial wave analysis is performed to obtain a weighted MC sample which is a precise image of the measured data in all coordinates, thus allowing for the naive treatment of the acceptance mentioned above.

### 5.4. Partial Wave Analysis

Partial wave analysis (PWA) is one of the most sophisticated tools used in hadron spectroscopy and is based on scattering theory, allowing for a decomposition of the observed total amplitude into partial wave contributions. An introduction to the basic concepts and formalisms involved is given in the following and a more detailed description can be found in [109, 110].

#### 5.4.1. Basic Concepts and Formalisms

The amplitude used in this analysis is based on the isobar model. Final states, such as  $p\bar{p}\eta$ , are described by a sequence of two-body decays of short-lived intermediate resonances

$$\gamma^* \rightarrow R\eta, R\rho, R\bar{\rho} \quad \text{and} \quad R \rightarrow p\bar{p}, p\eta, \bar{p}\eta .$$

All amplitudes are described in the helicity formalism, a special choice of a spin formalism. The quantum mechanical state of a free particle at rest can be described by its total angular momentum  $j$  and the projection to an arbitrarily chosen quantization axis

denoted by  $|j, m\rangle$ . A complete set of orthogonal states is called a canonical basis, the base vectors of which fulfill the relations

$$\sum_{j,m} |j, m\rangle \langle j, m| = \mathbf{1} \quad \text{and} \quad \langle j', m' | j, m \rangle = \delta_{j'j} \delta_{m'm} . \quad (5.10)$$

In general, particles have to be described not only at rest, but relativistically with momentum  $\vec{p}$ . In the canonical reference system such a description can be achieved by a Lorentz boost. It is useful to first rotate the coordinate system so that one axis, e.g., the  $z$ -axis, is aligned with  $\vec{p}$ . As shown in [111], a rotation can be written as

$$\hat{r}(\alpha, \beta, \gamma) |j, m\rangle = \sum_{m'} D_{mm'}^j(\alpha, \beta, \gamma) |j, m'\rangle , \quad (5.11)$$

where the unitary operator  $\hat{r}(\alpha, \beta, \gamma)$  acts on the state  $|j, m\rangle$ ,  $\alpha, \beta, \gamma$  are the Euler angles and  $D_{mm'}^j$  are the complex unitary Wigner-D-matrices given by

$$\begin{aligned} \langle j, m' | \hat{r}(\alpha, \beta, \gamma) | j, m \rangle &= \sum_{m''} D_{mm''}^j(\alpha, \beta, \gamma) \langle j, m | j, m'' \rangle \\ &= D_{mm'}^j(\alpha, \beta, \gamma) = e^{-im'\alpha} d_{mm'}^j(\beta) e^{-im\gamma} , \end{aligned} \quad (5.12)$$

where the Wigner-d-matrices can be found in [36].

The helicity  $\lambda$  of a particle is defined as the projection of its total angular momentum  $\vec{J}$  to a quantization axis along the direction of the momentum vector  $\vec{p}$ , given by

$$\lambda = \vec{J} \cdot \hat{p} = \vec{J} \cdot \frac{\vec{p}}{|\vec{p}|} , \quad (5.13)$$

and is therefore invariant under rotations around and boosts along this axis. A transformation into the helicity frame is achieved first applying a rotation so that the  $z$ -axis matches the direction of the particles momentum and then applying a Lorentz boost along this axis. If a particle  $a$  with total angular momentum  $J_a$  and helicity  $\lambda_a$  decays into two daughter particles  $b$  and  $c$ , a transition amplitude can be constructed as shown in detail in [111, 112]

$$A_{\lambda_b \lambda_c}^{J_a, \lambda_a}(a \rightarrow b + c) = \sqrt{\frac{2J_a + 1}{4\pi}} D_{\lambda_a \lambda}^{J_a*}(\varphi, \vartheta, 0) F_{\lambda_b \lambda_c}^{J_a} , \quad (5.14)$$

where  $\lambda_b$  and  $\lambda_c$  are the helicities of the daughter particles with  $\lambda = \lambda_b - \lambda_c$  and  $D_{\lambda_a \lambda}^{J_a*}$  are the Wigner-D functions with azimuthal angle  $\varphi$  and polar angle  $\vartheta$ . The  $F_{\lambda_b \lambda_c}^{J_a}$  represents the fit parameter that has to be optimized. Some of these amplitudes may vanish due to certain symmetries and conservation laws. Resonances studied in this analysis decay via the strong interaction and thus are expected to conserve the total angular momentum  $J$ ,

isospin  $I$ , parity  $P$ , charge conjugation  $C$  and  $G$  parity. For example, if parity  $P$  is conserved, the parameter  $F_{\lambda_b\lambda_c}^{J_a}$  is correlated to  $F_{-\lambda_b-\lambda_c}^{J_a}$  with the relation

$$F_{\lambda_b\lambda_c}^{J_a} = P_a \cdot P_b \cdot P_c \cdot (-1)^{-J_a+J_b+J_c} F_{-\lambda_b-\lambda_c}^{J_a}, \quad (5.15)$$

where  $P_i$  denotes the intrinsic parity and  $J_i$  the total angular momentum of the corresponding particle. The quantum numbers for all  $p\bar{p}m$  final-state particles are

	$p$	$\bar{p}$	$\eta$	$\omega$
$J^{P(C)}$	$\frac{1}{2}^+$	$\frac{1}{2}^-$	$0^{-+}$	$1^{--}$
$I^{(G)}$	$\frac{1}{2}$	$\frac{1}{2}$	$0^+$	$0^-$

While the  $\eta$  meson is treated as a stable particle, the three-body decay of the  $\omega$  meson is handled separately with the amplitude

$$A_{\lambda_\omega}^{J_\omega}(\omega \rightarrow \pi^+\pi^-\pi^0) = \sqrt{\frac{3}{4\pi}} \cdot D_{\lambda_\omega\mu}^{1*}(\varphi_n, \vartheta_n, 0) \cdot \tilde{\lambda}_\mu, \quad (5.16)$$

where  $\tilde{\lambda}$  is the slope of the  $\omega \rightarrow \pi^+\pi^-\pi^0$  Dalitz plot, characterized by the cross product of the two charged pion momenta  $\tilde{\lambda} = |\vec{p}_{\pi^+} \times \vec{p}_{\pi^-}|^2$  in the  $\omega$  helicity frame. The normal vector  $\vec{n}$  to the decay plane of all daughter particles is described by the Euler angles  $\varphi_n, \vartheta_n$  and  $\gamma_n \equiv 0$ . The projection of the spin  $\mu = \vec{J}_\omega \cdot \vec{n}$  has to be zero for this decay [113]. Since the angular momentum  $L$  between the daughter particles and the spin  $S$  are good quantum numbers to describe the system, helicity amplitudes in this work are transformed once more into the so-called  $LS$  basis. The transformation is given in [110] as

$$F_{\lambda_b\lambda_c}^{J_a} = \sum_{L,S} \sqrt{\frac{2L+1}{2J_a+1}} \langle L, 0; S, \lambda | J_a, \lambda \rangle \langle J_b, \lambda_b; J_c, -\lambda_c | S, \lambda \rangle \cdot \alpha_{LS}^{J_a}, \quad (5.17)$$

where  $L$  and  $S$  are limited by  $|J_b - J_c| \leq S \leq |J_b + J_c|$  and  $|L - S| \leq J_a \leq |L + S|$ .  $\langle J_b, \lambda_b; J_c, -\lambda_c | S, \lambda \rangle$  are Clebsch-Gordan coefficients, which can be found in [36].

A common parameterization of the dynamical part of the amplitude for an isolated resonance with mass  $m_0$  and width  $\Gamma$  is given by the relativistic Breit-Wigner function written as

$$BW(m) = \frac{m_0 \Gamma B_L(q, q_0)}{m_0^2 - m^2 - i(\rho/\rho_0)m_0 \Gamma B_L^2(q, q_0)}, \quad (5.18)$$

with phase space factors  $\rho$  and  $\rho_0 = \rho(m_0)$  given by

$$\rho(m) = \sqrt{\left(1 - \left(\frac{m_b + m_c}{m}\right)^2\right) \cdot \left(1 - \left(\frac{m_b - m_c}{m}\right)^2\right)}. \quad (5.19)$$

$B_L(q, q_0)$  are the Blatt-Weisskopf centrifugal barrier factors, which describe a distortion of the line shape based on the angular momentum  $L$  and momentum  $q$  of the daughter



particles of a decaying resonance. Two-particle interactions are negligible outside an interaction radius  $r$ . The barrier factors can be calculated in the form

$$B_L(q, q_0) = \frac{b_L(q)}{b_L(q_0)}, \quad (5.20)$$

where  $b_L(z)$  for angular momenta up to  $L = 4$  are given in Table 5.3 with  $z = \frac{qr}{\hbar c}$  [114]. In this analysis a radius  $r = 0.66$  fm is used.

**Table 5.3.:** Blatt-Weisskopf barrier factors for angular momenta up to  $L = 4$  [114].

$L$	$b_L(z)$
0	1
1	$\sqrt{\frac{2z}{z+1}}$
2	$\sqrt{\frac{13z^2}{(z-3)^2+9z}}$
3	$\sqrt{\frac{277z^3}{z(z-15)^2+9(2z-5)^2}}$
4	$\sqrt{\frac{12746z^4}{(z^2-45z+105)^2+25z(2z-21)^2}}$

#### 5.4.2. Analysis Software Package PAWIAN

The partial wave analysis presented in this work is performed with the software package PAWIAN (Partial Wave Interactive Analysis) [115]. It follows an object-oriented approach and makes use of external packages such as qft++ [116], which facilitates numerical quantum field theory calculations and is used for evaluation of Clebsch-Gordan coefficients and Wigner-D-matrices. The minimization is realized by an event based maximum likelihood fit using the MINUIT2 package [108]. Production and decay amplitudes can be described in different spin formalisms, e.g., the canonical, helicity and covariant tensor formalisms. The dynamical part of the amplitudes can be individually parameterized by a Breit-Wigner, Flatté or K-matrix, as well as user-defined parameterizations thanks to the highly modular design. PAWIAN also provides basic tools to perform a coupled channel analysis, which is used for the two decay modes of the  $p\bar{p}\eta$  final state.

#### 5.4.3. PWA Contributions and Results

Before a partial wave analysis can be performed one has to address the remaining background events. Here a sideband method is used, where events from the sideband regions get a negatively weighted likelihood to account for the background under the peak. Since only an effective description of the data is intended for an accurate efficiency determination, a choice of contributing resonances is made as listed in Table 5.4 with their corresponding quantum numbers  $J^{PC}$ . The resonances are only used to represent the

**Table 5.4.:** List of intermediate resonances with quantum numbers  $J^{PC}$  and associated decay particles used in the PWA to describe the  $p\bar{p}\eta$  (**left**) and  $p\bar{p}\omega$  (**right**) final states. For the  $p\bar{p}\omega$  final state resonances are chosen exclusively in the  $p\bar{p}$  system.

R	$J^{P(C)}$		R	$J^{PC}$
J/ $\psi$	$1^{--}$	} $p\bar{p}$	PHSP	$0^{-+}$
$\omega$	$1^{--}$		PHSP	$0^{++}$
$\omega_3$	$3^{--}$		PHSP	$2^{++}$
N(1535)	$1/2^-$	} $p\eta$	$\eta(1405)$	$0^{-+}$
N(1720)	$3/2^+$		$\eta(2225)$	$0^{-+}$
$\bar{N}(1535)$	$1/2^+$	} $\bar{p}\eta$	$f_0(1500)$	$0^{++}$
$\bar{N}(1720)$	$3/2^-$		$f_0(2100)$	$0^{++}$
			$f_2(1950)$	$2^{++}$
			$f_2(2150)$	$2^{++}$

respective set of quantum numbers and should certainly not be associated with physical resonances. Mass  $m$  and width  $\Gamma$  of these intermediate resonances are left free in the fit, except for the J/ $\psi$ , which is described by a Voigt amplitude, the convolution of a Breit-Wigner and a Gaussian distribution, with Breit-Wigner mass and width being fixed to values from the PDG [36]. A contribution of J/ $\psi$  is possible in the  $p\bar{p}\eta$  final state by the process  $e^+e^- \rightarrow \eta(J/\psi \rightarrow p\bar{p})$ , which will be discussed in more detail in Section 5.8. In the partial wave analysis, the J/ $\psi$  is only included in case its significance is greater than  $3\sigma$ . A significant contribution is seen in five data sets (4.1784, 4.1888, 4.1989, 4.2092 and 4.2263 GeV). Both channels,  $\eta \rightarrow \gamma\gamma$  and  $\eta \rightarrow \pi^+\pi^-\pi^0$ , are handled simultaneously in the fit. Final results of the PWA are shown in Figures 5.8 to 5.11 for the two data sets with the highest statistics, one with contribution of a J/ $\psi$  resonance (4.1784 GeV) and one without (3.7730 GeV).

Since there are no significant couplings of  $N^*$  to  $p\omega$  [36], the  $p\bar{p}\omega$  final state is described by adding resonances exclusively in the  $p\bar{p}$  system. Additional phase space contributions are denoted by PHSP, where the dynamical part of the amplitude is set constant, i.e., this mass coordinate has the form of the signal MC, and the angular distributions are generated according to the quantum numbers  $J^{PC}$ . Results are also shown for the data set with highest statistics in Figure 5.12. It should be re-emphasized here, that the main objective was an effective description of the data. Thus, intermediate states outside the J/ $\psi$  are to be treated as effective parameterizations of the data and do not reflect properties of physical resonances, especially as all masses and widths are left free in the fit and the statistics is certainly not enough to determine physically meaningful masses and widths.

The efficiencies can then be calculated using event weights according to the PWA solutions and integrating all events within the signal region. Figure 5.7 shows the results of the partial wave analysis compared to a simple one-dimensional estimation. A significant difference between both methods can be observed with relative changes of up to 22 %. However, these changes appear to be quite constant in the entire energy range. Such a behavior can be explained by the fact that the center-of-mass energies of all 17 data sets are far from threshold for both final states,  $p\bar{p}\eta$  and  $p\bar{p}\omega$ . In particular, this constant shift cannot produce any unphysical structures in the cross section.

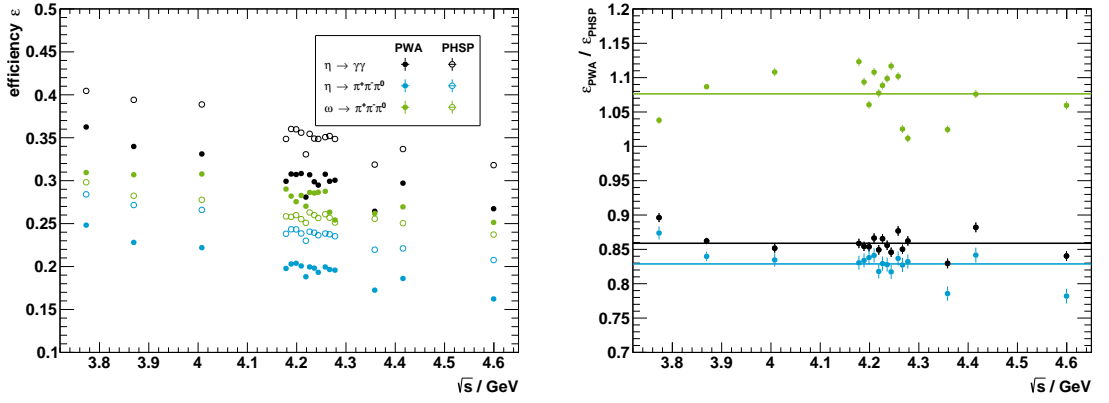


**Figure 5.7.:** **Left:** Efficiencies of the  $\eta \rightarrow \gamma\gamma$  (black),  $\eta \rightarrow \pi^+\pi^-\pi^0$  (blue) and  $\omega \rightarrow \pi^+\pi^-\pi^0$  (green) decay modes determined with a partial wave analysis (filled dots) or simply using the MC simulations (open circles) for all 17 data sets. **Right:** Relative difference of the efficiencies between the two determination methods as well as their weighted averages represented by solid lines.

## 5. Analysis of $e^+e^- \rightarrow p\bar{p}\eta$ and $e^+e^- \rightarrow p\bar{p}\omega$

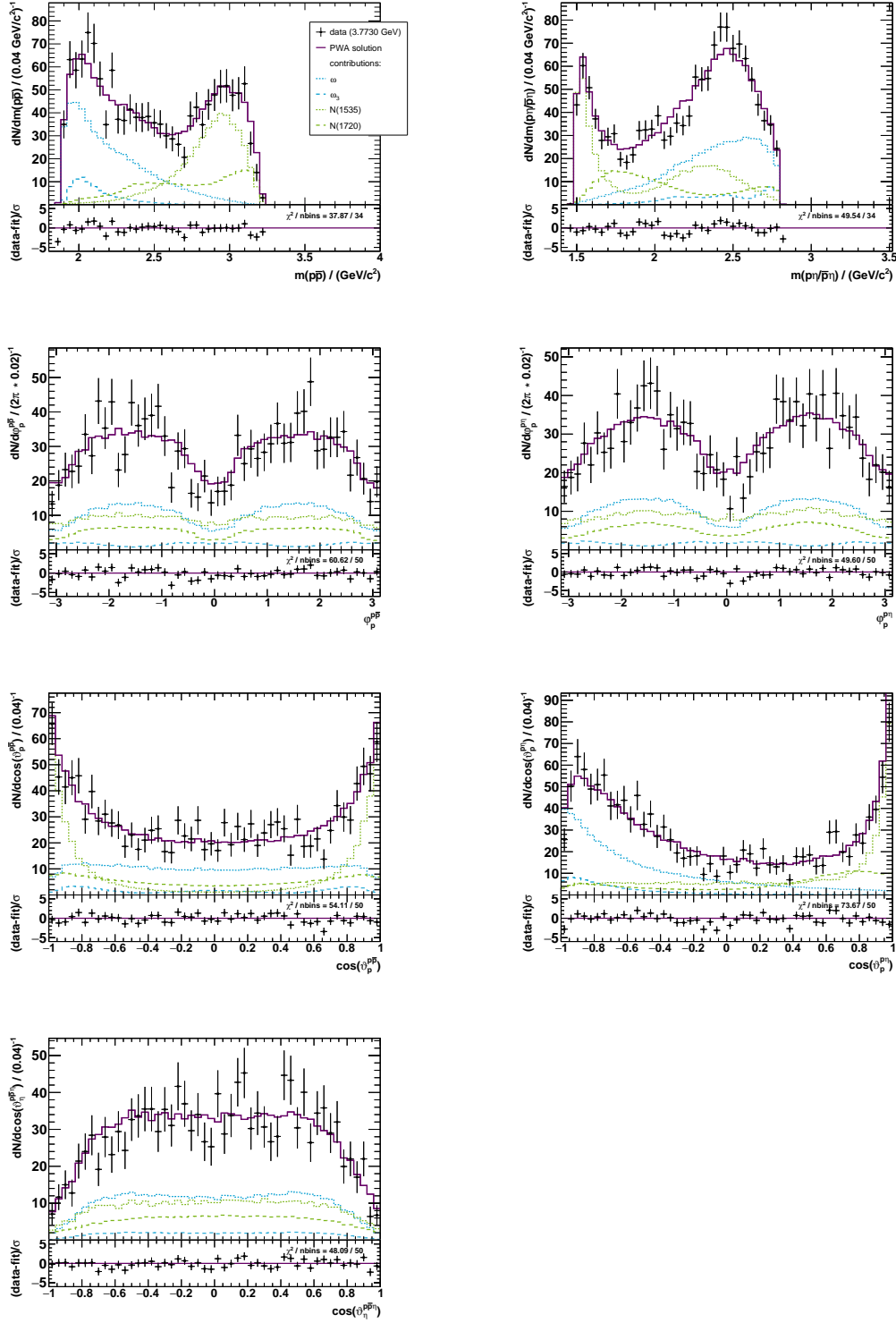


**Figure 5.8.:** Final results of the partial wave analysis for the  $\eta \rightarrow \gamma\gamma$  decay mode at a center-of-mass energy of 3.7730 GeV. The PWA solution and individual contributions are represented by solid and dashed lines, respectively. The angle notation  $\phi_p^{p\bar{p}}$  means the azimuthal angle of the proton in the  $p\bar{p}$  system.

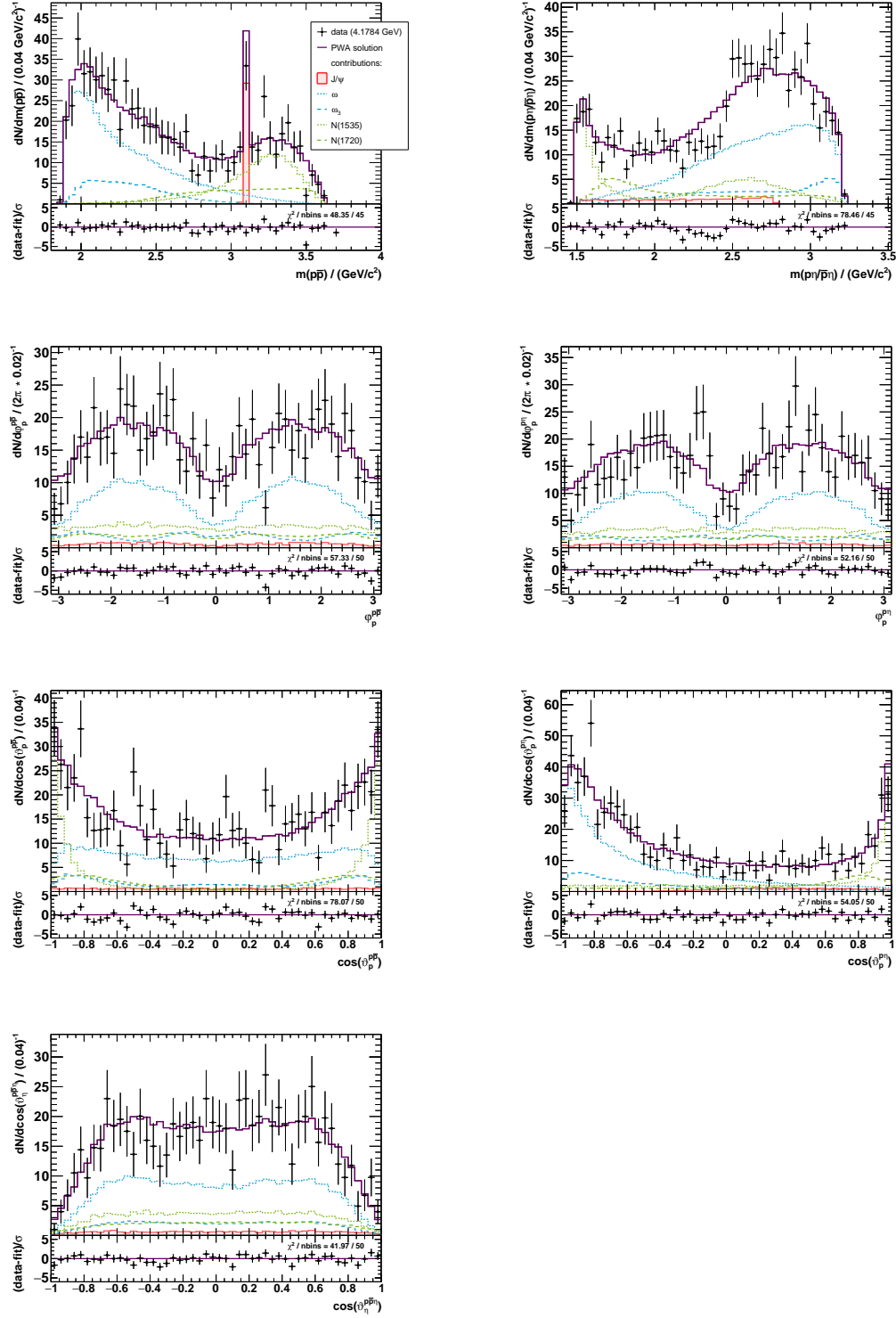


**Figure 5.9.:** Final results of the partial wave analysis for the  $\eta \rightarrow \gamma\gamma$  decay mode at a center-of-mass energy of 4.1784 GeV. The PWA solution and individual contributions are represented by solid and dashed lines, respectively. The angle notation  $\phi_p^{\text{p}\bar{\text{p}}}$  means the azimuthal angle of the proton in the  $\text{p}\bar{\text{p}}$  system.

## 5. Analysis of $e^+e^- \rightarrow p\bar{p}\eta$ and $e^+e^- \rightarrow p\bar{p}\omega$

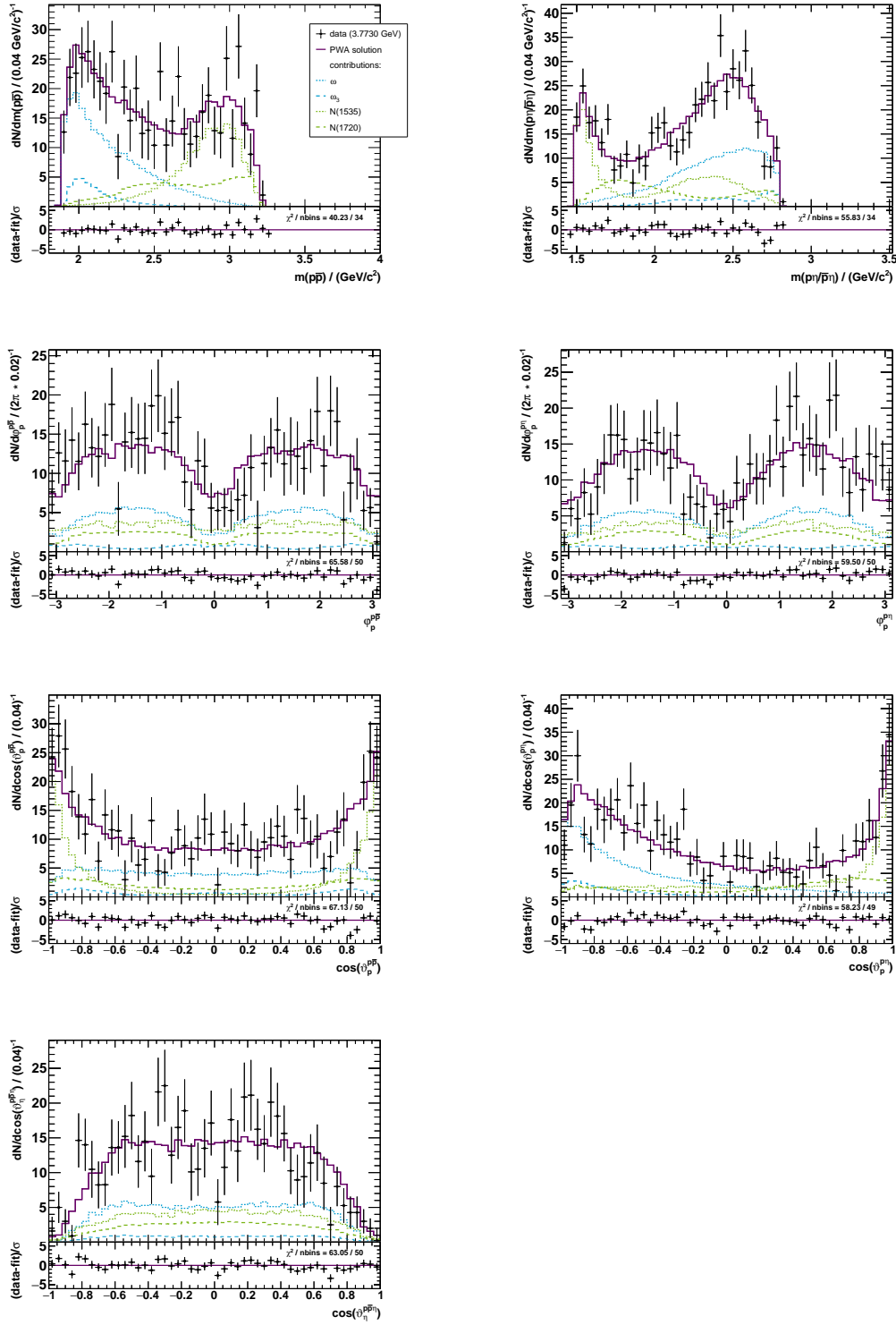


**Figure 5.10.:** Final results of the partial wave analysis for the  $\eta \rightarrow \pi^+\pi^-\pi^0$  decay mode at a center-of-mass energy of 3.7730 GeV. The PWA solution and individual contributions are represented by solid and dashed lines, respectively. The angle notation  $\varphi_p^{p\bar{p}}$  means the azimuthal angle of the proton in the  $p\bar{p}$  system.

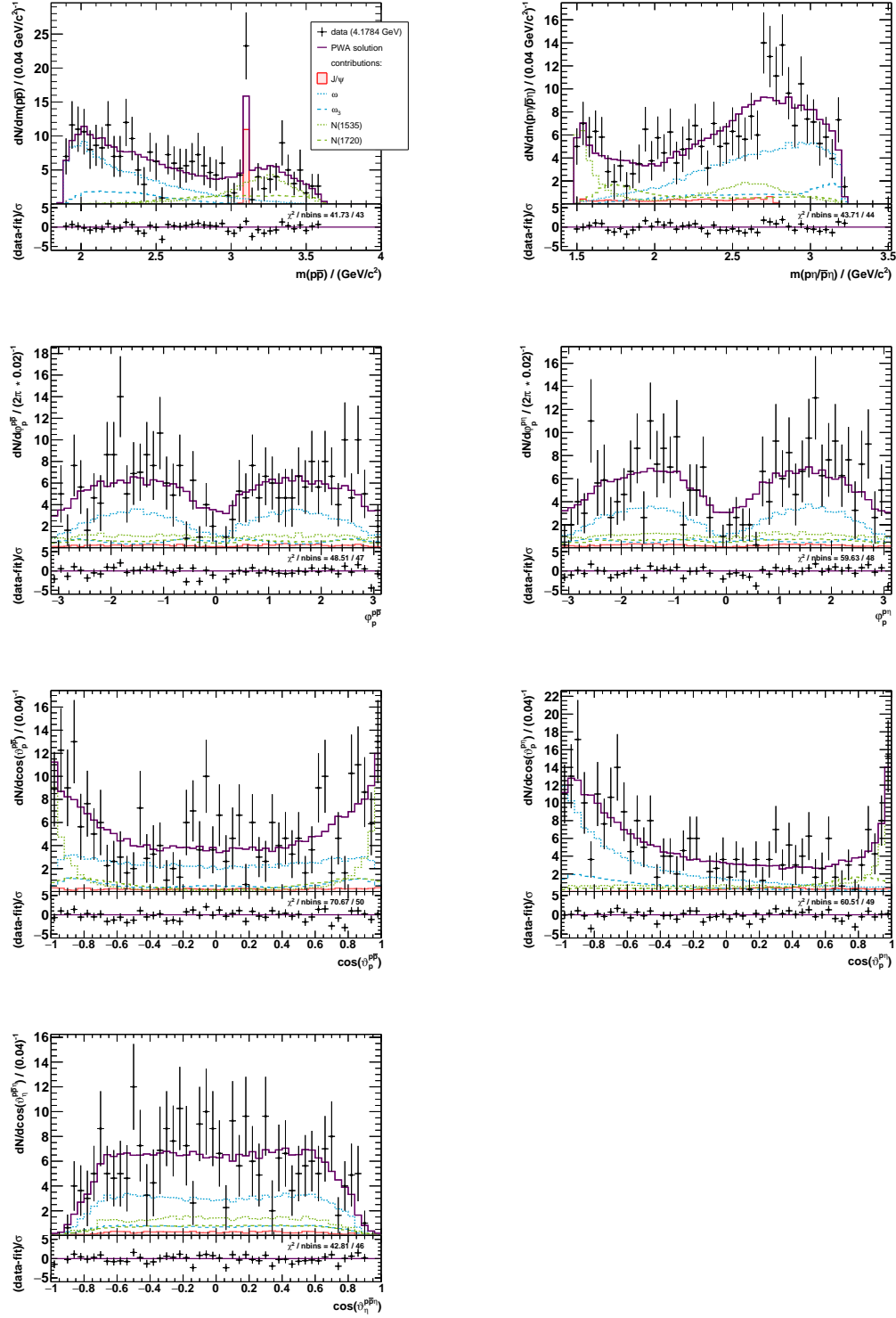


**Figure 5.11.:** Final results of the partial wave analysis for the  $\eta \rightarrow \pi^+\pi^-\pi^0$  decay mode at a center-of-mass energy of 4.1784 GeV. The PWA solution and individual contributions are represented by solid and dashed lines, respectively. The angle notation  $\varphi_p^{p\bar{p}}$  means the azimuthal angle of the proton in the  $p\bar{p}$  system.

## 5. Analysis of $e^+e^- \rightarrow p\bar{p}\eta$ and $e^+e^- \rightarrow p\bar{p}\omega$

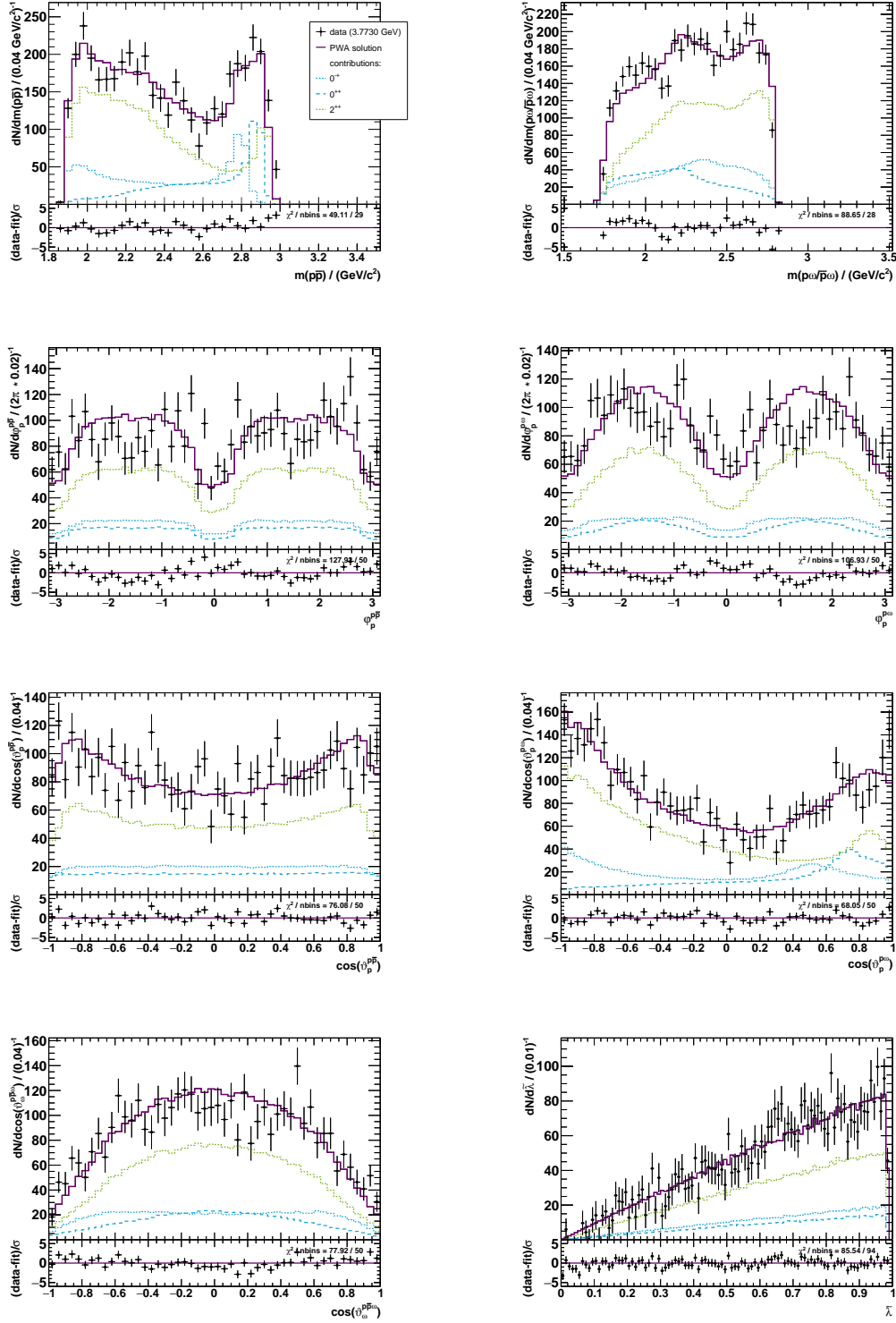


**Figure 5.12.:** Final results of the partial wave analysis for the  $\omega \rightarrow \pi^+\pi^-\pi^0$  decay mode at a center-of-mass energy of 3.7730 GeV. The PWA solution and individual contributions are represented by solid and dashed lines, respectively. The angle notation  $\varphi_p^{p\bar{p}}$  means the azimuthal angle of the proton in the  $p\bar{p}$  system.  $\tilde{\lambda}$  is the Dalitz plot slope as described in the text.



## 5.5. Radiative Correction Factors

In quantum field theory, describing a process like  $e^+e^- \rightarrow p\bar{p}m$  can quickly become infinitely complex. To facilitate the comparison of an experimental observation with a theoretical model, it is common practice to calculate the Born cross section, i.e., the cross section of the process at lowest order in perturbation theory. Schematic diagrams of the process studied in this work at leading order as well as three higher order contributions are shown in Figure 5.13. An example of an effect beyond leading order is initial-state radiation. Charged particles can decelerate and emit a real photon. If, for example, the electron or positron emits a photon before annihilation, it is called initial-state radiation (ISR). Equivalent to this, there is also final-state radiation (FSR). Additionally, a photon emitted by the electron can be reabsorbed by the positron and vice versa, which is called vertex correction. Besides these radiative corrections to the leading order process, there is another higher order effect that is usually corrected for. The virtual photon can produce a fermion-antifermion pair, which then annihilates again into a virtual photon. This effect is called vacuum polarization (VP) and can be described as a small correction to the leading order process given by

$$(1 + \delta_v) = \frac{1}{|1 - \Pi(s)|^2} , \quad (5.21)$$

where  $\Pi(s)$  is the vacuum polarization tensor depending on the available energy  $s$ . These VP corrections, including leptonic and hadronic contributions, are calculated with the alphaQED software package [117] with an accuracy of 0.5 %. Radiative corrections  $(1 + \delta_r)$  can have an effect on the reconstruction efficiency  $\varepsilon$  and are therefore determined with the ConExc Monte Carlo generator using an iterative approach. A flat line shape of the Born cross section is used as a starting point and the resulting cross sections are used as input for the next iteration until the radiative correction dependent quantity  $\kappa = \varepsilon(1 + \delta_r)$  converges, as shown in Figure 5.14. The result is considered to be converged if the ratio  $\kappa_i/\kappa_{i-1}$  of two successive iterations is compatible with one. It should be noted here that during the iterative procedure, efficiencies were determined using the signal Monte Carlo simulations evenly generated in phase space. A partial wave analysis, as described in Section 5.4, was performed exclusively after the last and final iteration. This is justified because the difference in efficiency is approximately constant in the entire energy range and thus has no influence on the iterative procedure.

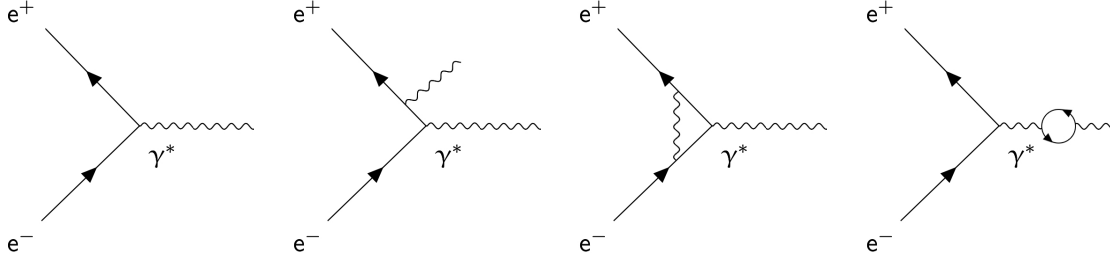


**Figure 5.13.:** Schematic diagrams which contribute to the process  $e^+e^- \rightarrow p\bar{p}m$ . The leading order process is shown as well as three examples of higher order effects: Initial-state radiation, vertex correction and vacuum polarization (from left to right).

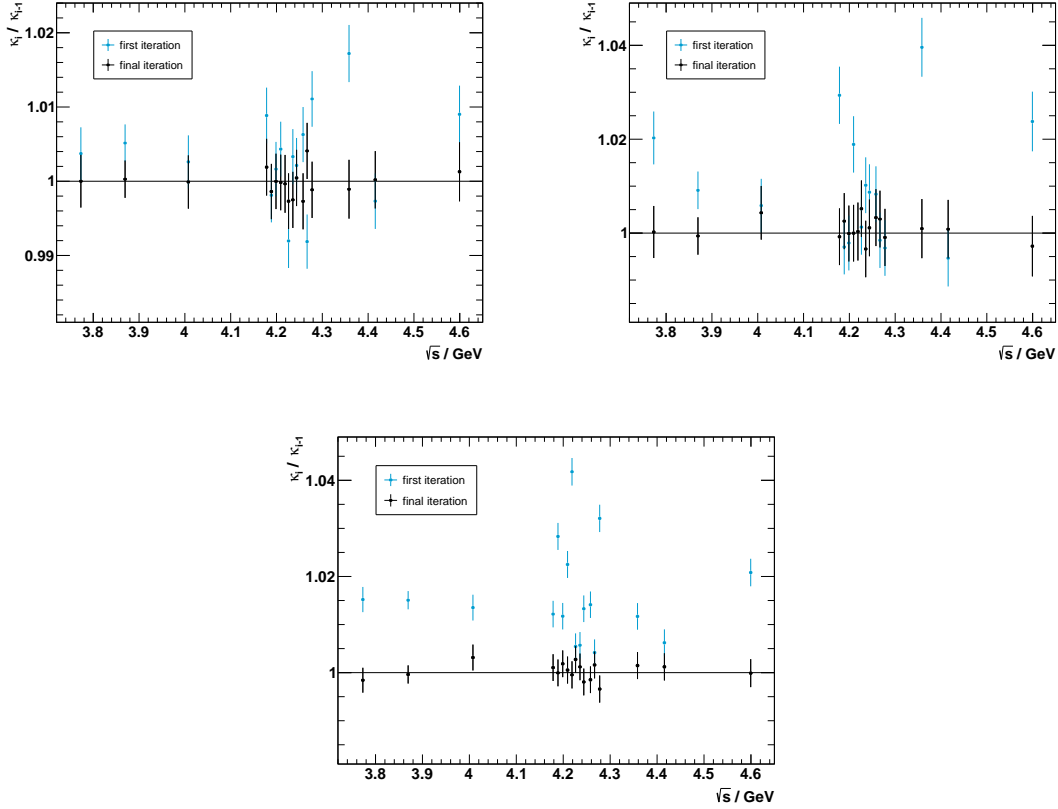


**Figure 5.14.:** Relative difference of the radiative correction dependent quantity  $\kappa$  between iteration  $i$  and the previous iteration  $i - 1$  for  $\eta \rightarrow \gamma\gamma$  (top left),  $\eta \rightarrow \pi^+\pi^-\pi^0$  (top right) and  $\omega \rightarrow \pi^+\pi^-\pi^0$  (bottom).

## 5.6. Born Cross Sections

After all necessary observables have been determined, the Born cross sections can be calculated with Equation (5.1). Results are listed in Tables 5.5 to 5.7 and are graphically depicted in Figure 5.15. Branching fractions are taken from the PDG [36] and integrated luminosities were measured based on the Bhabha scattering process  $e^+e^- \rightarrow (\gamma)e^+e^-$  [88]. The remaining values are determined as described in the previous sections. A combined Born cross section of the two different  $\eta$  decay modes is calculated with a weighted squares method [33]. The weighted average cross section value  $\bar{x}$  and its associated uncertainty  $\delta\bar{x}$  can be written as

$$\bar{x} \pm \delta\bar{x} = \frac{\sum_j x_j \cdot \sum_i \omega_{ij}}{\sum_i \sum_j \omega_{ij}} \pm \sqrt{\frac{1}{\sum_i \sum_j \omega_{ij}}} , \quad (5.22)$$

with  $\omega_{ij}$  being an element of  $V^{-1}$ , the inverse of the covariance matrix  $V$  given by

$$V = \begin{pmatrix} \sigma_{t1}^2 & cov(x_1, x_2) & \cdots & cov(x_1, x_n) \\ cov(x_2, x_1) & \sigma_{t2}^2 & \cdots & cov(x_2, x_n) \\ \vdots & \vdots & \ddots & \vdots \\ cov(x_n, x_1) & cov(x_n, x_2) & \cdots & \sigma_{tn}^2 \end{pmatrix} , \quad (5.23)$$

$$\sigma_{ti}^2 = \sigma_i^2(\text{stat.}) + \sum_k \sigma_{ik}^2(\text{sys. } k) , \quad (5.24)$$

$$cov(x_i, x_j) = x_i \cdot \rho_{ij} \cdot x_j \cdot \rho_{ji} , \quad (5.25)$$

where  $\sigma_{ti}^2$  is the total uncertainty in mode  $i$ , the squared sum of the statistical  $\sigma_i^2(\text{stat.})$  and all systematic uncertainties  $\sigma_{ik}^2(\text{sys. } k)$  from source  $k$ .  $cov(x_i, x_n)$  is the systematic uncertainty between mode  $i$  and  $j$ , with measured values  $x_i$  and common relative systematics  $\rho_{ij}$ . All uncertainties that are shown so far are statistical uncertainties only. Systematical uncertainties will be discussed in the following section.

## 5. Analysis of $e^+e^- \rightarrow p\bar{p}\eta$ and $e^+e^- \rightarrow p\bar{p}\omega$

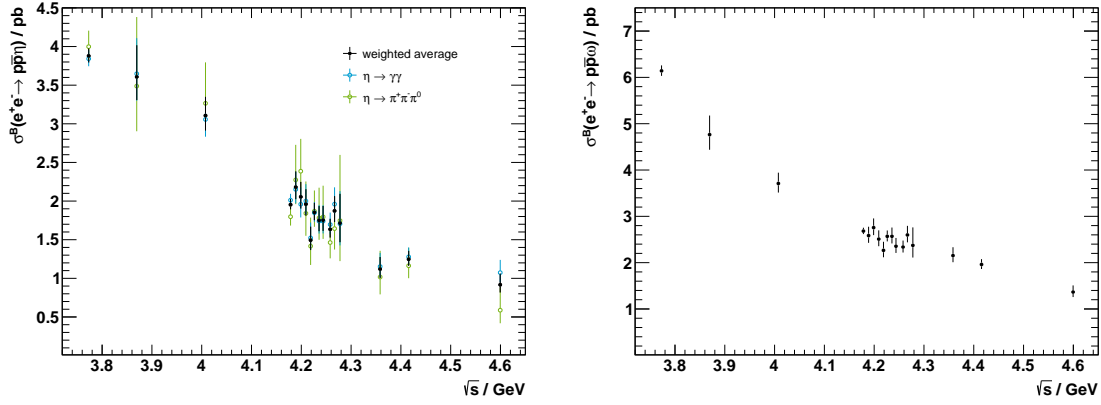


**Figure 5.15.:** Calculated Born cross sections  $\sigma^B$  for the  $p\bar{p}\eta$  (left) and  $p\bar{p}\omega$  (right) final states with corresponding statistical uncertainties. The cross sections of the two  $\eta$  meson decay modes are shown in comparison to their weighted average.

**Table 5.5.:** Center-of-mass energies  $\sqrt{s}$ , integrated luminosities  $L$ , correction factors for initial-state radiation ( $1 + \delta_r$ ) and vacuum polarization ( $1 + \delta_v$ ) as well as number of observed events  $N_{\text{obs}}$ , efficiencies  $\varepsilon$  and the calculated Born cross sections  $\sigma^B(e^+e^- \rightarrow p\bar{p}\eta)$  for the  $\eta \rightarrow \gamma\gamma$  decay mode with their corresponding statistical uncertainties.

$\sqrt{s} / \text{GeV}$	$L / \text{pb}^{-1}$	$(1 + \delta_r)$	$(1 + \delta_v)$	$N_{\text{obs}}$	$\varepsilon / \%$	$\sigma^B / \text{pb}$
3.7730	2931.8	0.8993	1.0570	$1521.9^{+42.8}_{-38.2}$	$36.3 \pm 0.1$	$3.82^{+0.11}_{-0.10}$
3.8695	224.0	0.9290	1.0507	$106.8^{+13.5}_{-10.2}$	$34.0 \pm 0.1$	$3.65^{+0.46}_{-0.35}$
4.0076	482.0	0.9553	1.0438	$191.7^{+17.1}_{-14.0}$	$33.1 \pm 0.1$	$3.06^{+0.27}_{-0.22}$
4.1784	3189.0	1.0398	1.0543	$829.5^{+33.9}_{-29.1}$	$30.0 \pm 0.1$	$2.01^{+0.08}_{-0.07}$
4.1888	524.6	1.0034	1.0559	$145.0^{+15.3}_{-12.1}$	$30.8 \pm 0.1$	$2.15^{+0.23}_{-0.18}$
4.1989	526.0	1.0156	1.0567	$133.9^{+14.9}_{-11.7}$	$30.7 \pm 0.1$	$1.96^{+0.22}_{-0.17}$
4.2092	518.0	1.0240	1.0565	$136.2^{+14.9}_{-11.7}$	$30.8 \pm 0.1$	$2.00^{+0.22}_{-0.17}$
4.2187	514.6	1.1701	1.0564	$107.2^{+14.0}_{-10.6}$	$28.1 \pm 0.1$	$1.52^{+0.20}_{-0.15}$
4.2263	1056.4	1.0228	1.0562	$255.1^{+19.2}_{-16.1}$	$30.7 \pm 0.1$	$1.85^{+0.14}_{-0.12}$
4.2357	530.3	1.0569	1.0554	$121.2^{+14.6}_{-11.2}$	$29.9 \pm 0.1$	$1.74^{+0.21}_{-0.16}$
4.2438	538.1	1.0464	1.0555	$120.2^{+14.2}_{-11.0}$	$29.5 \pm 0.1$	$1.74^{+0.21}_{-0.16}$
4.2580	828.4	1.0536	1.0534	$189.0^{+17.2}_{-13.9}$	$30.7 \pm 0.1$	$1.70^{+0.15}_{-0.12}$
4.2668	531.1	1.0238	1.0532	$132.4^{+14.7}_{-11.5}$	$29.9 \pm 0.1$	$1.96^{+0.22}_{-0.17}$
4.2777	175.7	1.0463	1.0530	$39.1^{+9.7}_{-6.4}$	$30.1 \pm 0.1$	$1.71^{+0.42}_{-0.28}$
4.3583	543.9	1.1749	1.0511	$80.7^{+12.3}_{-9.2}$	$26.4 \pm 0.1$	$1.15^{+0.18}_{-0.13}$
4.4156	1043.9	1.0714	1.0524	$176.1^{+16.8}_{-13.5}$	$29.7 \pm 0.1$	$1.28^{+0.12}_{-0.10}$
4.5995	586.9	1.1439	1.0547	$80.1^{+12.3}_{-9.2}$	$26.7 \pm 0.1$	$1.07^{+0.16}_{-0.12}$

**Table 5.6.:** Center-of-mass energies  $\sqrt{s}$ , integrated luminosities  $L$ , correction factors for initial-state radiation  $(1 + \delta_r)$  and vacuum polarization  $(1 + \delta_v)$  as well as number of observed events  $N_{\text{obs}}$ , efficiencies  $\varepsilon$  and the calculated Born cross sections  $\sigma^B(e^+e^- \rightarrow p\bar{p}\eta)$  for the  $\eta \rightarrow \pi^+\pi^-\pi^0$  decay mode with their corresponding statistical uncertainties.

$\sqrt{s}$ / GeV	$L$ / pb $^{-1}$	$(1 + \delta_r)$	$(1 + \delta_v)$	$N_{\text{obs}}$	$\varepsilon$ / %	$\sigma^B$ / pb
3.7730	2931.8	0.8993	1.0570	$627.1^{+32.2}_{-27.4}$	$24.8 \pm 0.1$	$4.00^{+0.21}_{-0.18}$
3.8695	224.0	0.9290	1.0507	$39.9^{+10.1}_{-6.6}$	$22.8 \pm 0.1$	$3.53^{+0.89}_{-0.58}$
4.0076	482.0	0.9553	1.0438	$78.9^{+12.8}_{-9.5}$	$22.2 \pm 0.1$	$3.27^{+0.53}_{-0.39}$
4.1784	3189.0	1.0398	1.0543	$282.8^{+22.5}_{-17.9}$	$19.8 \pm 0.1$	$1.81^{+0.14}_{-0.11}$
4.1888	524.6	1.0034	1.0559	$58.2^{+11.6}_{-8.0}$	$20.3 \pm 0.1$	$2.28^{+0.45}_{-0.31}$
4.1989	526.0	1.0156	1.0567	$62.8^{+10.9}_{-8.3}$	$20.4 \pm 0.1$	$2.41^{+0.42}_{-0.32}$
4.2092	518.0	1.0240	1.0565	$47.3^{+10.5}_{-7.4}$	$20.1 \pm 0.1$	$1.86^{+0.41}_{-0.29}$
4.2187	514.6	1.1701	1.0564	$38.4^{+10.0}_{-6.6}$	$18.8 \pm 0.1$	$1.42^{+0.37}_{-0.24}$
4.2263	1056.4	1.0228	1.0562	$96.9^{+13.8}_{-10.4}$	$20.0 \pm 0.1$	$1.88^{+0.27}_{-0.20}$
4.2357	530.3	1.0569	1.0554	$47.3^{+10.4}_{-7.5}$	$19.8 \pm 0.1$	$1.78^{+0.39}_{-0.28}$
4.2438	538.1	1.0464	1.0555	$46.7^{+10.5}_{-7.4}$	$19.3 \pm 0.1$	$1.80^{+0.40}_{-0.28}$
4.2580	828.4	1.0536	1.0534	$61.1^{+11.9}_{-8.5}$	$20.0 \pm 0.1$	$1.47^{+0.29}_{-0.20}$
4.2668	531.1	1.0238	1.0532	$42.1^{+10.3}_{-6.9}$	$19.7 \pm 0.1$	$1.65^{+0.40}_{-0.27}$
4.2777	175.7	1.0463	1.0530	$15.0^{+7.3}_{-4.5}$	$19.6 \pm 0.1$	$1.75^{+0.85}_{-0.52}$
4.3583	543.9	1.1749	1.0511	$26.7^{+8.9}_{-5.9}$	$17.3 \pm 0.1$	$1.02^{+0.34}_{-0.22}$
4.4156	1043.9	1.0714	1.0524	$57.7^{+11.5}_{-7.0}$	$18.6 \pm 0.1$	$1.16^{+0.23}_{-0.16}$
4.5995	586.9	1.1439	1.0547	$15.5^{+7.6}_{-4.4}$	$16.2 \pm 0.1$	$0.60^{+0.29}_{-0.17}$

**Table 5.7.:** Center-of-mass energies  $\sqrt{s}$ , integrated luminosities  $L$ , correction factors for initial-state radiation  $(1 + \delta_r)$  and vacuum polarization  $(1 + \delta_v)$  as well as number of observed events  $N_{\text{obs}}$ , efficiencies  $\varepsilon$  and the calculated Born cross sections  $\sigma^B(e^+e^- \rightarrow p\bar{p}\omega)$  for the  $\omega \rightarrow \pi^+\pi^-\pi^0$  decay mode with their corresponding statistical uncertainties.

$\sqrt{s}$ / GeV	$L$ / pb $^{-1}$	$(1 + \delta_r)$	$(1 + \delta_v)$	$N_{\text{obs}}$	$\varepsilon$ / %	$\sigma^B$ / pb
3.7730	2931.8	0.8978	1.0570	4623.7 $^{+89.1}_{-81.8}$	$30.9 \pm 0.1$	6.11 $^{+0.12}_{-0.11}$
3.8695	224.0	0.9417	1.0507	285.7 $^{+24.7}_{-19.6}$	$30.7 \pm 0.1$	4.76 $^{+0.41}_{-0.33}$
4.0076	482.0	0.9832	1.0438	485.4 $^{+30.7}_{-25.8}$	$30.8 \pm 0.1$	3.71 $^{+0.23}_{-0.20}$
4.1784	3189.0	1.0220	1.0543	2357.9 $^{+63.9}_{-56.6}$	$29.0 \pm 0.1$	2.68 $^{+0.07}_{-0.06}$
4.1888	524.6	1.0406	1.0559	370.4 $^{+27.4}_{-22.4}$	$28.2 \pm 0.1$	2.58 $^{+0.19}_{-0.16}$
4.1989	526.0	1.0217	1.0567	380.3 $^{+27.3}_{-22.4}$	$27.6 \pm 0.1$	2.76 $^{+0.20}_{-0.16}$
4.2092	518.0	1.0393	1.0565	355.7 $^{+26.7}_{-21.8}$	$28.3 \pm 0.1$	2.51 $^{+0.19}_{-0.15}$
4.2187	514.6	1.0869	1.0564	319.3 $^{+25.8}_{-20.8}$	$27.0 \pm 0.1$	2.27 $^{+0.19}_{-0.15}$
4.2263	1056.4	1.0145	1.0562	733.8 $^{+36.0}_{-31.3}$	$28.6 \pm 0.1$	2.57 $^{+0.13}_{-0.11}$
4.2357	530.3	1.0189	1.0554	371.0 $^{+27.4}_{-22.4}$	$28.6 \pm 0.1$	2.57 $^{+0.19}_{-0.15}$
4.2438	538.1	1.0463	1.0555	353.4 $^{+26.7}_{-21.8}$	$28.7 \pm 0.1$	2.36 $^{+0.18}_{-0.15}$
4.2580	828.4	1.0424	1.0534	539.1 $^{+32.3}_{-27.3}$	$28.8 \pm 0.1$	2.34 $^{+0.14}_{-0.12}$
4.2668	531.1	1.0287	1.0532	347.0 $^{+26.2}_{-21.3}$	$26.3 \pm 0.1$	2.60 $^{+0.20}_{-0.16}$
4.2777	175.7	1.0823	1.0530	106.4 $^{+17.6}_{-11.8}$	$25.4 \pm 0.1$	2.37 $^{+0.39}_{-0.26}$
4.3583	543.9	1.0569	1.0511	300.3 $^{+25.1}_{-20.0}$	$26.2 \pm 0.1$	2.15 $^{+0.18}_{-0.14}$
4.4156	1043.9	1.0554	1.0524	540.0 $^{+31.7}_{-26.8}$	$26.9 \pm 0.1$	1.96 $^{+0.12}_{-0.10}$
4.5995	586.9	1.1230	1.0547	210.4 $^{+22.0}_{-16.7}$	$25.1 \pm 0.1$	1.37 $^{+0.14}_{-0.11}$

## 5.7. Systematic Uncertainties

Studying systematic effects is an essential part of every physics analysis, since they can have a sizeable influence on a measurement. A summary of the systematics which have been determined in previous work of the BESIII collaboration can be found in Table 5.8. Integrated luminosities were measured based on the Bhabha scattering process  $e^+e^- \rightarrow (\gamma)e^+e^-$  with an uncertainty of 1 % [88]. The systematic uncertainty of the tracking efficiency is estimated to be 1 % per track using a  $J/\psi \rightarrow p\bar{p}\pi^+\pi^-$  control sample [118]. Photon detection efficiencies were studied using a  $J/\psi \rightarrow \rho\pi$  control sample and a 1 % systematic uncertainty is estimated for each photon [119]. The uncertainty of the PID efficiency is 1 % for both protons and pions [120]. Branching fractions are taken from the PDG [36]. Systematic uncertainties of subsequent  $\pi^0$  decays can be neglected as the branching fraction  $\mathcal{B}r(\pi^0 \rightarrow \gamma\gamma) = 98.823(34)\%$  [36] is known at sub-permille level. Besides these more general systematics, there are also some uncertainties, which depend specifically on this analysis and have to be considered as described in the following sections.

**Table 5.8.:** Systematic uncertainties in % for the  $p\bar{p}\eta$  and  $p\bar{p}\omega$  final states, which have been determined in previous work of the BESIII collaboration.

	$\eta \rightarrow$		$\omega \rightarrow$
	$\gamma\gamma$	$\pi^+\pi^-\pi^0$	$\pi^+\pi^-\pi^0$
Luminosity	1.0	1.0	1.0
Tracking efficiency	2.0	4.0	4.0
Photon detection	2.0	2.0	2.0
Particle identification	2.0	4.0	4.0
Branching fraction	0.5	1.2	0.8
Total	3.6	6.2	6.1

### 5.7.1. Kinematic Fit

After the initial track selection a kinematic fit was performed to make a final event selection as described in Chapter 4. In order to increase the signal significance of the  $\eta \rightarrow \gamma\gamma$  decay mode, a cut was applied to the  $\chi^2$  value, which could introduce a systematic effect and has to be studied in more detail. Therefore, the cut is varied around its nominal value of 30 and the resulting Born cross section  $\sigma_i^B$  is calculated as described in Section 5.6. The value of interest is its ratio to the reference value  $\sigma_{\text{ref}}^B$  given by

$$R_{\sigma,i} = \frac{\sigma_i^B}{\sigma_{\text{ref}}^B}, \quad (5.26)$$

with the uncertainty

$$\Delta R_{\sigma,i} = \left[ \left( \frac{\partial R_{\sigma,i}}{\partial \sigma_{\text{ref}}^{\text{B}}} \cdot \Delta \sigma_{\text{ref}}^{\text{B}} \right)^2 + \left( \frac{\partial R_{\sigma,i}}{\partial \sigma_i^{\text{B}}} \cdot \Delta \sigma_i^{\text{B}} \right)^2 + 2 \cdot \text{cov}_i \cdot \left( \frac{\partial R_{\sigma,i}}{\partial \sigma_{\text{ref}}^{\text{B}}} \right) \cdot \left( \frac{\partial R_{\sigma,i}}{\partial \sigma_i^{\text{B}}} \right) \right]^{\frac{1}{2}}, \quad (5.27)$$

where  $\frac{\partial R_{\sigma,i}}{\partial \sigma_i^{\text{B}}}$  is the partial derivative of the ratio with respect to the Born cross section and  $\text{cov}_i$  is the covariance, given by  $\text{cov}_i = \Delta \sigma_{\text{ref}}^{\text{B}} \cdot \Delta \sigma_i^{\text{B}} \cdot \text{cor}_i$  with the correlation factor  $\text{cor}_i = \sqrt{\min(\frac{N_i}{N_{\text{ref}}}, \frac{N_{\text{ref}}}{N_i})}$  due to a certain number of events being shared in both samples. Results are presented in Figure 5.16. The high statistics data set at 3.7730 GeV shows deviations of up to 5% for stricter cut values  $\chi_{\text{cut}}^2 < 30$ . For more loose cut values, deviations lie within the range of statistical fluctuations. However, data sets with lower statistics show a linear effect of the  $\chi^2$  cut on the cross section around the final value  $\chi_{\text{cut}}^2 = 30$ . At  $\chi_{\text{cut}}^2 \approx 50$  this linear increase changes into a continuous decrease. The former behavior is a purely systematic effect likely caused by small differences between data and MC simulations, which is accounted for by assigning a systematic uncertainty. The latter can be explained by limited statistics in the data. If the cut is loosened further, there are no more events in data above a certain value. In the huge MC sample on the other hand, there are events even at higher  $\chi^2$  values. As can be checked with Equation (5.1), an increase of the cut value therefore leads to a decrease of the Born cross section.

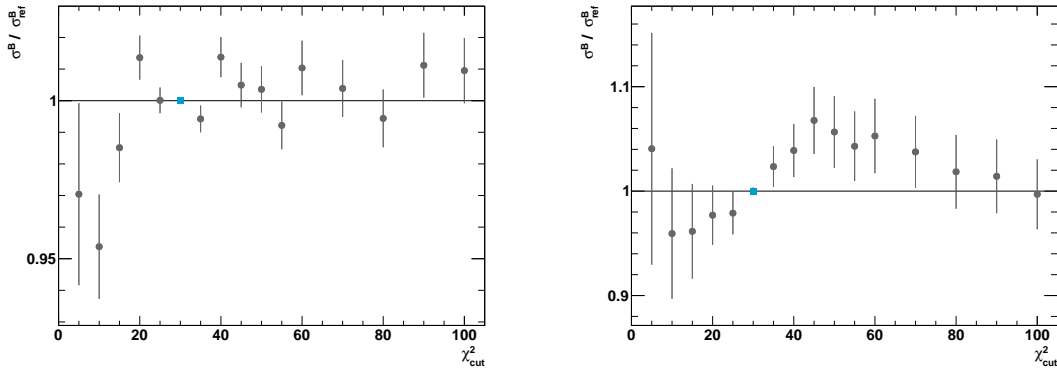


**Figure 5.16.:** Systematic study of the influence of the  $\chi^2$  cut on the final result  $\sigma_{\text{ref}}^{\text{B}}$  of the  $\eta \rightarrow \gamma\gamma$  decay mode for the high statistics data set at 3.7730 GeV (**left**) and one with lower statistics at 4.2438 GeV (**right**). The reference value is represented by a blue squared marker.



A systematic uncertainty is assigned (see Table 5.9) as the standard deviation  $\sigma_R$  of a weighted average of the cross section ratio  $R_{\sigma,i}$  given by

$$\sigma_R^2 = \frac{\sum_i \omega_i^2 (1 - R_{\sigma,i})^2}{\sum_i \omega_i^2} \quad \text{with} \quad \omega_i = (\Delta R_{\sigma,i})^{-1}, \quad (5.28)$$

which is evaluated in a symmetric region around the reference cut value

$$\chi_{\text{cut},i}^2 \in \{5, 10, \dots, 55\}.$$

This is a very conservative treatment of systematic uncertainties, since the values are strongly correlated with statistical fluctuations.

### 5.7.2. Signal Region

In Section 5.2 a signal region was defined to extract the number of observed events  $N_{\text{obs}}$  and efficiency  $\varepsilon$ , such that it contains  $\alpha_{\text{sr}} = 95\%$  of the signal. Changing this arbitrarily chosen value has an effect on the final result, which has to be taken into account (see Figure 5.17). A systematic uncertainty is assigned using Equation (5.28) and the resulting values can be found in Tables 5.9 to 5.11.

### 5.7.3. Radiative Corrections

The radiative correction factor  $(1 + \delta_r)$  was obtained from QED calculations with an iterative approach using the calculated Born cross sections as input as described in Section 5.5. After five iterations the correction is considered to be converged. In order to investigate a possible influence of this breaking criteria on the final result, the iterative procedure is continued as presented in Figure 5.18, showing a strong converging behavior. After the fifth and final iteration all fluctuations are compatible with zero within their relative statistical uncertainties and can therefore be neglected.

### 5.7.4. Background Description

The last source of a possible systematic effect that is considered in this work is the description of the remaining background. Background contributions in the invariant mass of the meson system are described by a first and a second order polynomial for the  $\eta \rightarrow \gamma\gamma$  and  $m \rightarrow \pi^+\pi^-\pi^0$  decay modes, respectively. A systematic uncertainty is assigned as the difference of the cross section value using a polynomial higher by one order as shown in Figure 5.19. Results can be found in Tables 5.9 to 5.11. There is only a marginal difference between these two fits, yielding a relative difference of the Born cross section values on the permille level.

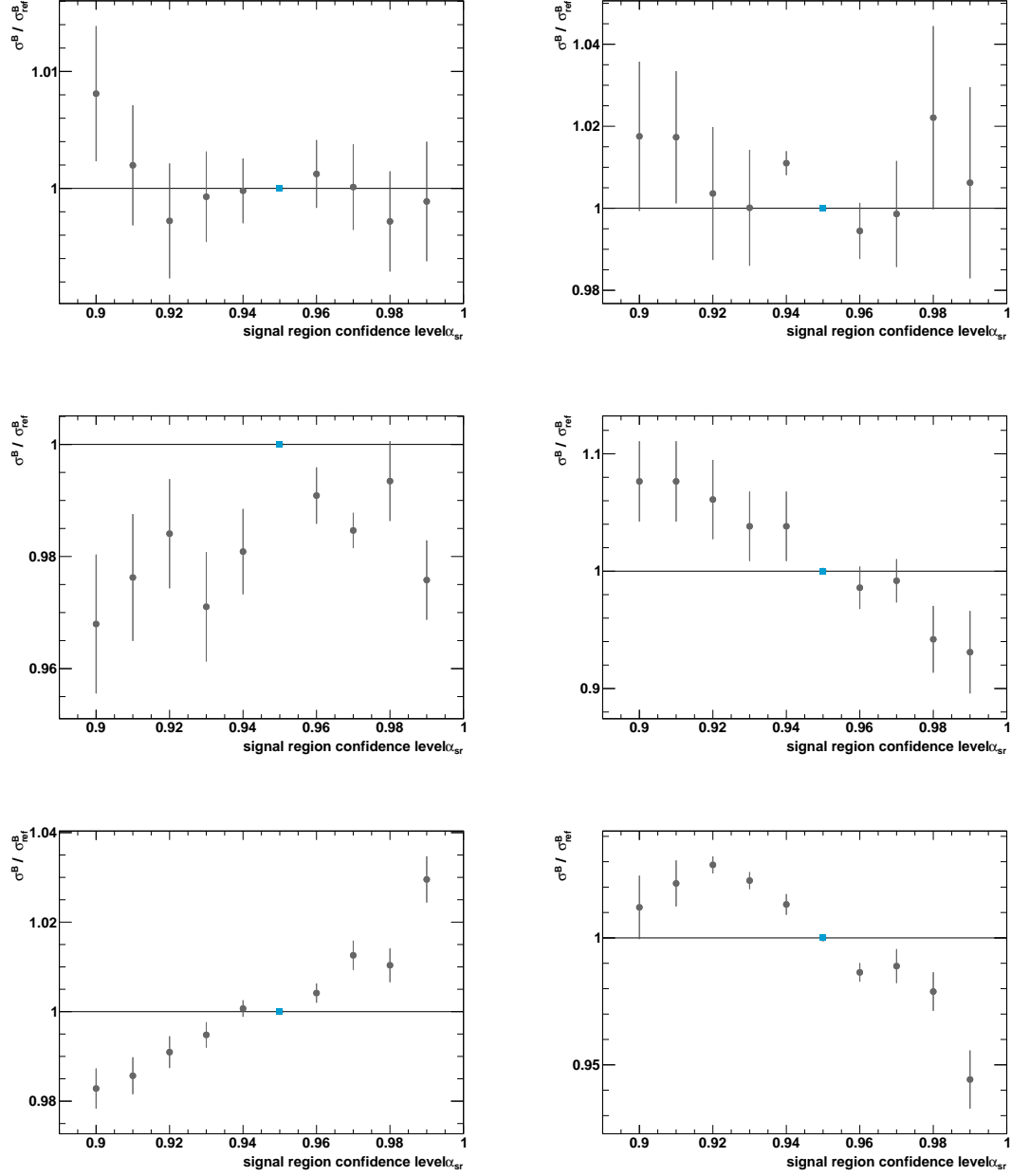


**Figure 5.17.:** Systematic study of the arbitrarily chosen signal region confidence level  $\alpha_{\text{sr}}$  of the  $\eta \rightarrow \gamma\gamma$  (**top**),  $\eta \rightarrow \pi^+\pi^-\pi^0$  (**middle**) and  $\omega \rightarrow \pi^+\pi^-\pi^0$  (**bottom**) decay modes for the high statistics data set at 3.7730 GeV (**left**) and one with lower statistics at 4.2438 GeV (**right**). The reference value is represented by a blue squared marker.

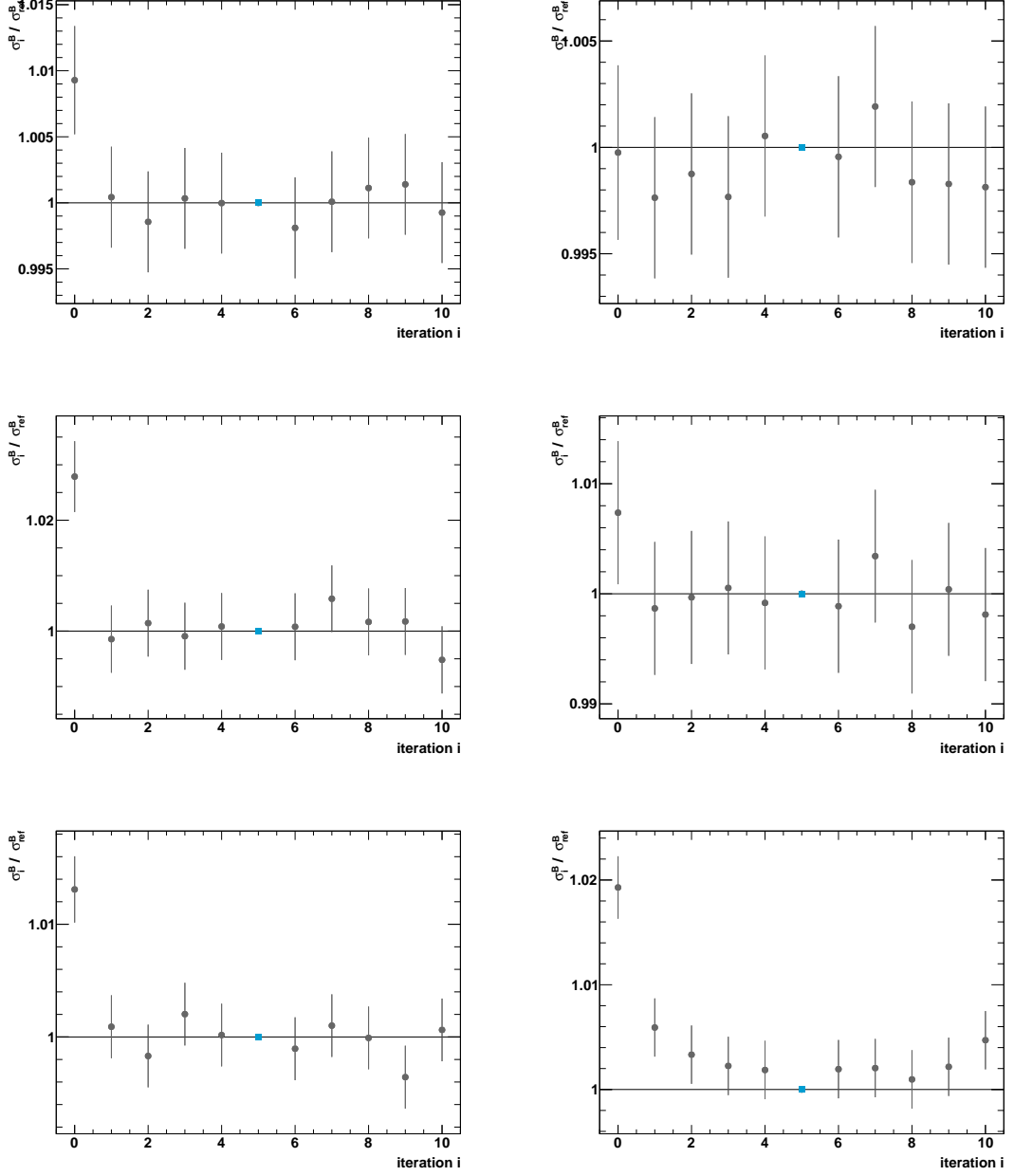


**Figure 5.18.:** Systematic study of the radiative correction procedure for the  $\eta \rightarrow \gamma\gamma$  (**top**),  $\eta \rightarrow \pi^+\pi^-\pi^0$  (**middle**) and  $\omega \rightarrow \pi^+\pi^-\pi^0$  (**bottom**) decay modes for the high statistics data set at 3.7730 GeV (**left**) and one with lower statistics at 4.2438 GeV (**right**). The reference value is represented by a blue squared marker.

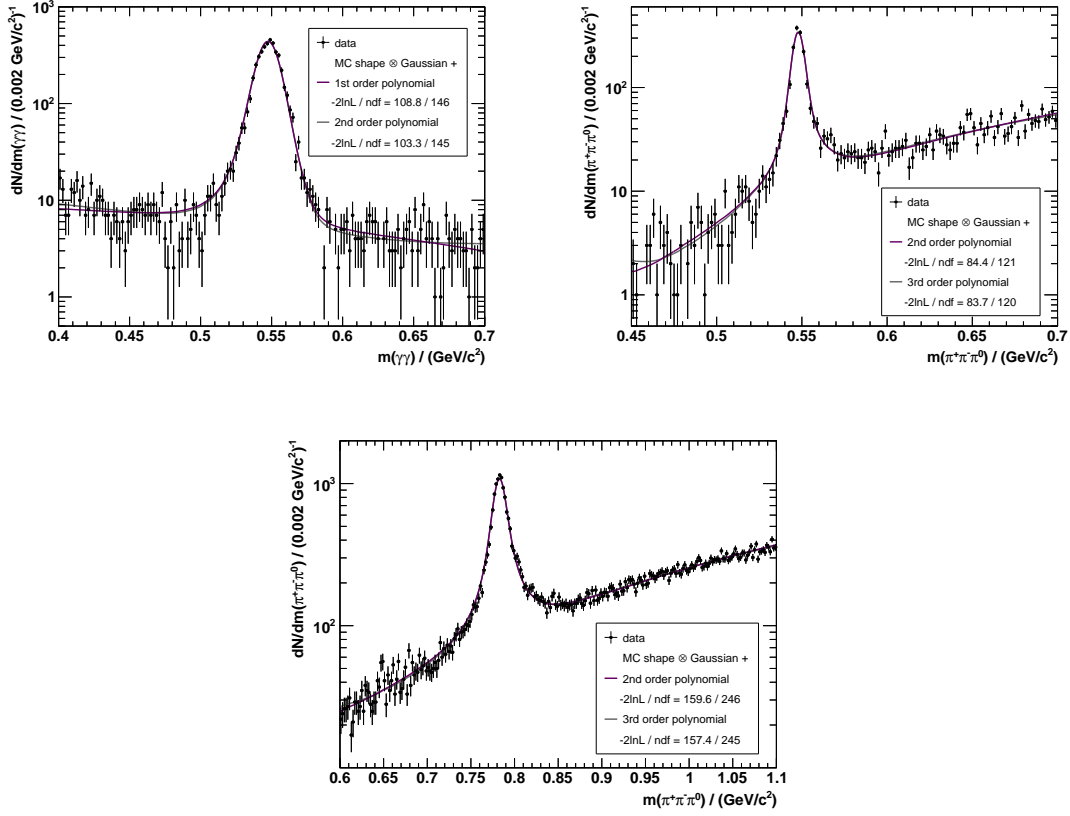


**Figure 5.19.:** Invariant mass distribution of the meson system:  $\eta \rightarrow \gamma\gamma$  (top left),  $\eta \rightarrow \pi^+\pi^-\pi^0$  (top right) and  $\omega \rightarrow \pi^+\pi^-\pi^0$  (bottom) summed up over all 17 data samples. The reference fit as described in Section 5.2 is shown (magenta line) as well as an additional fit (gray line), where the background is considered with a polynomial higher by one order.

**Table 5.9.:** Systematic uncertainties in % dependent on the center-of-mass energy  $\sqrt{s}$  in GeV for the  $\eta \rightarrow \gamma\gamma$  decay mode.

	3.7730	3.8695	4.0076	4.1784	4.1888	4.1989	4.2092	4.2187
$\chi^2$ cut	1.0	2.1	1.9	1.9	4.1	2.9	3.9	5.0
Signal region	0.2	1.0	1.7	0.6	2.0	1.1	1.4	2.1
Background	0.5	0.3	0.8	0.7	0.6	0.9	0.5	1.7
Total	1.1	2.3	2.6	2.1	4.6	3.2	4.1	5.7

4.2263	4.2357	4.2438	4.2580	4.2668	4.2777	4.3583	4.4156	4.5995
3.2	2.1	3.7	2.7	2.0	6.4	2.6	2.3	3.5
1.1	1.0	1.0	2.4	1.4	1.9	1.8	1.3	2.6
0.6	1.3	0.7	1.0	0.5	1.1	1.2	1.2	1.1
3.5	2.6	3.9	3.7	2.5	6.8	3.4	2.9	4.5

**Table 5.10.:** Systematic uncertainties in % dependent on the center-of-mass energy  $\sqrt{s}$  in GeV for the  $\eta \rightarrow \pi^+\pi^-\pi^0$  decay mode.

	3.7730	3.8695	4.0076	4.1784	4.1888	4.1989	4.2092	4.2187
Signal region	1.3	0.8	1.5	0.8	3.4	2.7	3.8	4.2
Background	2.4	1.8	1.7	1.5	1.5	0.6	1.6	1.5
Total	2.7	2.0	2.3	1.7	3.7	2.8	4.1	4.5

4.2263	4.2357	4.2438	4.2580	4.2668	4.2777	4.3583	4.4156	4.5995
1.9	4.9	4.4	3.0	2.4	3.0	4.3	2.7	2.9
1.5	1.6	1.6	2.1	1.6	1.4	2.3	1.6	1.6
2.4	5.2	4.7	3.7	2.9	3.3	4.9	3.1	3.3

**Table 5.11.:** Systematic uncertainties in % dependent on the center-of-mass energy  $\sqrt{s}$  in GeV for the  $\omega \rightarrow \pi^+\pi^-\pi^0$  decay mode.

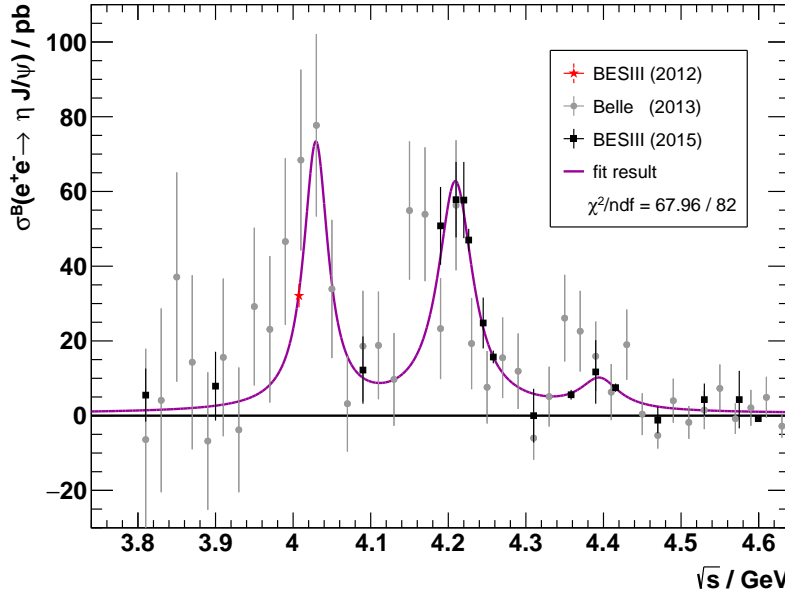
	3.7730	3.8695	4.0076	4.1784	4.1888	4.1989	4.2092	4.2187
Signal region	1.0	0.9	2.5	0.8	1.5	1.2	1.8	2.7
Background	0.3	0.3	0.3	0.3	0.3	0.2	0.2	0.3
Total	1.0	0.9	2.5	0.9	1.5	1.2	1.8	2.7

4.2263	4.2357	4.2438	4.2580	4.2668	4.2777	4.3583	4.4156	4.5995
1.5	2.5	2.2	1.5	1.9	2.2	1.9	2.1	2.1
0.2	0.2	0.3	0.3	0.2	0.2	0.2	0.2	0.2
1.5	2.5	2.2	1.5	1.9	2.2	1.9	2.1	2.1

## 5.8. Cross Check

The process  $e^+e^- \rightarrow \eta(J/\psi \rightarrow p\bar{p})$  provides a unique opportunity to perform a cross check of the analysis procedure developed in this work. Born cross sections  $\sigma^B(e^+e^- \rightarrow \eta J/\psi)$  have been published by the Belle collaboration [31] at center-of-mass energies from 5.3 GeV down to 3.8 GeV utilizing initial-state radiation, as well as by the BESIII collaboration [32, 33] at several center-of-mass energies between 3.8 GeV and 4.6 GeV, as shown in Figure 5.20. In both analyses, the  $J/\psi$  was reconstructed via its decay into a pair of leptons to make use of the higher branching fractions  $\mathcal{B}r(J/\psi \rightarrow e^+e^-) = 5.971(32)\%$  and  $\mathcal{B}r(J/\psi \rightarrow \mu^+\mu^-) = 5.961(33)\%$  compared to  $\mathcal{B}r(J/\psi \rightarrow p\bar{p}) = 0.2121(29)\%$  [36]. The partial wave analysis in Section 5.4 has shown that there is a significant contribution in five data samples. For these data sets, the Born cross sections are calculated with Equation (5.1). The number of observed events is extracted by integrating the invariant mass distribution of the  $p\bar{p}$  system only for the  $J/\psi$  contribution from the PWA solution. Reconstruction efficiencies are determined by a simple one-dimensional method using signal MC simulations evenly distributed in phase space.



**Figure 5.20.:** Born cross section  $\sigma^B(e^+e^- \rightarrow \eta J/\psi)$  as available in the literature. The red star is from [32], gray circles are from [31] and black squares are from [33]. The solid magenta line is a fit to the data further described in the text, which is used as input for MC simulations.

A least square fit is performed to the  $e^+e^- \rightarrow \eta J/\psi$  cross section of the available database as the sum of three incoherent Breit-Wigner distributions of the form

$$A = \frac{m\Gamma}{s^2 - m^2 + im\Gamma} , \quad (5.29)$$

with mass  $m$  and width  $\Gamma$  of a resonant contribution, as well as a second order polynomial. The three Breit-Wigner correspond to the  $\psi(4040)$ ,  $\psi(4160)$  and  $\psi(4360)$  resonances, as described in more detail in [31, 33]. All parameters are left free in the fit. In order to get a good estimate of the radiative correction factors, the MC simulations are generated according to the fit result. Results for the  $\eta \rightarrow \gamma\gamma$  decay mode are listed in Table 5.12.

For those data samples without a significant  $\eta J/\psi$  contribution an upper limit is calculated using a Bayesian approach [22, 121, 122]. First, an upper limit of the number of observed events is determined. A likelihood is defined based on Poisson statistics as

$$\mathcal{L}(\mu_{\text{sig}}; N_{\text{tot}}, N_{\text{bkg}}) = \int_0^\infty P(N_{\text{tot}}; \mu_{\text{sig}} + f \cdot \mu_{\text{bkg}}) P(N_{\text{bkg}}; \mu_{\text{bkg}}) d\mu_{\text{bkg}} , \quad (5.30)$$

where  $P(n; \mu) = \frac{1}{n!} \mu^n e^{-\mu}$  is the Poisson distribution,  $f$  is a scaling factor and  $\mu_{\text{sig}}$  and  $\mu_{\text{bkg}}$  are the expected number of signal and background events, respectively.  $N_{\text{tot}}$  is the number of events in a signal region around the  $J/\psi$  peak and  $N_{\text{bkg}}$  is the number of events in two corresponding sideband regions. The signal region is arbitrarily defined as an interval  $30 \text{ MeV}/c^2$  around the nominal mass of the  $J/\psi$  ( $m_{J/\psi} = 3.0969 \text{ GeV}/c^2$ ) [36]. Two sideband regions are defined with the same width of  $30 \text{ MeV}/c^2$  next to the signal region and leaving a gap of  $15 \text{ MeV}/c^2$ . The non- $\eta$  sideband subtracted invariant mass distribution of the  $p\bar{p}$  system is shown in Figure 5.21 for the  $\eta \rightarrow \gamma\gamma$  decay mode, summed up over all 17 data samples. The background under the peak follows a linear behavior, so the scaling factor is given by  $f = \frac{1}{2}$ . For a given confidence level  $CL$  one can find an upper limit  $N_{\text{UL}}$  which satisfies

$$CL = \frac{\int_{-\infty}^{N_{\text{UL}}} \mathcal{L}(\mu_{\text{sig}}; N_{\text{tot}}, N_{\text{bkg}}) d\mu_{\text{sig}}}{\int_{-\infty}^{+\infty} \mathcal{L}(\mu_{\text{sig}}; N_{\text{tot}}, N_{\text{bkg}}) d\mu_{\text{sig}}} . \quad (5.31)$$

Upper limits at 90 % confidence level are summarized in Table 5.13 as well as graphically depicted in Figure 5.22. All values agree with previous measurements. The upper limits at  $3.8695 \text{ GeV}$  and  $4.2777 \text{ GeV}$  center-of-mass energy are large due to the very limited statistics. The results of the five data samples with significant  $J/\psi$  contribution indicate a contribution of the  $\psi(4160)$  resonance, which was also seen by the Belle [31] and BESIII [33] collaborations. This means, that the analysis presented here is compatible with

previous analyses within statistical uncertainties, so that we can safely draw conclusions also for the full  $p\bar{p}\eta$  and  $p\bar{p}\omega$  reactions as discussed in the following section.

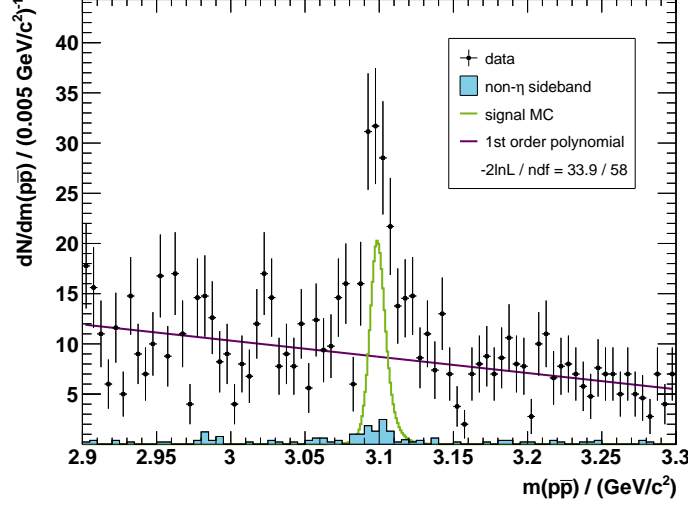


**Figure 5.21.:** Sideband corrected invariant mass distribution of the  $p\bar{p}$  system for the  $\eta \rightarrow \gamma\gamma$  decay, summed up over all 17 data samples. Black dots represent data and the non- $\eta$  sideband distribution is shown by the blue histogram. The green line is an arbitrarily scaled signal MC simulation, indicating the position and resolution of the reconstructed  $J/\psi \rightarrow p\bar{p}$  decay. The solid magenta line shows the result of a first order polynomial fit to the background shape, excluding the peak region from 3.05  $\text{GeV}/c^2$  to 3.15  $\text{GeV}/c^2$ .

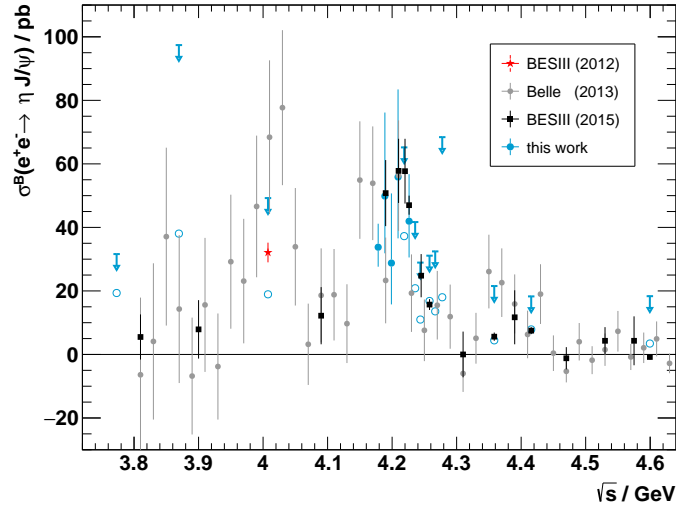


**Figure 5.22.:** Born cross sections  $\sigma^B(e^+e^- \rightarrow \eta J/\psi)$  and upper limits determined in this work compared to the database available in the literature. Blue dots represent the five data samples with significant  $J/\psi$  contribution, open circles are the expected cross section values for all other data sets and arrows indicate the corresponding upper limits. For more information on the literature values see caption in Figure 5.20.



**Table 5.12.:** Center-of-mass energies  $\sqrt{s}$ , integrated luminosities  $L$ , correction factors for initial-state radiation  $(1 + \delta_r)$  and vacuum polarization  $(1 + \delta_v)$  as well as number of observed events  $N_{\text{obs}}$ , efficiencies  $\varepsilon$  and the calculated Born cross sections  $\sigma^{\text{B}}(e^+e^- \rightarrow \eta J/\psi)$  for the  $\eta \rightarrow \gamma\gamma$  decay mode with their corresponding statistical uncertainties for the five data samples which revealed a significant  $J/\psi$  contribution in the PWA described in Section 5.4.

$\sqrt{s}$ / GeV	$L$ / pb $^{-1}$	$(1 + \delta_r)$	$(1 + \delta_v)$	$N_{\text{obs}}$	$\varepsilon$ / %	$\sigma^{\text{B}}$ / pb
4.1784	3189.0	0.8074	1.0543	$29.7^{+6.5}_{-5.4}$	$38.4 \pm 0.1$	$33.8^{+7.4}_{-6.1}$
4.1888	524.6	0.7779	1.0559	$7.2^{+3.8}_{-2.6}$	$39.7 \pm 0.1$	$49.9^{+26.3}_{-18.0}$
4.1989	526.0	0.7643	1.0567	$4.2^{+3.2}_{-1.9}$	$40.7 \pm 0.1$	$28.8^{+21.9}_{-13.0}$
4.2092	518.0	0.7737	1.0565	$8.1^{+4.0}_{-2.8}$	$40.6 \pm 0.1$	$55.9^{+27.6}_{-19.3}$
4.2263	1056.4	0.8542	1.0562	$13.6^{+4.8}_{-3.7}$	$40.6 \pm 0.1$	$42.0^{+14.8}_{-11.4}$

**Table 5.13.:** Center-of-mass energies  $\sqrt{s}$ , integrated luminosities  $L$ , correction factors for initial-state radiation  $(1 + \delta_r)$  and vacuum polarization  $(1 + \delta_v)$  for the twelve data samples which did not have a significant  $J/\psi$  contribution in the PWA described in Section 5.4. Additionally, the number of events in the signal region  $N_{\text{tot}}$  and the sideband regions  $N_{\text{bkg}}$ , efficiencies  $\varepsilon$ , and the calculated upper limits on the Born cross sections  $\sigma^{\text{B}}(e^+e^- \rightarrow \eta J/\psi)$  for the  $\eta \rightarrow \gamma\gamma$  decay mode.

$\sqrt{s}$ / GeV	$L$ / pb $^{-1}$	$(1 + \delta_r)$	$(1 + \delta_v)$	$N_{\text{tot}}$	$N_{\text{bkg}}$	$\varepsilon$ / %	$\sigma^{\text{B}}_{\text{UL}}$ / pb
3.7730	2931.8	0.8993	1.0570	46.8	91.9	$42.2 \pm 0.1$	31.6
3.8695	224.0	0.9290	1.0507	4.0	6.0	$40.0 \pm 0.1$	97.4
4.0076	482.0	0.9553	1.0438	4.6	7.2	$42.8 \pm 0.1$	49.2
4.2187	514.6	1.1701	1.0564	5.6	0.0	$40.5 \pm 0.1$	65.2
4.2357	530.3	1.0569	1.0554	4.0	3.0	$39.2 \pm 0.1$	41.7
4.2438	538.1	1.0464	1.0555	2.2	3.0	$37.4 \pm 0.1$	28.9
4.2580	828.4	1.0536	1.0534	5.6	0.0	$34.5 \pm 0.1$	31.1
4.2668	531.1	1.0238	1.0532	4.8	0.0	$31.4 \pm 0.1$	32.5
4.2777	175.7	1.0463	1.0530	1.0	3.0	$28.9 \pm 0.1$	68.4
4.3583	543.9	1.1749	1.0511	1.0	1.8	$25.5 \pm 0.1$	21.5
4.4156	1043.9	1.0714	1.0524	2.0	3.0	$30.6 \pm 0.1$	18.3
4.5995	586.9	1.1439	1.0547	0.6	0.0	$14.6 \pm 0.1$	18.4

## 5.9. Results

Now that the Born cross sections have been determined at 17 center-of-mass energies including statistical and systematic uncertainties, an investigation of possible resonant contributions in the  $p\bar{p}m$  cross section is performed. The final Born cross sections  $\sigma^B(e^+e^- \rightarrow p\bar{p}\eta)$  and  $\sigma^B(e^+e^- \rightarrow p\bar{p}\omega)$  are shown in Figure 5.23. The excellent high luminosity data samples from the BESIII experiment provide precise cross section values for both reactions with reasonable statistical and systematic uncertainties, allowing to further study possible contributions of  $\psi \rightarrow p\bar{p}m$  decays. No obvious resonant structures can be observed. As shown in Section 5.8, there should be at least a contribution of the  $\psi(4160)$  in the  $p\bar{p}\eta$  cross section with an intermediate  $J/\psi \rightarrow p\bar{p}$  decay. However, due to the small branching fraction of  $\mathcal{B}r(J/\psi \rightarrow p\bar{p}) = 0.2121(29)\%$ , the cross section for this process  $\sigma^B(e^+e^- \rightarrow \psi(4160) \rightarrow \eta(J/\psi \rightarrow p\bar{p}))$  is very low.

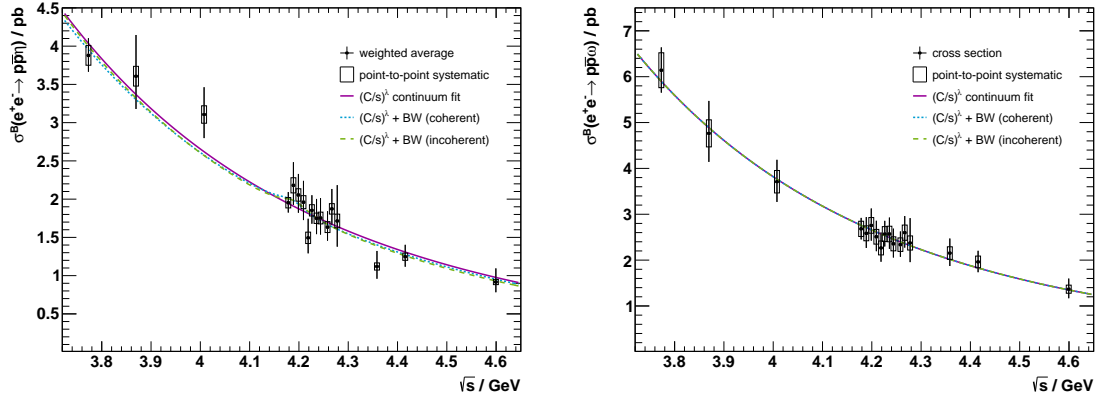


**Figure 5.23.:** Born cross sections for the  $p\bar{p}\eta$  (left) and  $p\bar{p}\omega$  (right) final states with their corresponding total uncertainties, including statistical and systematic uncertainties. Open squares indicate point-to-point systematic uncertainties. Three maximum likelihood fits are shown, as further described in the text: Continuum contribution only (solid line), as well as adding one Breit-Wigner resonance coherently (dotted line) or incoherently (dashed line).

The significance and the amplitude of such a resonant contribution will now be investigated by performing an unbinned maximum likelihood fit. Continuum production of the  $p\bar{p}\eta$  final state is considered by [87]

$$\sigma_{\text{con}} = \left( \frac{C}{\sqrt{s}} \right)^\lambda, \quad (5.32)$$

where  $\sqrt{s}$  is the center-of-mass energy, and  $C$  and  $\lambda$  are *a priori* unknown parameters. A potential resonance is described by a Breit-Wigner amplitude as given in Equation (5.29) with mass  $m$  and width  $\Gamma$  being fixed to the  $\psi(4160)$  average values of the PDG, i.e.,

$m_{\psi(4160)} = 4191(5) \text{ MeV}/c^2$  and  $\Gamma_{\psi(4160)} = 70(10) \text{ MeV}/c^2$ . This additional contribution is added in a coherent

$$\sigma_{\text{coh}} = \left| \sqrt{\sigma_{\text{con}}} + \sqrt{\sigma_{\psi}} \frac{m\Gamma}{s^2 - m^2 + im\Gamma} e^{i\phi} \right|^2, \quad (5.33)$$

or incoherent way

$$\sigma_{\text{incoh}} = \sigma_{\text{con}} + \sigma_{\psi} \left| \frac{m\Gamma}{s^2 - m^2 + im\Gamma} \right|^2, \quad (5.34)$$

where  $\phi$  is the relative phase between continuum and resonant contribution with associated amplitudes  $\sigma_{\text{con}}$  and  $\sigma_{\psi}$ . Given the data  $x$  and a set of model parameters  $\Theta$ , the likelihood  $\mathcal{L}(x; \Theta)$  can be defined. Since data  $x$  are fixed, the likelihood is only a function of the parameters  $\Theta$  and can be written as

$$\mathcal{L}(\Theta) = \prod_{i,j} \mathcal{L}_{ij}(\Theta), \quad (5.35)$$

where  $\mathcal{L}_{ij}$  is a set of likelihood functions, one for each data set  $i$  and decay mode  $j$ . For the sake of clarity, these indices are omitted in the following formulas. The likelihood functions can be transformed to depend only on one parameter, i.e., the expected number of signal events to be observed  $N \equiv N_{ij}(\Theta)$ , which can be calculated using Equation (5.1)

$$N(\Theta) = \sigma(x; \Theta) \cdot L \cdot (1 + \delta_r)(1 + \delta_v) \cdot \varepsilon \cdot \mathcal{B}r, \quad (5.36)$$

where  $\sigma(x; \Theta)$  is the cross section hypothesis currently being tested. The functions  $\mathcal{L}_{ij}(N)$  are obtained from data via a likelihood scan of the number of signal events in the invariant mass distributions of the meson systems. Binned maximum likelihood fits are performed based on Poisson statistics, as described in Section 5.2, for a series of fixed  $N$  around the observed value  $N_{\text{obs}}$ . Results are shown in Figure 5.24. These likelihood scans are successfully described by asymmetric Gaussian distributions of the type

$$\mathcal{G}(N) = \frac{1}{\sqrt{2\pi}(\frac{\sigma_L + \sigma_R}{2})} e^{-\frac{(N-\mu)^2}{2\sigma_k^2}} \quad \text{with} \quad \sigma_k = \begin{cases} \sigma_L, & N \leq \mu \\ \sigma_R, & N > \mu \end{cases}, \quad (5.37)$$

with mean  $\mu$ , i.e., the number of signal events with the highest maximum likelihood value, and parameters  $\sigma_L$ ,  $\sigma_R$  incorporating Gaussian distributed asymmetric statistical uncertainties. Fit parameters can be found in Table 5.14. As expected, the mean matches the previously determined number of observed events. A noteworthy deviation from the asymmetric Gaussian shape is only visible for the smallest data sample, but can

generally be neglected. The likelihood functions, including systematic uncertainties  $\sigma_{\text{sys}}$ , can therefore be written in the form

$$\mathcal{L}(N) = \frac{1}{\sqrt{2\pi}\left(\frac{\sigma_L + \sigma_R}{2}\right)} e^{-\frac{(N-\mu)^2}{2(\sigma_k^2 + \sigma_{\text{sys}}^2)}} \quad \text{with} \quad \sigma_k = \begin{cases} \sigma_L, & N \leq \mu \\ \sigma_R, & N > \mu \end{cases}. \quad (5.38)$$

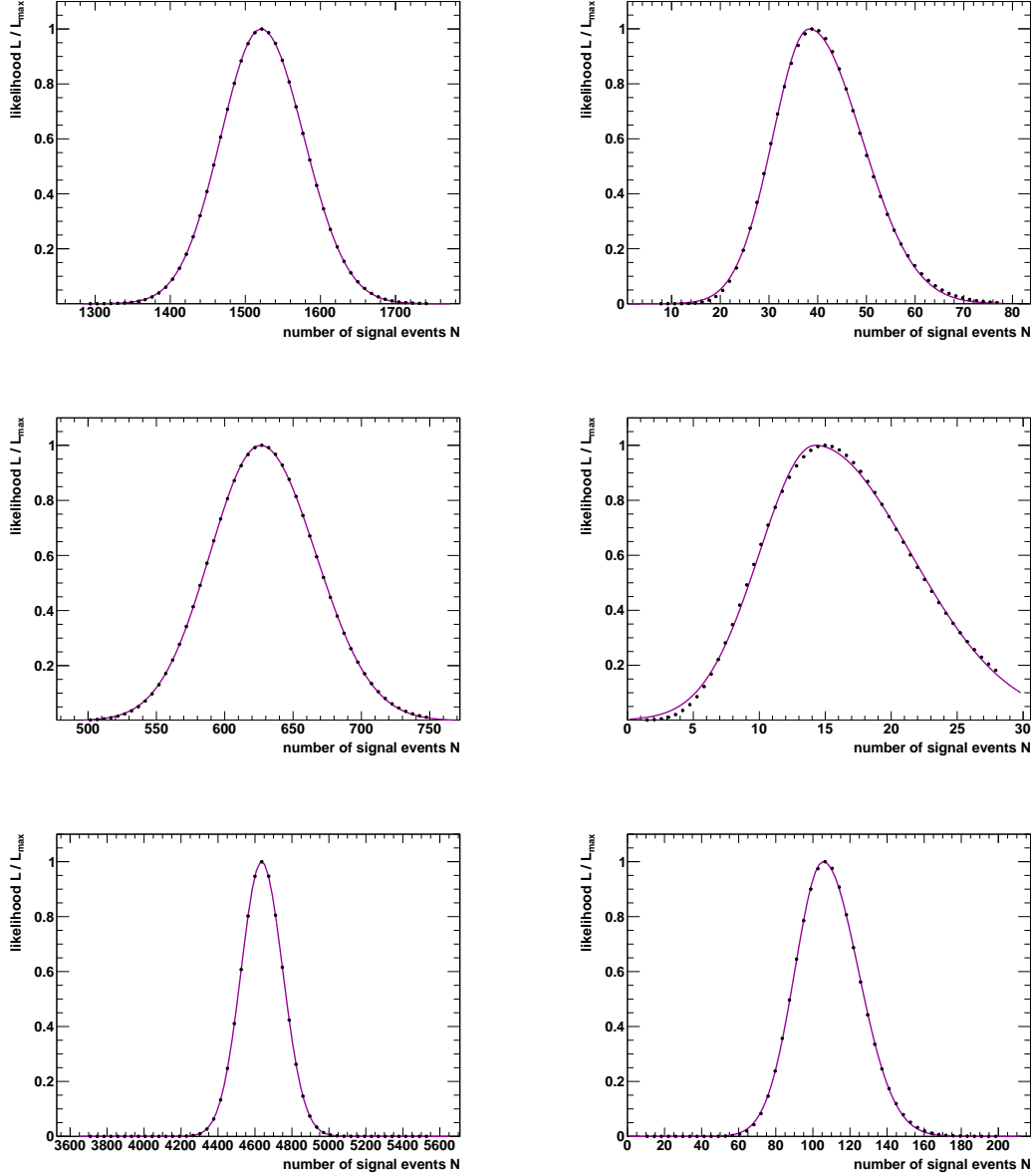


**Figure 5.24.:** Likelihood scans of the number of signal events in the invariant mass distributions of the meson system for the  $\eta \rightarrow \gamma\gamma$  (**top**),  $\eta \rightarrow \pi^+\pi^-\pi^0$  (**middle**) and  $\omega \rightarrow \pi^+\pi^-\pi^0$  (**bottom**) decay modes for the high statistics data set at 3.7730 GeV (**left**) and the one with the smallest statistics at 4.2777 GeV (**right**). The asymmetric Gaussian fit results are shown by solid lines.

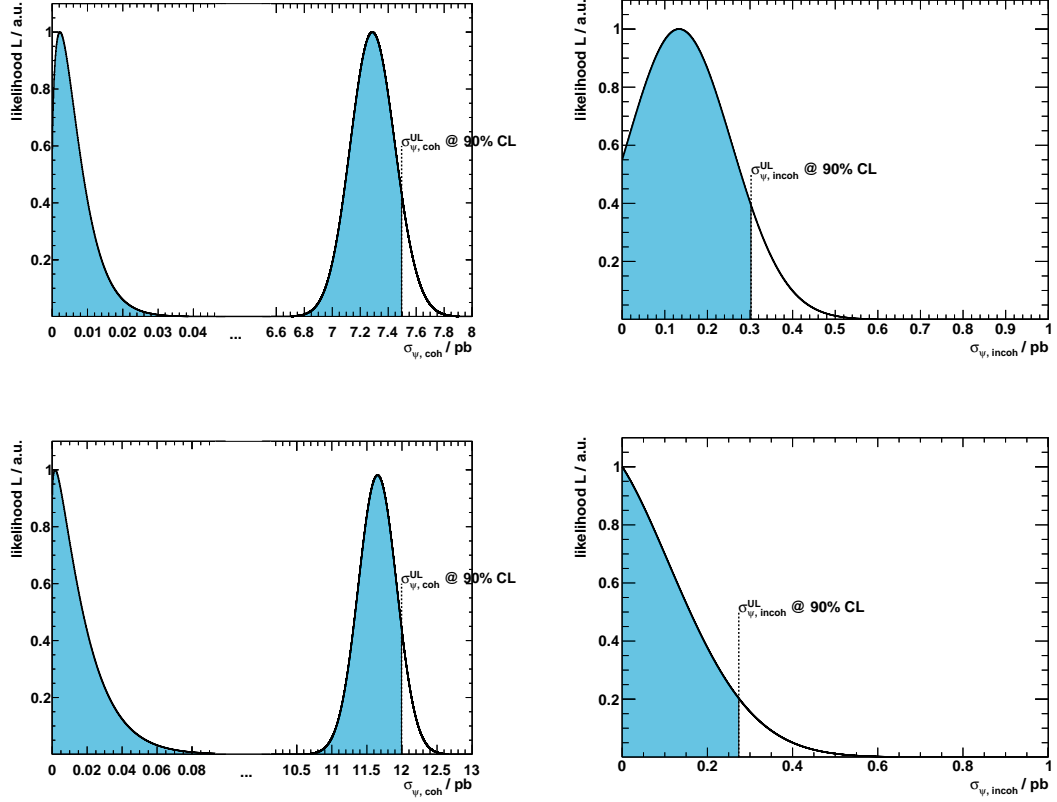


**Figure 5.25.:** Likelihood distribution for a coherent (**left**) and incoherent (**right**)  $\psi(4160)$  resonant contribution in the  $p\bar{p}\eta$  (**top**) and  $p\bar{p}\omega$  (**bottom**) cross section. Upper limits are calculated at 90 % confidence level indicated by dashed lines. Note the special formatting of the x-axis.

Now unbinned maximum likelihood fits are performed according to Equations (5.32) to (5.34) as graphically depicted in Figure 5.23. The likelihood distributions are shown in Figure 5.25. In the coherent case, the fits show two solutions with exactly the same fit quality, i.e., the same maximum likelihood values. One where the interference effect between the continuum and the Breit-Wigner amplitude is constructive and the other one where this is destructive, corresponding to a smaller and a larger resonant amplitude, respectively. This multiple-solution problem is discussed in more detail in [123]. It states that when fitting experimental data with the coherent sum of a Breit-Wigner amplitude and another function  $f$  with a specific form, there can be two and only two non-trivial solutions. This is the case for the continuum distribution defined in Equation (5.32).

The incoherent fit only shows one solution, which, for the  $p\bar{p}\omega$  final state has a vanishing resonant amplitude, and for the  $p\bar{p}\eta$  final state the amplitude has a value of  $0.13(12)$  pb. The latter can be compared to the result of the fit to the  $e^+e^- \rightarrow \eta J/\psi$  cross section as described in Section 5.8. The fit to the literature data yields an amplitude of  $61.2(59)$  pb,

which has to be multiplied by the branching fraction of the additional  $J/\psi \rightarrow p\bar{p}$  decay  $\mathcal{B}r(J/\psi \rightarrow p\bar{p}) = 0.2121(29)\%$  [36]. The resulting value is  $0.13(1)$  pb, which exactly matches the one determined by the fit to the  $p\bar{p}\eta$  cross section. However, the fit uncertainty in this work is quite large and the significance for such a signal is  $1.1\sigma$ .

**Table 5.14.:** Asymmetric Gaussian parameters  $\mu$ ,  $\sigma_L$  and  $\sigma_R$  of fits to the likelihood scans for two  $\eta$  meson decay modes.

$\sqrt{s}$ / GeV	$\eta \rightarrow \gamma\gamma$			$\eta \rightarrow \pi^+\pi^-\pi^0$			$\omega \rightarrow \pi^+\pi^-\pi^0$		
	$\mu$	$\sigma_L^2$	$\sigma_R^2$	$\mu$	$\sigma_L^2$	$\sigma_R^2$	$\mu$	$\sigma_L^2$	$\sigma_R^2$
3.7730	1521.1	53.8	57.0	626.2	37.0	40.4	4635.8	110.4	114.0
3.8695	105.9	13.1	16.3	39.1	8.1	11.3	284.8	25.6	29.1
4.0076	190.8	18.2	21.3	78.0	11.6	14.9	496.9	33.8	37.3
4.1784	828.6	39.5	42.7	281.9	23.0	26.2	2356.6	74.3	77.7
4.1888	144.1	15.6	18.9	57.3	10.1	13.5	369.4	29.3	32.7
4.1989	133.1	15.1	18.4	62.0	9.7	12.8	379.4	28.8	32.2
4.2092	135.4	15.0	18.2	46.6	8.5	11.5	354.8	27.6	30.9
4.2187	106.3	13.7	16.9	37.6	7.7	10.7	318.0	26.3	29.6
4.2263	254.3	21.1	24.3	96.1	12.9	16.1	732.8	41.4	44.8
4.2357	120.4	14.5	17.7	46.5	8.4	11.4	368.0	28.4	31.8
4.2438	119.4	14.0	17.2	45.9	8.5	11.6	352.6	27.9	31.2
4.2580	188.2	18.1	21.3	60.3	9.8	12.9	538.2	34.9	38.3
4.2668	132.5	14.8	18.0	41.3	8.0	11.2	346.1	27.6	31.0
4.2777	38.3	7.5	10.8	14.2	4.2	7.3	105.6	15.3	18.9
4.3583	79.9	11.3	14.5	25.9	6.0	9.0	299.4	25.4	28.7
4.4156	175.3	17.6	20.8	56.8	9.8	13.2	539.2	34.4	37.7
4.5995	79.3	11.2	14.4	14.7	4.3	7.4	209.5	20.7	24.0

### 5.9.1. Upper Limit Determination

As shown in the previous section, no obvious resonant structure can be observed in the  $p\bar{p}\eta$  and  $p\bar{p}\omega$  cross sections and thus upper limits are calculated, again using a Bayesian approach. In general, the vector  $\Theta$  can be split into two components  $\Theta = (\xi, \Phi)$ , where  $\xi$  is referred to as the parameter of interest, in this case the amplitude  $\sigma_\psi$  of a possible resonant contribution, and  $\Phi$  containing all remaining fit parameters. For a given confidence level  $CL$  one can find an upper limit  $\xi^{\text{UL}}$  which satisfies

$$CL = \frac{\int_{-\infty}^{\xi^{\text{UL}}} \mathcal{L}(\Theta) \pi(\Theta) d\xi}{\int_{-\infty}^{+\infty} \mathcal{L}(\Theta) \pi(\Theta) d\xi}, \quad (5.39)$$

where  $\pi(\Theta)$  is some probability distribution used to incorporate prior knowledge on the model parameters, e.g., to exclude unphysical negative cross section values

$$\pi(\Theta) = \begin{cases} 1, & \xi \geq 0 \\ 0, & \xi < 0 \end{cases}. \quad (5.40)$$

Although this function is not normalized, it does not cause a problem because the likelihood runs quickly towards zero. Since decays of resonances to  $p\bar{p}\eta$  and  $p\bar{p}\omega$  in this energy regime have still not been observed, an upper limit scan is performed, for mass  $m$  and width  $\Gamma$  of a possible resonant contribution fixed to values in steps of  $1 \text{ MeV}/c^2$  in the ranges  $4 \text{ GeV}/c^2 < m < 4.4 \text{ GeV}/c^2$  and  $40 \text{ MeV} < \Gamma < 300 \text{ MeV}$ , respectively. Results are shown in Figure 5.26. The upper limit of a coherent contribution is higher than the incoherent one by about a factor of 10, which is caused by the solution where the interference effect between the continuum and the Breit-Wigner amplitude is destructive. There are also areas where the upper limit gets worse due to the lack of data. Adding new data sets to this analysis could seal these holes. As mentioned in Section 4.1, BESIII has initiated a systematic scan to precisely study the line shape of exotic candidates. Since the final calibration of the most recently taken data samples is still in progress, only a glimpse at these data is given in an outlook in Chapter 7.

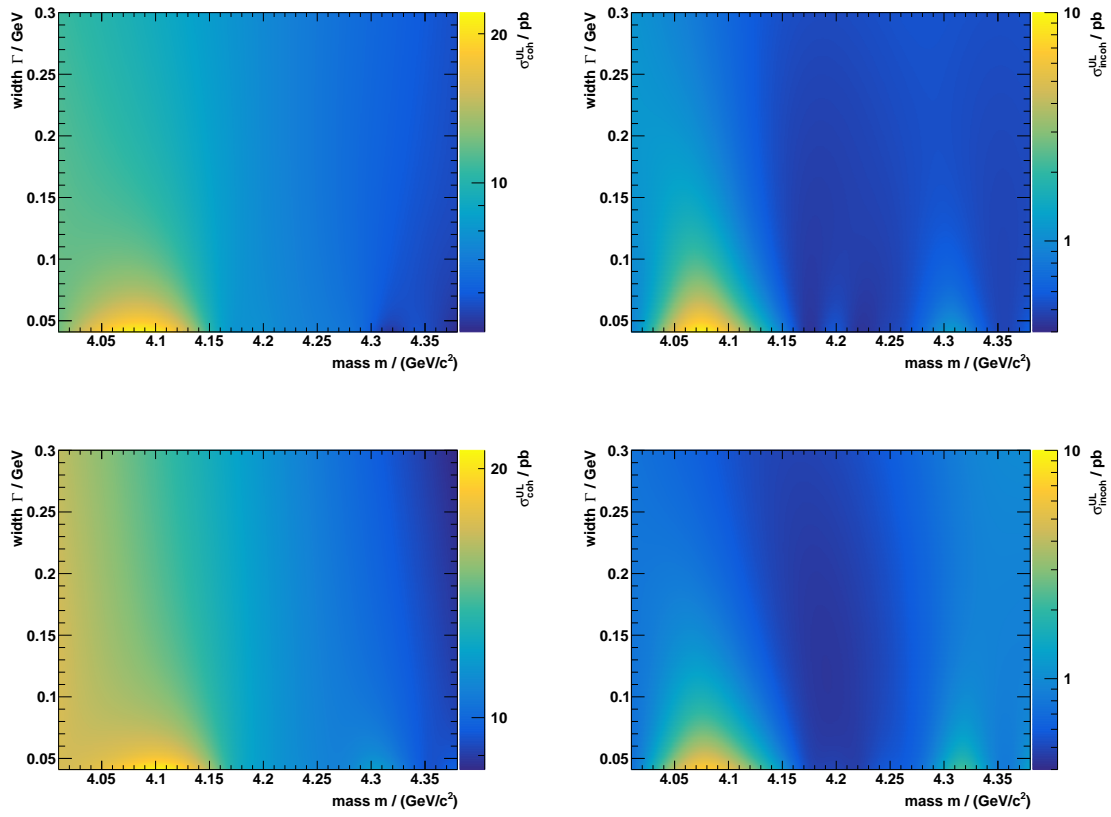


**Figure 5.26.:** Upper limits for a possible coherent (**left**) and incoherent (**right**) resonant contribution with mass  $m$  and width  $\Gamma$  in the  $p\bar{p}\eta$  (**top**) and  $p\bar{p}\omega$  (**bottom**) cross sections.



## 6. Analysis of $e^+e^- \rightarrow p\bar{p}\eta'$ and $e^+e^- \rightarrow p\bar{p}f_1$

In the following, an analysis of the data is presented regarding the cross sections of  $e^+e^- \rightarrow p\bar{p}\eta'$  and  $e^+e^- \rightarrow p\bar{p}f_1$ . The mesons are named according to their quantum numbers, here  $\eta'$  ( $J^{PC} = 0^{-+}$ ) and  $f_1$  ( $1^{++}$ ). In this notation, different excitations are often indicated by adding the mass of the state to its name in parentheses, e.g.,  $f_1(1285)$ . Since this is the lightest  $0^+(1^{++})$  meson, it is simply referred to as  $f_1$  throughout this thesis. The  $p\bar{p}$  pair is again directly detected with the BESIII detection system, whereas the mesons are reconstructed from their decay products. The three most dominant branching fractions of the two mesons given by the PDG are listed in Table 6.1. The  $\eta'$  has a dominant decay mode into  $\eta\pi^+\pi^-$ , whose signature is very similar to that of  $\eta \rightarrow \pi^+\pi^-\pi^0$ , and the subsequent  $\eta$  meson is again reconstructed only via its electromagnetic decay into two photons. The decay  $\eta' \rightarrow \gamma\rho^0$  has a branching fraction of about 28.9 %, including non-resonant  $\gamma\pi^+\pi^-$  contributions. Due to the single photon, the background increases drastically and this channel is not included in the upcoming analysis. The third highest decay mode is  $\eta' \rightarrow \eta\pi^0\pi^0$ , which is similar to the  $\eta \rightarrow \pi^0\pi^0\pi^0$  decay. A broad signal shape is expected with six photons in the final state, making the reconstruction quite difficult. Therefore, this channel is excluded from this analysis. The  $f_1$  also has a dominant decay into  $\eta\pi^+\pi^-$ . The channels with the next highest branching fractions are decays into four pions, which are not included in this work. Thus, both mesons, i.e.,  $\eta'$  and  $f_1$ , are reconstructed by their decay to  $\eta\pi^+\pi^-$ .

**Table 6.1.:** Branching fractions  $\mathcal{Br}$  for different decay modes of the  $\eta'$  (**left**) and the  $f_1$  meson (**right**). Values are taken from [36].

mode $i$	$\mathcal{Br} \ (\Gamma_i/\Gamma)$	mode $i$	$\mathcal{Br} \ (\Gamma_i/\Gamma)$
$\eta' \rightarrow \eta\pi^+\pi^-$	$(42.6 \pm 0.7) \%$	$f_1 \rightarrow \eta\pi^+\pi^-$	$(35 \pm 15) \%$
$\rightarrow \gamma\rho^0$	$(28.9 \pm 0.5) \%$	$\rightarrow \pi^+\pi^-\pi^0\pi^0$	$(22.3^{+1.3}_{-1.2}) \%$
$\rightarrow \eta\pi^0\pi^0$	$(22.8 \pm 0.8) \%$	$\rightarrow \pi^+\pi^-\pi^+\pi^-$	$(11.2^{+0.7}_{-0.6}) \%$

After the initial event selection, as described in Chapter 4, particles are constrained by a 5C kinematic fit. Four constraints are used to specify energy and momentum conservation and one additional constraint is set for the reconstruction of the subsequent  $\eta \rightarrow \gamma\gamma$  decay (see Section 4.3). The combination yielding the smallest  $\chi^2_{5C}$  value is kept for further analysis. Two mass windows are selected to reduce background unrelated to an  $\eta'$  or  $f_1$  event, given by

$$\eta' : 0.850 \text{ GeV}/c^2 \leq m(\eta\pi^+\pi^-) \leq 1.100 \text{ GeV}/c^2 , \quad (6.1)$$

$$f_1 : 1.100 \text{ GeV}/c^2 \leq m(\eta\pi^+\pi^-) \leq 1.600 \text{ GeV}/c^2 . \quad (6.2)$$

Resulting invariant mass distributions show clear peaks at the nominal positions of the  $\eta'$  mass ( $m_{\eta'} = 957.78(6) \text{ MeV}/c^2$ ) and the  $f_1$  mass ( $m_{f_1} = 1281.9(5) \text{ MeV}/c^2$ ) [36], as depicted in Figure 6.1. There could also be a small contribution of  $\eta(1295)$ , which has been reported by various experiments with a mass of  $m_{\eta(1295)} = 1294(4) \text{ MeV}/c^2$  [36]. It is considered to be the first radial excitation of the  $\eta$  meson. However, the mass of the  $\eta(1295)$  does not match the maximum of the peak as good as the mass of the  $f_1(1285)$ . This is indicated in Figure 6.1 by two vertical lines at the respective mass values. Additionally, the  $\eta(1295)$  is significantly broader ( $\Gamma_{\eta(1295)} = 55(5) \text{ MeV}/c^2$ ) than the  $f_1$  ( $\Gamma_{f_1} = 22.7(11) \text{ MeV}/c^2$ ), which describes the data quite well. The structure seen in this work is therefore treated as a pure  $f_1$  contribution.

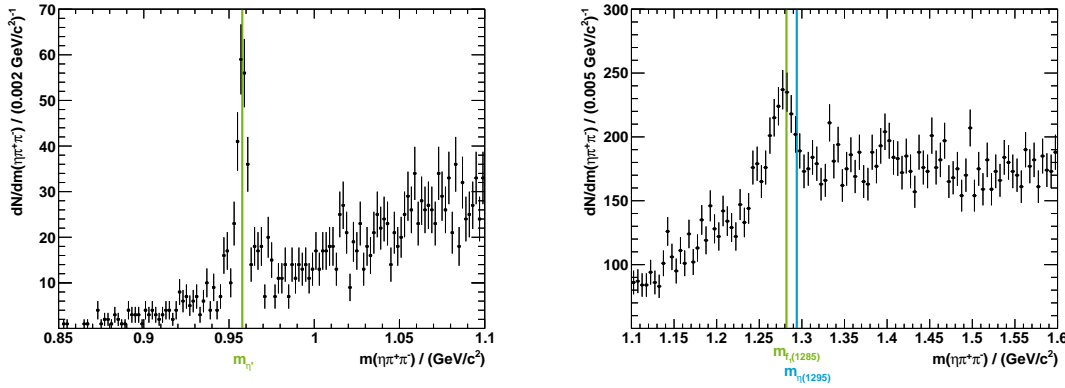


**Figure 6.1.:** Invariant mass distributions of the  $\eta\pi^+\pi^-$  system in the vicinity of the  $\eta'$  (left) and the  $f_1$  (right) meson. Black dots represent the data summed up over all 17 data sets, and vertical lines indicate the nominal values of the  $\eta'$ ,  $f_1$  and  $\eta(1295)$  mass.

## 6.1. Background Studies

Possible background contributions are studied once more using the generic MC sample provided by BESIII. The huge generic sample is scaled down to fit the data at 4.1784 GeV, using one scale parameter for signal and one for the sum of all background contributions. The invariant mass distributions of the  $\eta\pi^+\pi^-$  systems are presented in Figure 6.2, showing a reasonable agreement between data and MC within statistical uncertainties. In particular, there is no peaking background, neither under the  $\eta'$  peak nor the  $f_1$  peak. Dominant contributions are listed in Table 6.2. The background spectra contain processes which do not correspond to the signal hypothesis ( $p\bar{p}\eta\pi^+\pi^-$ ). A cut to the  $\chi^2$  value of the 5C kinematic fit is therefore able to increase the significance of the signal. The optimal position for such a cut is determined with a figure of merit, as defined in Equation (5.4).  $\chi^2$  distributions are depicted in Figure 6.3.

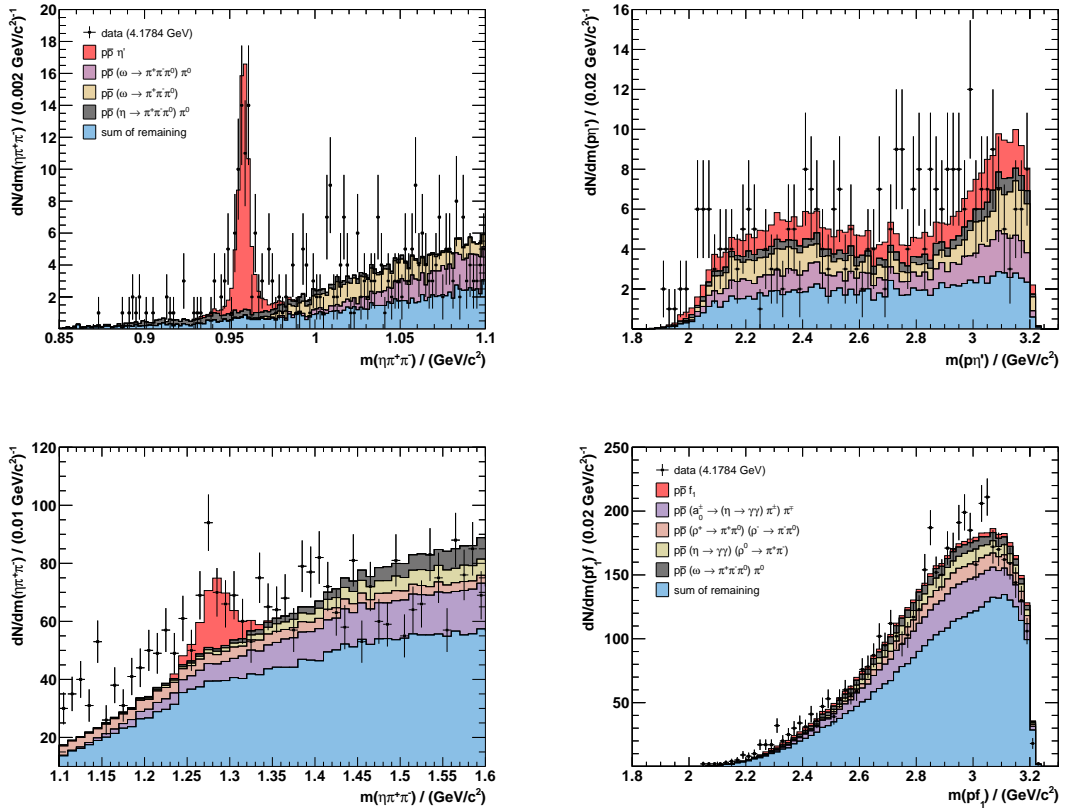


**Figure 6.2.:** Invariant mass distributions of the  $\eta\pi^+\pi^-$  (left) and the  $p\pi$  system (right) for  $p\bar{p}\eta'$  (top) and  $p\bar{p}f_1$  (bottom). Black dots represent the data at 4.1784 GeV compared to differently colored, stacked contributions from the generic MC sample: The signal (red), the most dominant background contributions, as well as the sum of all remaining background processes (blue). Spectra on each row share the same legend.

## 6. Analysis of $e^+e^- \rightarrow p\bar{p}\eta'$ and $e^+e^- \rightarrow p\bar{p}f_1$

The figure of merit is calculated with the information of the generic MC sample scaled to data, showing maxima at  $\chi^2$  values of 82 ( $\eta'$ ) and 106 ( $f_1$ ). An additional cross check is performed using the data driven sideband approach introduced in Chapter 5. Background contributions in the  $\eta\pi^+\pi^-$  invariant mass distributions of the  $p\bar{p}\eta'$  and  $p\bar{p}f_1$  final states are described by a second and third order polynomial, respectively. The corresponding  $\chi^2$  distributions agree with the result of the generic MC sample within statistical uncertainties.

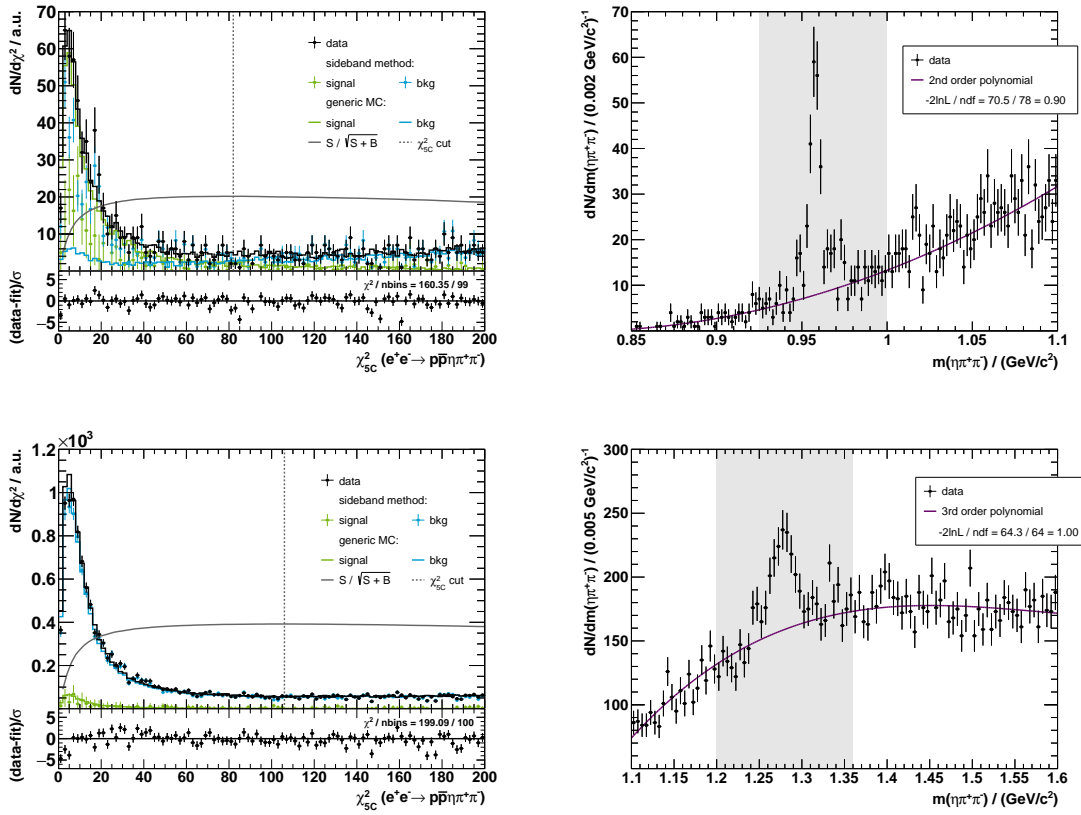


**Figure 6.3.:** **Left:**  $\chi^2$  distributions of the 5C kinematic fit to the  $p\bar{p}\eta\pi^+\pi^-$  final state for  $p\bar{p}\eta'$  (**top**) and  $p\bar{p}f_1$  (**bottom**). Black dots represent the data, summed up over all 17 high luminosity data sets. Signal (green) and background (blue) contributions are obtained from the generic MC sample (solid lines) or determined by a sideband approach (dotted). The dashed lines indicate cuts on the  $\chi^2$  values and the figures of merit (gray solid lines) are arbitrarily scaled for better visibility. **Right:** Corresponding invariant mass distributions and the fits to the background distributions, as described in the text. Gray shaded areas are excluded from the fits.

**Table 6.2.:** Topology of events from the generic MC sample at 4.1784 GeV, which survived all selection criteria in the reconstruction of the  $p\bar{p}\eta'$  (**top**) and  $p\bar{p}f_1$  (**bottom**) final states. The signal process is highlighted in green above the most dominant background channels that are ordered by occurrence, where  $N$  is the scaled number of events.

Process	Final state	$N$
$p\bar{p}(\eta' \rightarrow \eta\pi^+\pi^-)$	$p\bar{p}\eta\pi^+\pi^-$	68
$p\bar{p}(\omega \rightarrow \pi^+\pi^-\pi^0)\pi^0$	$p\bar{p}\pi^+\pi^-\pi^0\pi^0$	60
$p\bar{p}(\omega \rightarrow \pi^+\pi^-\pi^0)$	$p\bar{p}\pi^+\pi^-\pi^0$	60
$p\bar{p}(\eta \rightarrow \pi^+\pi^-\pi^0)\pi^0$	$p\bar{p}\pi^+\pi^-\pi^0\pi^0$	26
sum of remaining		114
$p\bar{p}(f_1 \rightarrow \eta\pi^+\pi^-)$	$p\bar{p}\eta\pi^+\pi^-$	106
$p\bar{p}(a_0^\pm \rightarrow \eta\pi^\pm)\pi^\mp$	$p\bar{p}\pi^+\pi^-\pi^0\pi^0$	694
$p\bar{p}(\rho^+ \rightarrow \pi^+\pi^0)(\rho^- \rightarrow \pi^-\pi^0)$	$p\bar{p}\pi^+\pi^-\pi^0\pi^0$	294
$p\bar{p}\eta(\rho^0 \rightarrow \pi^+\pi^-)$	$p\bar{p}\eta\pi^+\pi^-$	245
$p\bar{p}(\omega \rightarrow \pi^+\pi^-\pi^0)\pi^0$	$p\bar{p}\pi^+\pi^-\pi^0\pi^0$	217
sum of remaining		1857

## 6.2. Number of Observed Events

After applying the cuts to the  $\chi^2$  values of the 5C kinematic fits, the resulting invariant mass distributions of the  $\eta\pi^+\pi^-$  system are shown in Figure 6.4 summed up over all 17 data samples. Both spectra show a significant peak at the nominal position of the respective meson. However, the statistics of individual data sets are quite limited and the peaks may not be as significant, especially in some of the smaller data samples. Therefore, a first maximum likelihood fit is performed to the sum of all data samples. Signal peaks are described by the respective signal Monte Carlo shape convolved with a Gaussian distribution accounting for potential differences in resolution. The convolution is defined in Equation (5.6). Background distributions of the  $\eta' \rightarrow \eta\pi^+\pi^-$  and  $f_1 \rightarrow \eta\pi^+\pi^-$  decay modes are described by a second and a third order polynomial, respectively. The resulting parameters from the fit of the background contributions are fixed in subsequent individual fits to each data set to preserve the background shape determined in the overall fit. Only an additional background scale parameter is left free<sup>1</sup>. Results are presented in Figure 6.5 for the data set with the highest statistics at 4.1784 GeV and the one with smallest statistics at 4.2777 GeV. Results for all other data samples can be found in Appendix A.

<sup>1</sup>In case of the  $f_1 \rightarrow \eta\pi^+\pi^-$  reconstruction at  $\sqrt{s} = 3.7730$  GeV center-of-mass energy all background fit parameters are left free. For masses  $m(\eta\pi^+\pi^-)$  near  $1.6 \text{ GeV}/c^2$  the  $p\bar{p}\eta\pi^+\pi^-$  final state is close to the kinematic limit. This slightly changes the background shape compared to all other data samples.

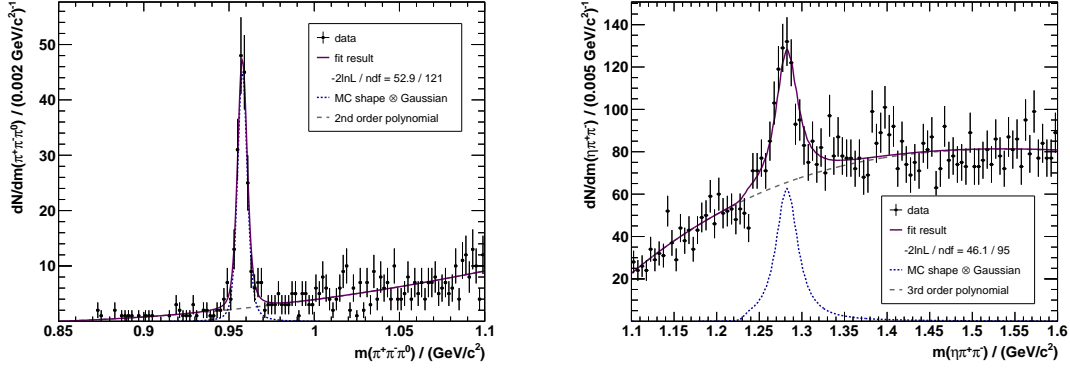


**Figure 6.4.:** Invariant mass distributions of the  $\eta'$  (left) and  $f_1$  (right) meson decay systems after applying all selection criteria. Black dots represent data, summed up over all 17 data samples. The results of the fits, as described in the text, are shown by solid lines and the signal and background components are indicated by blue dotted and gray dashed lines, respectively.

In all four cases, the fit is able to describe the data quite well within statistical uncertainties. In the reconstruction of the  $\eta' \rightarrow \eta\pi^+\pi^-$  decay for the small data set (see Figure 6.5 top right), there are only seven events that survive all selection criteria, five of which are clustered close to the nominal mass of the  $\eta'$  meson. However, such a small enhancement is certainly not significant enough to obtain a reliable cross section value. To quantify this observation for all data sets, a second fit is performed where the signal part of the fit function is omitted. The significance for an  $\eta'$  or  $f_1$  signal is then calculated from the difference of the likelihood values of both fits and the change in number of degrees of freedom. For data sets with a significance greater than  $3\sigma$ , the number of observed events  $N_{\text{obs}}$  is determined as described in Section 5.2 by counting the number of events in the background subtracted invariant mass distribution of the meson candidate within a signal region around its nominal mass value that contains 95 % of the signal peak. Results are listed in Tables 6.3 and 6.4. The data show a significant  $\eta'$  signal contribution in all but four data sets. Although there is a clear  $f_1$  signal peak in the integrated  $\eta\pi^+\pi^-$  mass spectrum of all 17 data samples, individual contributions are significant for only two data samples due to the large background distribution. For these samples, upper limits are determined according to Equation (5.31) with the probability function defined in Equation (5.30) based on Poisson statistics. Results are listed in Tables 6.3 and 6.4.

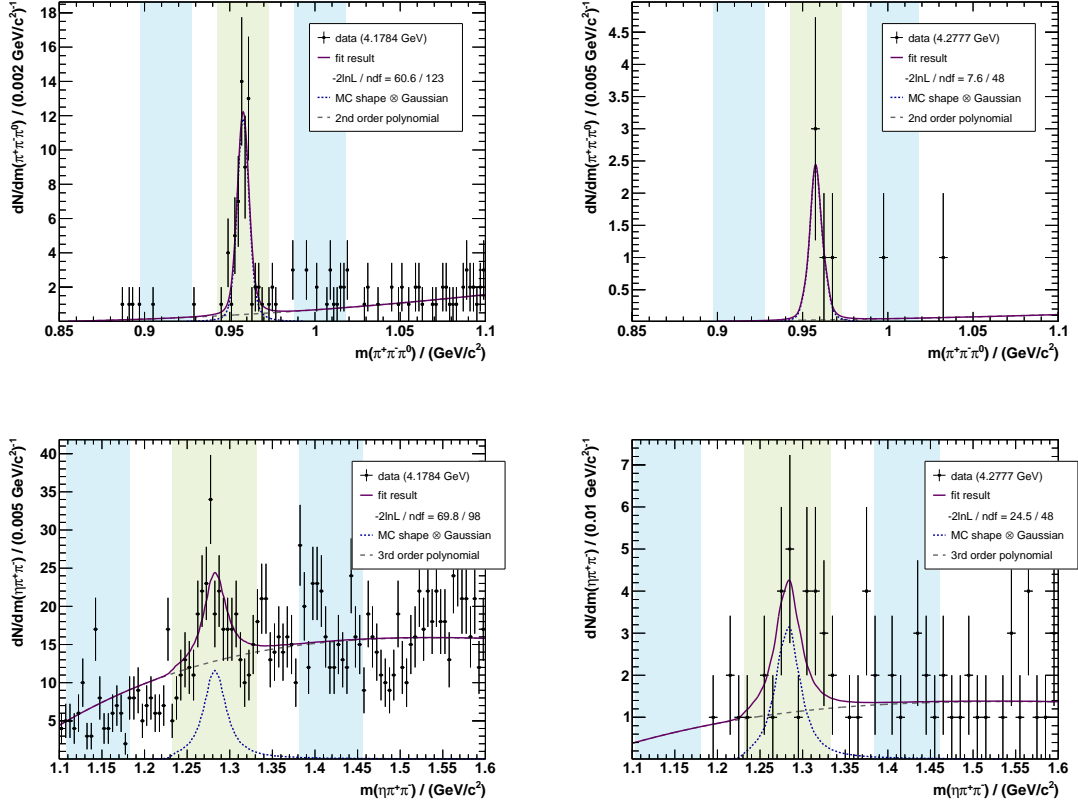


**Figure 6.5.:** Invariant mass of the  $\eta\pi^+\pi^-$  system in the reconstruction of  $\eta'$  (**top**) and  $f_1$  (**bottom**) mesons for the high statistics data set at 4.1784 GeV (**left**) and the one with smallest statistics at 4.2777 GeV (**right**), fitted with the signal MC shape convolved with a Gaussian and a second or third order polynomial. Additionally the signal (green) and sideband regions (blue) are shown.

### 6.3. Efficiency

As already discussed in great detail in Section 5.3, one needs to understand the reconstruction and selection efficiency to calculate cross sections. Since the available statistics in this case is much more limited, a partial wave analysis as described in Section 5.4 is not feasible. Hence, only a simple one-dimensional efficiency determination is performed. The efficiency  $\varepsilon$  is calculated according to Equation (5.9), where the number of accepted events is determined by integrating the invariant mass distribution  $m(\eta\pi^+\pi^-)$  of the Monte Carlo sample within a signal region that contains 95 % of the signal. Results are summarized in Tables 6.3 and 6.4.

**Table 6.3.:** Center-of-mass energies  $\sqrt{s}$ , integrated luminosities  $L$ , correction factors for initial-state radiation ( $1+\delta_r$ ) and vacuum polarization ( $1+\delta_v$ ) as well as number of observed events  $N_{\text{obs}}$ , efficiencies  $\varepsilon$  and the calculated Born cross sections  $\sigma^B(e^+e^- \rightarrow p\bar{p}\eta')$  for 13 data samples which have a significant  $\eta'$  signal contribution (**top**). Additionally, the number of events in the signal region  $N_{\text{tot}}$  and the sideband regions  $N_{\text{bkg}}$  as well as calculated upper limits for the remaining data samples (**bottom**).

$\sqrt{s}$ / GeV	L / pb <sup>-1</sup>	(1 + δ <sub>r</sub> )	(1 + δ <sub>v</sub> )	$N_{\text{obs}}$	$\varepsilon$ / %	$\sigma^B$ / pb
3.7730	2931.8	0.8737	1.0570	29.7 <sup>+9.5</sup> <sub>-6.8</sub>	22.8 ± 0.1	0.29 <sup>+0.09</sup> <sub>-0.07</sub>
4.1784	3189.0	0.9381	1.0543	54.5 <sup>+11.9</sup> <sub>-7.7</sub>	22.5 ± 0.1	0.46 <sup>+0.10</sup> <sub>-0.07</sub>
4.1888	524.6	0.9386	1.0559	9.0 <sup>+5.5</sup> <sub>-3.6</sub>	22.7 ± 0.1	0.45 <sup>+0.28</sup> <sub>-0.18</sub>
4.1989	526.0	0.9393	1.0567	6.8 <sup>+5.3</sup> <sub>-3.3</sub>	22.8 ± 0.1	0.34 <sup>+0.26</sup> <sub>-0.17</sub>
4.2092	518.0	0.9404	1.0565	9.1 <sup>+5.5</sup> <sub>-3.6</sub>	22.5 ± 0.1	0.47 <sup>+0.28</sup> <sub>-0.19</sub>
4.2187	514.6	0.9411	1.0564	8.1 <sup>+5.6</sup> <sub>-3.3</sub>	22.5 ± 0.1	0.42 <sup>+0.29</sup> <sub>-0.17</sub>
4.2263	1056.4	0.9417	1.0562	8.6 <sup>+6.1</sup> <sub>-3.4</sub>	23.2 ± 0.1	0.21 <sup>+0.15</sup> <sub>-0.08</sub>
4.2357	530.3	0.9427	1.0554	6.0 <sup>+5.4</sup> <sub>-3.0</sub>	22.9 ± 0.1	0.29 <sup>+0.27</sup> <sub>-0.15</sub>
4.2580	828.4	0.9447	1.0534	9.4 <sup>+6.1</sup> <sub>-3.4</sub>	23.2 ± 0.1	0.29 <sup>+0.19</sup> <sub>-0.11</sub>
4.2668	531.1	0.9453	1.0532	4.9 <sup>+4.3</sup> <sub>-3.4</sub>	23.0 ± 0.1	0.24 <sup>+0.21</sup> <sub>-0.17</sub>
4.2777	175.7	0.9460	1.0530	4.8 <sup>+4.8</sup> <sub>-2.8</sub>	22.7 ± 0.1	0.72 <sup>+0.72</sup> <sub>-0.43</sub>
4.4156	1043.9	0.9536	1.0524	9.9 <sup>+5.9</sup> <sub>-3.6</sub>	23.3 ± 0.1	0.24 <sup>+0.14</sup> <sub>-0.09</sub>
4.5995	586.9	0.9612	1.0547	4.8 <sup>+4.8</sup> <sub>-2.8</sub>	23.4 ± 0.1	0.20 <sup>+0.21</sup> <sub>-0.12</sub>

$\sqrt{s}$ / GeV	L / pb <sup>-1</sup>	(1 + δ <sub>r</sub> )	(1 + δ <sub>v</sub> )	$N_{\text{tot}}$	$N_{\text{bkg}}$	$\varepsilon$ / %	$\sigma_{\text{UL}}^B$ / pb
3.8695	224.0	0.8998	1.0507	2	2	22.6 ± 0.1	0.55
4.0076	482.0	0.9230	1.0438	4	2	23.0 ± 0.1	0.38
4.2438	538.1	0.9432	1.0555	6	1	22.9 ± 0.1	0.47
4.3583	543.9	0.9509	1.0511	3	0	23.4 ± 0.1	0.30



**Table 6.4.:** Center-of-mass energies  $\sqrt{s}$ , integrated luminosities  $L$ , correction factors for initial-state radiation ( $1+\delta_r$ ) and vacuum polarization ( $1+\delta_v$ ) as well as number of observed events  $N_{\text{obs}}$ , efficiencies  $\varepsilon$  and the calculated Born cross sections  $\sigma^{\text{B}}(\text{e}^+\text{e}^- \rightarrow \text{p}\bar{\text{p}}\text{f}_1)$  for two data samples which have a significant  $\text{f}_1$  signal contribution (**top**). Additionally, the number of events in the signal region  $N_{\text{tot}}$  and the sideband regions  $N_{\text{bkg}}$  as well as calculated upper limits at 90 % confidence level for the remaining data samples (**bottom**).

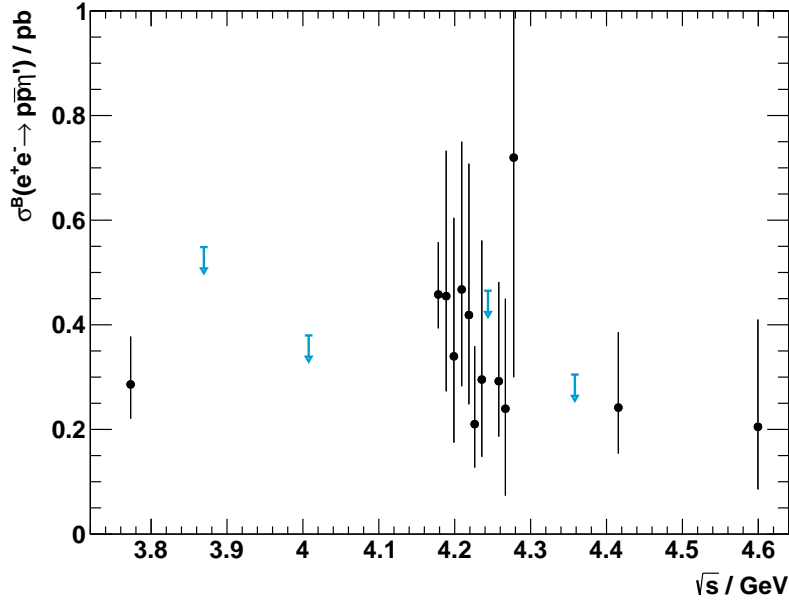
$\sqrt{s}$ / GeV	$L$ / $\text{pb}^{-1}$	$(1 + \delta_r)$	$(1 + \delta_v)$	$N_{\text{obs}}$	$\varepsilon$ / %	$\sigma^{\text{B}}$ / pb
4.0076	482.0	0.9230	1.0438	$26.8^{+12.9}_{-9.1}$	$25.8 \pm 0.1$	$1.62^{+0.78}_{-0.55}$
4.1784	3189.0	0.9381	1.0543	$68.3^{+23.3}_{-18.2}$	$25.3 \pm 0.1$	$0.62^{+0.21}_{-0.17}$

$\sqrt{s}$ / GeV	$L$ / $\text{pb}^{-1}$	$(1 + \delta_r)$	$(1 + \delta_v)$	$N_{\text{tot}}$	$N_{\text{bkg}}$	$\varepsilon$ / %	$\sigma_{\text{UL}}^{\text{B}}$ / pb
3.7730	2931.8	0.8737	1.0570	208	304	$25.7 \pm 0.1$	0.19
3.8695	224.0	0.8998	1.0507	18	14	$25.4 \pm 0.1$	1.97
4.1888	524.6	0.9386	1.0559	22	23	$25.7 \pm 0.1$	0.73
4.1989	526.0	0.9393	1.0567	16	39	$25.8 \pm 0.1$	0.30
4.2092	518.0	0.9404	1.0565	19	32	$25.4 \pm 0.1$	0.44
4.2187	514.6	0.9411	1.0564	20	21	$25.6 \pm 0.1$	0.70
4.2263	1056.4	0.9417	1.0562	54	47	$26.2 \pm 0.1$	0.80
4.2357	530.3	0.9427	1.0554	25	23	$25.9 \pm 0.1$	0.86
4.2438	538.1	0.9432	1.0555	25	17	$25.9 \pm 0.1$	1.05
4.2580	828.4	0.9447	1.0534	26	41	$26.4 \pm 0.1$	0.31
4.2668	531.1	0.9453	1.0532	21	21	$26.0 \pm 0.1$	0.72
4.2777	175.7	0.9460	1.0530	10	12	$25.6 \pm 0.1$	1.28
4.3583	543.9	0.9509	1.0511	26	22	$26.5 \pm 0.1$	0.91
4.4156	1043.9	0.9536	1.0524	36	34	$26.1 \pm 0.1$	0.55
4.5995	586.9	0.9612	1.0547	15	23	$25.9 \pm 0.1$	0.38

## 6.4. Born Cross Sections

Now that all necessary observables have been determined, the Born cross sections are calculated with Equation (5.1). Results are listed in Tables 6.3 and 6.4 and are graphically depicted in Figure 6.6 for the  $p\bar{p}\eta'$  final state. The data shows a small enhancement in the cross section at around 4.18 GeV. This could hint towards a resonant contribution of the  $\psi(4160)$  as seen, for example, in the  $p\bar{p}\eta$  line shape via an intermediate  $J/\psi \rightarrow p\bar{p}$  decay. A similar enhancement is seen in a recent analysis of  $e^+e^- \rightarrow \eta'J/\psi$  by BESIII [124]. Their results cannot be properly described by a single  $\psi(4160)$ , but by a coherent sum of  $\psi(4160)$  and  $\psi(4260)$ . An additional enhancement of  $\psi(4260)$  is not seen in this work. Three maximum likelihood fits are performed according to Equations (5.32) to (5.34): The pure continuum contribution as well as an additional coherent or incoherent Breit-Wigner resonance. Mass  $m$  and width  $\Gamma$  are again fixed to the  $\psi(4160)$  average values of the PDG, i.e.,  $m_{\psi(4160)} = 4191(5)$  MeV and  $\Gamma_{\psi(4160)} = 70(10)$  MeV. The interpretation of these fits shown in Figure 6.7 appears to be quite difficult. Due to the lack of data in the center-of-mass energy region between 3.7730 GeV and 4.1784 GeV, the shape of the continuum contribution is heavily dependent on the data point at 3.7730 GeV. The significance of such a resonant contribution is evaluated to be  $2.2\sigma$  and  $2.1\sigma$  for the coherent and incoherent case, respectively. These values do not include any systematic uncertainties.



**Figure 6.6.:** Born cross sections  $\sigma^B(e^+e^- \rightarrow p\bar{p}\eta')$  and upper limits. Black dots represent the 13 data samples with significant  $\eta'$  contribution in the  $\eta\pi^+\pi^-$  invariant mass, open circles are the expected cross section values for all other data sets and arrows indicate the corresponding upper limits. Uncertainties are statistical only.

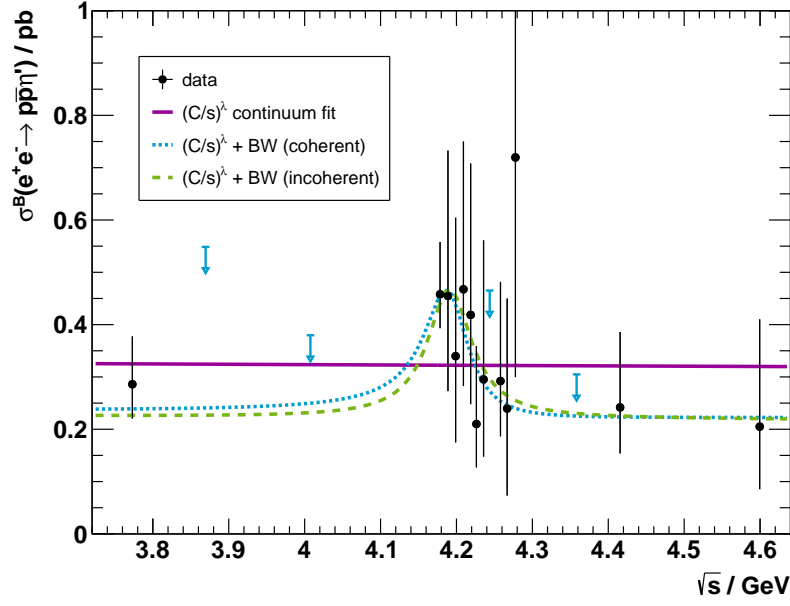


**Figure 6.7.:** Born cross sections  $\sigma^B(e^+e^- \rightarrow p\bar{p}\eta')$  and upper limits. Black dots represent the 13 data samples with significant  $\eta'$  contribution in the  $\eta\pi^+\pi^-$  invariant mass, open circles are the expected cross section values for all other data sets and arrows indicate the corresponding upper limits. Uncertainties are statistical only. Three maximum likelihood fits are shown, as described in the text: Continuum contribution only (solid line), as well as adding one Breit-Wigner resonance coherently (dotted line) or incoherently (dashed line).



## 7. Outlook

In the outlook chapter of this thesis, new high luminosity data samples will be shortly discussed. As mentioned before, the BESIII collaboration initiated a systematic scan to precisely study the line shape of exotic candidates by accumulating high luminosity data sets in the energy region  $4.1 \text{ GeV} \leq \sqrt{s} \leq 4.6 \text{ GeV}$ . The available database is continuously expanded and in the last run period eight data samples were recorded (4.1285, 4.1574, 4.2879, 4.3121, 4.3374, 4.3774, 4.3965 and 4.4362 GeV). Since the final calibration of this data is still in progress, results have to be considered preliminary.

The  $p\bar{p}\eta$  and  $p\bar{p}\omega$  final states are reconstructed and all necessary observables are determined as described in Chapter 5. Resulting Born cross sections are listed in Table 7.1 and are graphically depicted in Figure 7.1 together with the values of the fully analyzed other 17 high luminosity data samples. Note that the luminosities which are used are design values of the respective run period. However, the eight new data points already fit quite well into the profile of the previous data points and do not reveal any significant resonant structure.

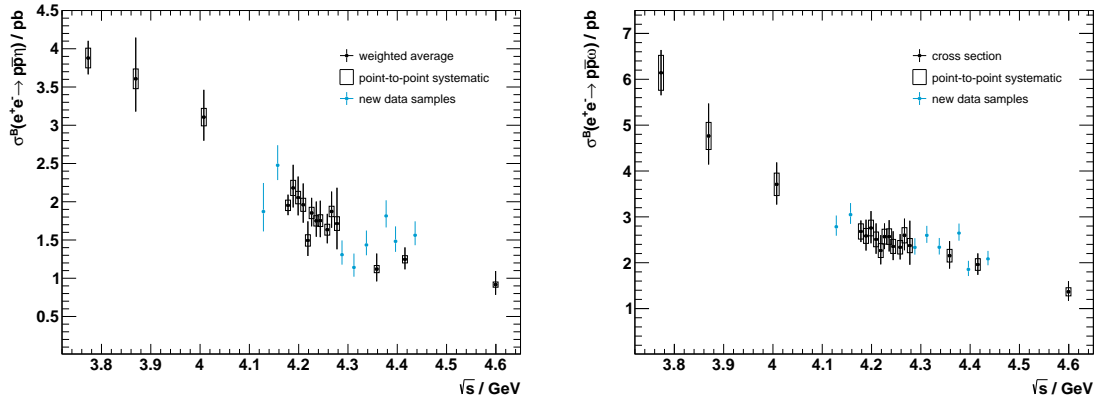


**Figure 7.1.:** Born cross sections for the  $p\bar{p}\eta$  (left) and  $p\bar{p}\omega$  (right) final states with their corresponding total uncertainties, including statistical and systematic uncertainties. Open squares indicate point-to-point systematics. Points from the eight new high luminosity data samples are presented by blue dots. Note, however, that the final calibration of this data as well as the determination of integrated luminosities is still in progress.

**Table 7.1.:** Center-of-mass energies  $\sqrt{s}$ , integrated luminosities  $L$  as well as the calculated Born cross sections for the eight new high luminosity data samples. Uncertainties are statistical only.

$\sqrt{s}$ / GeV	$L$ / pb $^{-1}$	$\bar{\sigma}^B(e^+e^- \rightarrow p\bar{p}\eta)$	$\sigma^B(e^+e^- \rightarrow p\bar{p}\omega)$ / pb
4.1285	400	$1.87^{+0.37}_{-0.26}$	$2.78^{+0.25}_{-0.20}$
4.1574	400	$2.48^{+0.26}_{-0.19}$	$3.05^{+0.25}_{-0.20}$
4.2879	500	$1.31^{+0.19}_{-0.13}$	$2.33^{+0.20}_{-0.16}$
4.3121	500	$1.14^{+0.18}_{-0.12}$	$2.60^{+0.21}_{-0.17}$
4.3374	500	$1.44^{+0.19}_{-0.14}$	$2.34^{+0.20}_{-0.16}$
4.3774	500	$1.81^{+0.20}_{-0.15}$	$2.65^{+0.21}_{-0.17}$
4.3965	500	$1.48^{+0.20}_{-0.14}$	$1.85^{+0.19}_{-0.14}$
4.4362	570	$1.56^{+0.18}_{-0.13}$	$2.08^{+0.17}_{-0.14}$

## 8. Conclusion

The studies presented in this thesis have shown that the high statistics data recorded in  $e^+e^-$  annihilations with the BESIII experiment allow to extract cross sections for several light hadron final states involving a  $p\bar{p}$  pair and to investigate possible couplings of exotic charmonia to these final states down to a precision of 0.42 pb. Born cross sections have been determined in the center-of-mass energy region  $3.7730 \text{ GeV} \leq \sqrt{s} \leq 4.5995 \text{ GeV}$  for reactions of the form  $e^+e^- \rightarrow p\bar{p}m$ , where  $m$  is a pseudoscalar ( $\eta, \eta'$ ), a vector ( $\omega$ ) or a pseudovector meson ( $f_1$ ).

In the main part of this thesis, a full analysis of  $e^+e^- \rightarrow p\bar{p}\eta$  and  $e^+e^- \rightarrow p\bar{p}\omega$  was carried out, including the investigation of statistical and systematic uncertainties. Both mesons were reconstructed by their decay products from hadronic decays into  $\pi^+\pi^-\pi^0$ . The  $\eta$  meson was additionally reconstructed via its electromagnetic decay into two photons. In all three decay channels, the mesons were clearly identified on top of rather small background distributions thanks to the excellent (anti-)proton identification of the BESIII detection system. For the precise evaluation of the Born cross sections it was necessary to perform a multidimensional efficiency determination. This was achieved by an effective description of the data using a partial wave analysis, one of the most sophisticated tools in hadron spectroscopy. No significant resonant structure could be observed in the cross section of the process  $e^+e^- \rightarrow p\bar{p}m$  and upper limits were calculated with a maximum likelihood method for a variety of different mass and width hypotheses of possible resonant contributions from heavy vector resonances. Born cross sections  $\sigma^B(e^+e^- \rightarrow p\bar{p}\eta)$  and  $\sigma^B(e^+e^- \rightarrow p\bar{p}\omega)$  in this energy regime are dominated by the continuum production of the respective final state. The detection of possible vector resonances is limited by the statistical and systematic uncertainties. For example, the  $\psi(4160)$  has a small coupling to  $\eta J/\psi$ , as seen in previous analyses by the Belle [31] and the BESIII [32, 33] collaborations using the dominant  $J/\psi \rightarrow l^+l^-$  decay. The process  $e^+e^- \rightarrow \eta(J/\psi \rightarrow p\bar{p})$  provided a unique opportunity to cross check the analysis procedure developed in this work, and all determined values were in very good agreement with previous results. Due to the small branching fraction  $\mathcal{B}r(J/\psi \rightarrow p\bar{p}) = 0.2121(29) \%$  [36], the amplitude of such a signal is in the order of the total uncertainty of this measurement and is therefore not significant enough to be unambiguously detected in the full process  $e^+e^- \rightarrow p\bar{p}\eta$  without additional selection criteria. A glimpse at new high luminosity data sets was presented in the outlook

chapter of this thesis. The accumulation of these data samples has only recently been completed at the end of June 2019 and the final calibration as well as the determination of integrated luminosities is still in progress. These supplemental data points will help to get a better understanding of the dominant continuum production process and improve the informative value of this analysis. Additionally, the BESIII collaboration will start a new run period by the end of this year. During the summer shutdown BEPCII was upgraded and now provides  $e^+e^-$  collisions at center-of-mass energies of up to 4.7 GeV. This allows to investigate the  $\psi(4660)$  and extend the energy range of this study in subsequent analyses.

The cross sections determined in this work are of great importance for the forthcoming proton-antiproton annihilation experiment PANDA, where (exotic) charmonia could be produced in association to a light meson, such as an  $\eta$  or  $\omega$  [125]. Estimates of charmonium production cross sections can be used to formulate detection strategies and investigate luminosity requirements.

In addition, the reactions  $e^+e^- \rightarrow p\bar{p}\eta'$  and  $e^+e^- \rightarrow p\bar{p}f_1$  were studied with both mesons reconstructed in the  $\eta\pi^+\pi^-$  decay mode, which in this case was strongly limited by statistics. Based on the analysis procedure developed throughout the main part of this thesis, cross sections were determined for the first time in this energy regime. In case of the  $f_1$  meson, upper limits were determined for all but two data samples at 4.0076 GeV and 4.1784 GeV, due to limited statistics and a large irreducible background distribution from direct  $\eta\pi^+\pi^-$  production. Born cross section values for  $p\bar{p}\eta'$  were calculated for all but four data sets at 3.8695, 4.0076, 4.2438 and 4.3583 GeV. A small enhancement in the cross section profile could be observed around 4.18 GeV center-of-mass energy. Similar to the structure seen in  $e^+e^- \rightarrow \eta J/\psi$ , a recent analysis of  $e^+e^- \rightarrow \eta' J/\psi$  by BESIII has revealed a significant contribution of  $\psi(4160)$  and  $\psi(4260)$  [124]. An additional enhancement of  $\psi(4260)$  is not seen in this work. Therefore, it is very unlikely that the observed structure is caused by  $e^+e^- \rightarrow \psi(4160) \rightarrow \eta'(J/\psi \rightarrow p\bar{p})$ . A direct decay of  $\psi(4160) \rightarrow p\bar{p}\eta'$  is expected to be even less significant, and in fact maximum likelihood fits yield values of  $2.2\sigma$  and  $2.1\sigma$  for a coherent and incoherent  $\psi(4160)$  resonant contribution, respectively. Hence, the structure is an artifact due to statistical fluctuations.

As a final summary of the work presented here, it shall be re-emphasized that the main goal was to determine Born cross sections for reactions of the form  $e^+e^- \rightarrow p\bar{p}m$ . For the first time, cross sections have been calculated at various center-of-mass energies between 3.7730 GeV and 4.5595 GeV for  $p\bar{p}\eta$  and  $p\bar{p}\omega$ , using the high statistics data sets from the BESIII experiment. In addition, a secondary analysis of  $p\bar{p}\eta'$  and  $p\bar{p}f_1$  was successfully performed, resulting in a new database where no information was previously available.



---

At this time, there are no theoretical predictions concerning the coupling of heavy charmonia to light hadron final states involving a  $p\bar{p}$  pair. Not observing any resonant contributions in these charmless final states indicates that heavy (exotic) charmonia strongly prefer to preserve their charm content. No matter whether it is a conventional charmonium  $c\bar{c}$ , a hybrid  $c\bar{c}g$  or a molecular state  $c\bar{c}q\bar{q}$ , they preferably decay into  $c\bar{c} q\bar{q}$  or  $c\bar{q} \bar{c}q$  final states, and do not annihilate into nothing but light quarks.



## A. Appendix

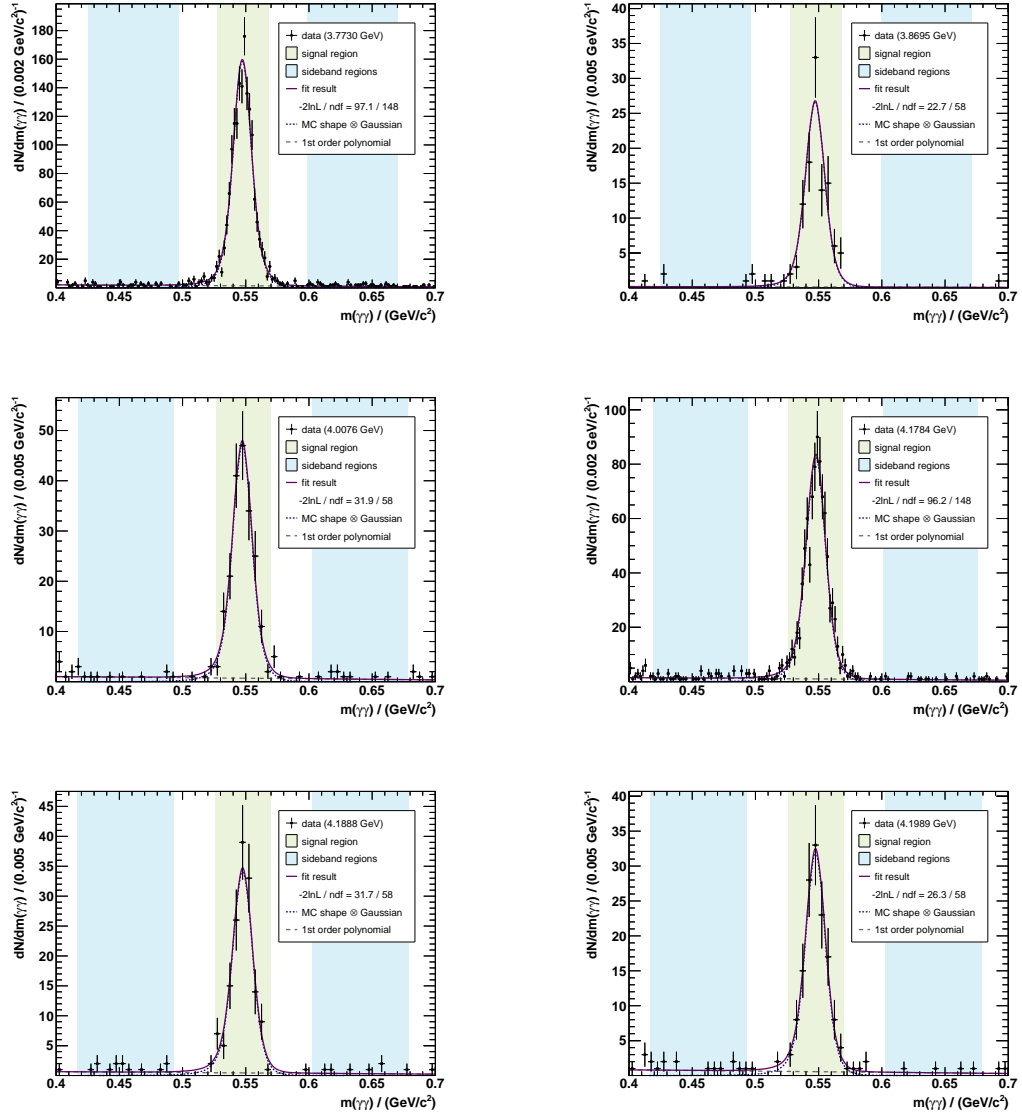


**Figure A.1.:** Invariant mass of the  $\eta$  system in the reconstruction of  $e^+e^- \rightarrow p\bar{p}(\eta \rightarrow \gamma\gamma)$  for center-of-mass energies from 3.7730 GeV to 4.1989 GeV (left to right and top to bottom), fitted with the signal MC shape convolved with a Gaussian and a first order polynomial. Additionally the signal (green) and sideband regions (blue) are shown.

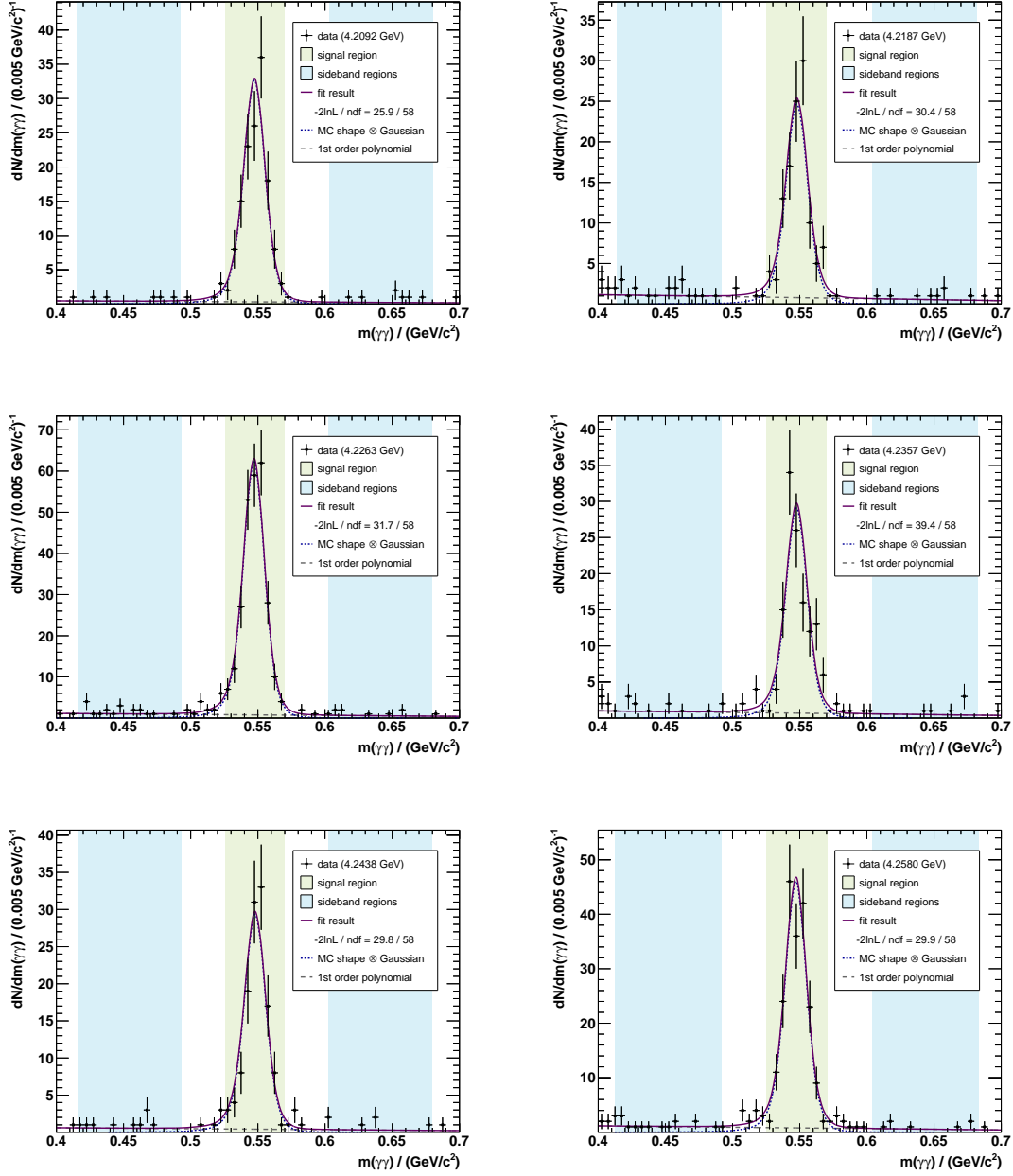


**Figure A.2.:** Invariant mass of the  $\eta$  system in the reconstruction of  $e^+e^- \rightarrow p\bar{p}(\eta \rightarrow \gamma\gamma)$  for center-of-mass energies from 4.2092 GeV to 4.2580 GeV (left to right and top to bottom), fitted with the signal MC shape convolved with a Gaussian and a first order polynomial. Additionally the signal (green) and sideband regions (blue) are shown.

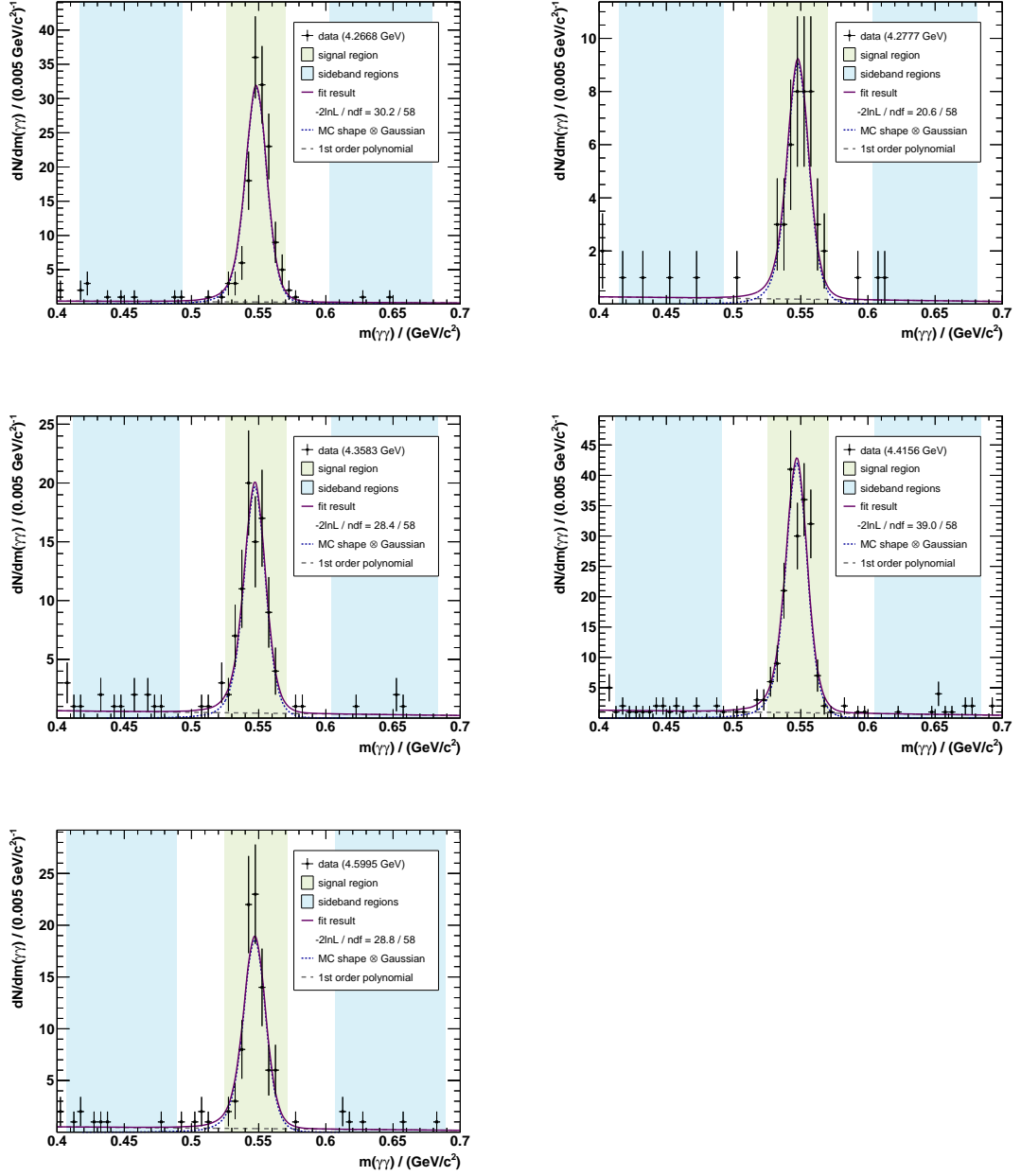


**Figure A.3.:** Invariant mass of the  $\eta$  system in the reconstruction of  $e^+e^- \rightarrow p\bar{p}(\eta \rightarrow \gamma\gamma)$  for center-of-mass energies from 4.2668 GeV to 4.5995 GeV (left to right and top to bottom), fitted with the signal MC shape convolved with a Gaussian and a first order polynomial. Additionally the signal (green) and sideband regions (blue) are shown.

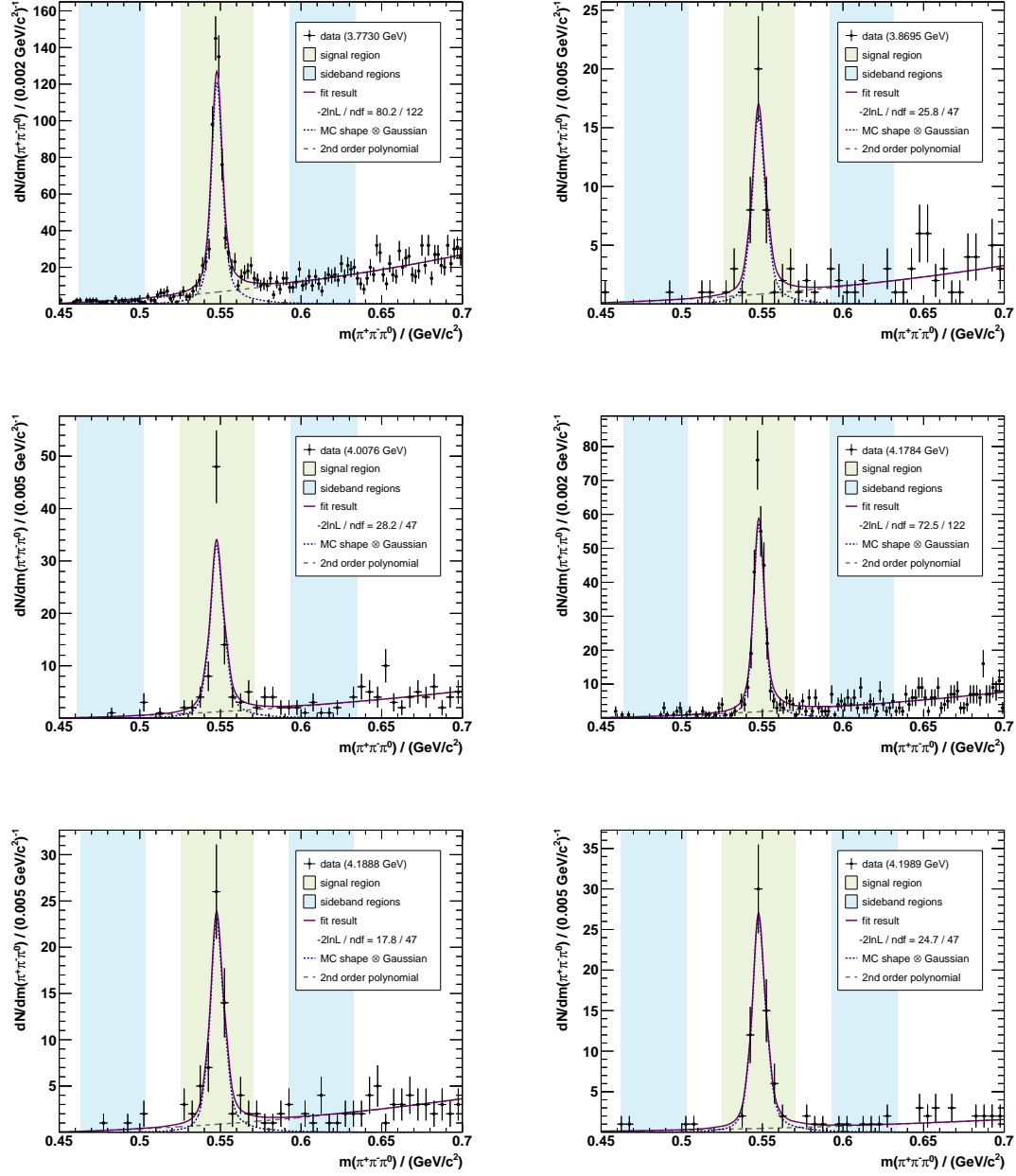


**Figure A.4.:** Invariant mass of the  $\eta$  system in the reconstruction of  $e^+e^- \rightarrow p\bar{p}(\eta \rightarrow \pi^+\pi^-\pi^0)$  for center-of-mass energies from 3.7730 GeV to 4.1989 GeV (left to right and top to bottom), fitted with the signal MC shape convolved with a Gaussian and a second order polynomial. Additionally the signal (green) and sideband regions (blue) are shown.

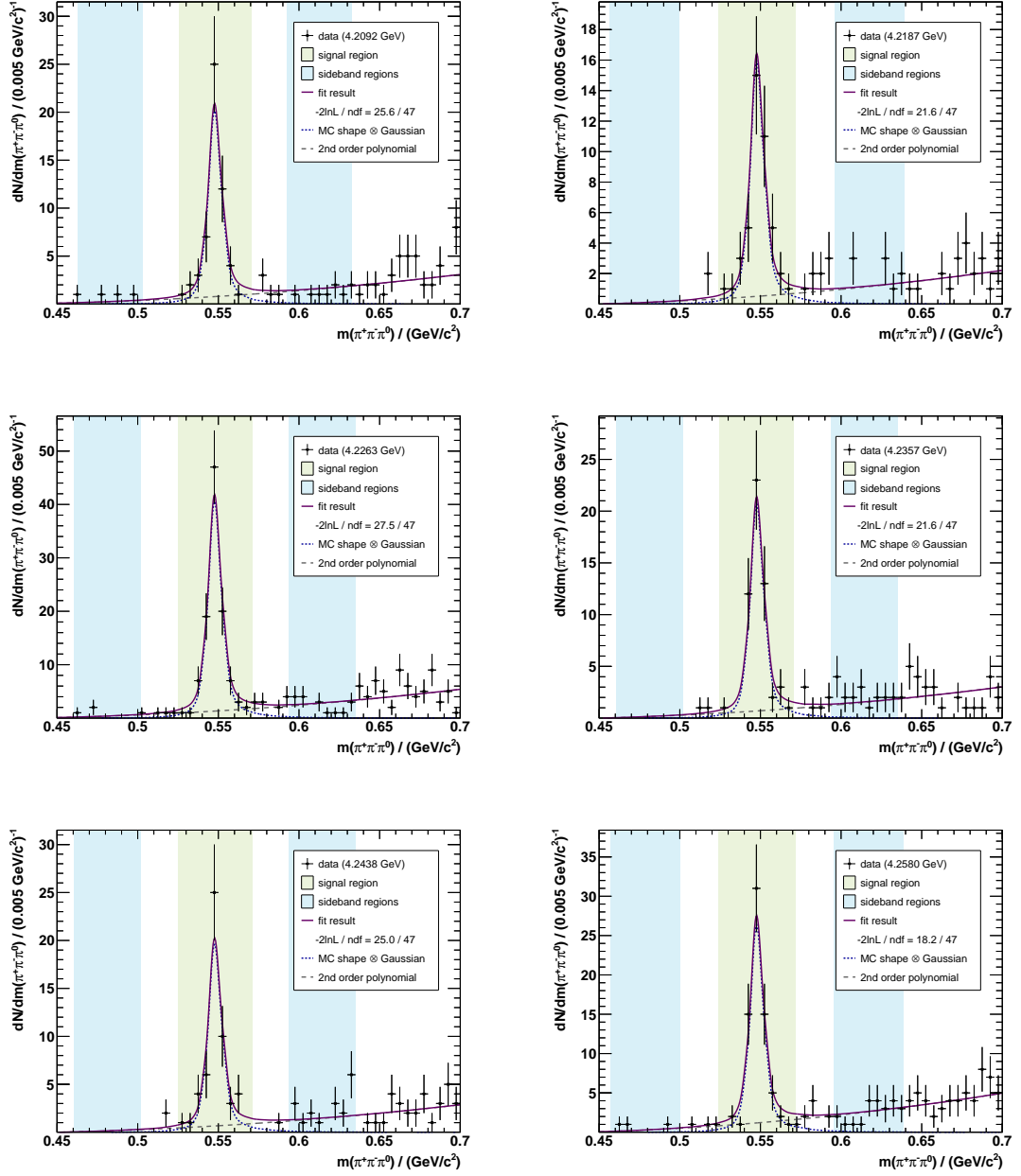


**Figure A.5.:** Invariant mass of the  $\eta$  system in the reconstruction of  $e^+e^- \rightarrow p\bar{p}(\eta \rightarrow \pi^+\pi^-\pi^0)$  for center-of-mass energies from 4.2092 GeV to 4.2580 GeV (left to right and top to bottom), fitted with the signal MC shape convolved with a Gaussian and a second order polynomial. Additionally the signal (green) and sideband regions (blue) are shown.

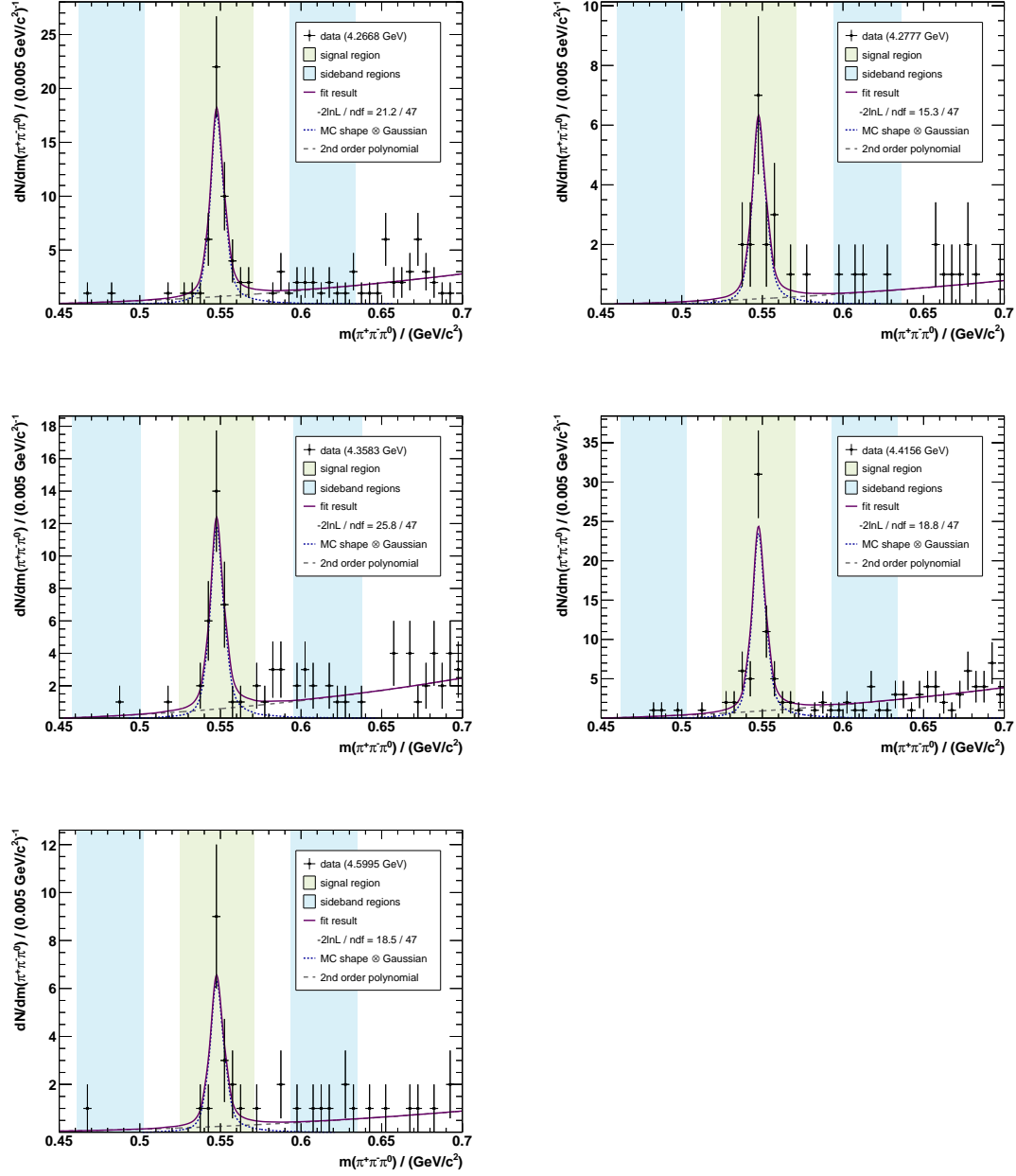


**Figure A.6.:** Invariant mass of the  $\eta$  system in the reconstruction of  $e^+e^- \rightarrow p\bar{p}(\eta \rightarrow \pi^+\pi^-\pi^0)$  for center-of-mass energies from 4.2668 GeV to 4.5995 GeV (left to right and top to bottom), fitted with the signal MC shape convolved with a Gaussian and a second order polynomial. Additionally the signal (green) and sideband regions (blue) are shown.



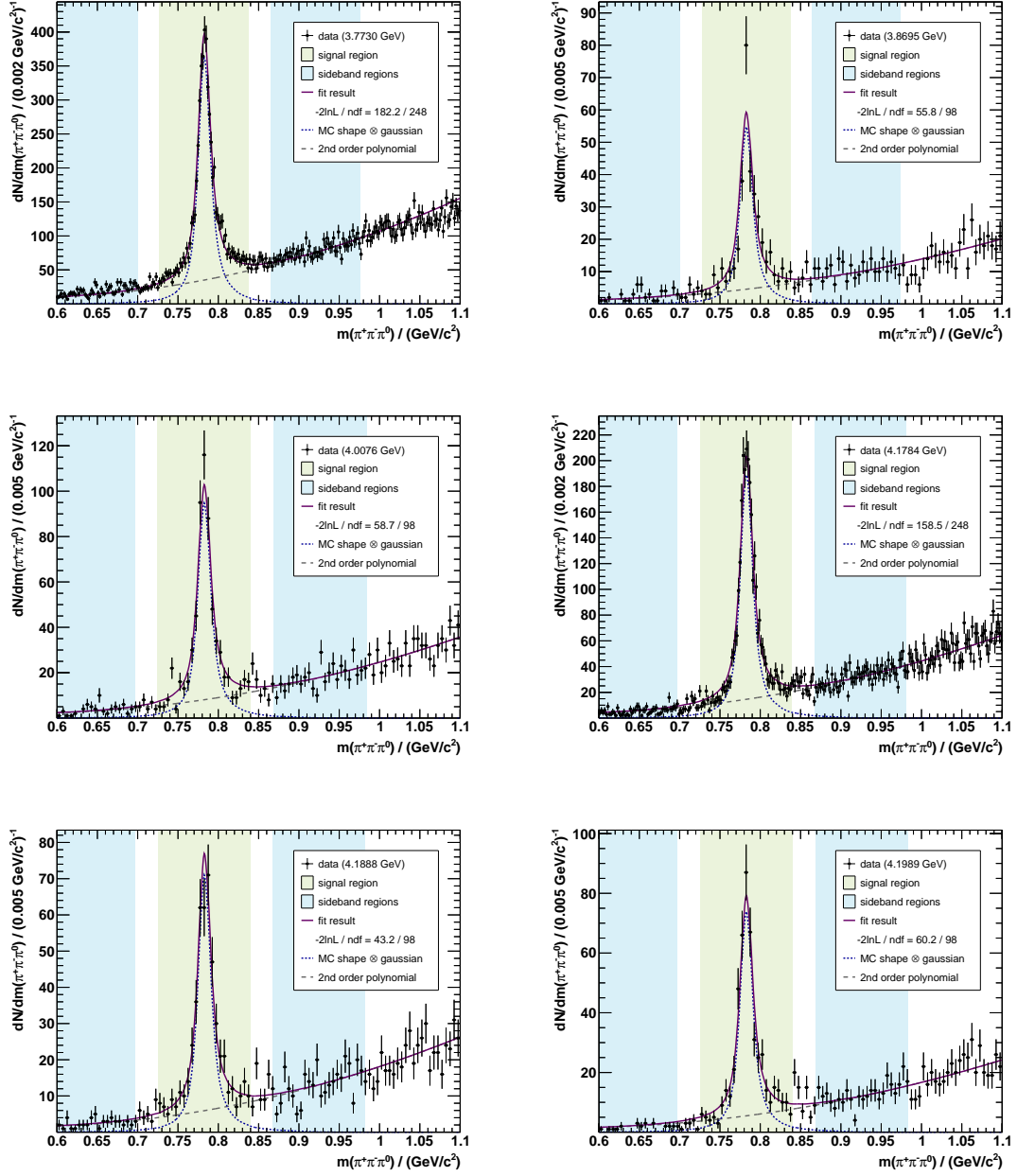


**Figure A.7.:** Invariant mass of the  $\omega$  system in the reconstruction of  $e^+e^- \rightarrow p\bar{p}(\omega \rightarrow \pi^+\pi^-\pi^0)$  for center-of-mass energies from 3.7730 GeV to 4.1989 GeV (left to right and top to bottom), fitted with the signal MC shape convolved with a Gaussian and a second order polynomial. Additionally the signal (green) and sideband regions (blue) are shown.

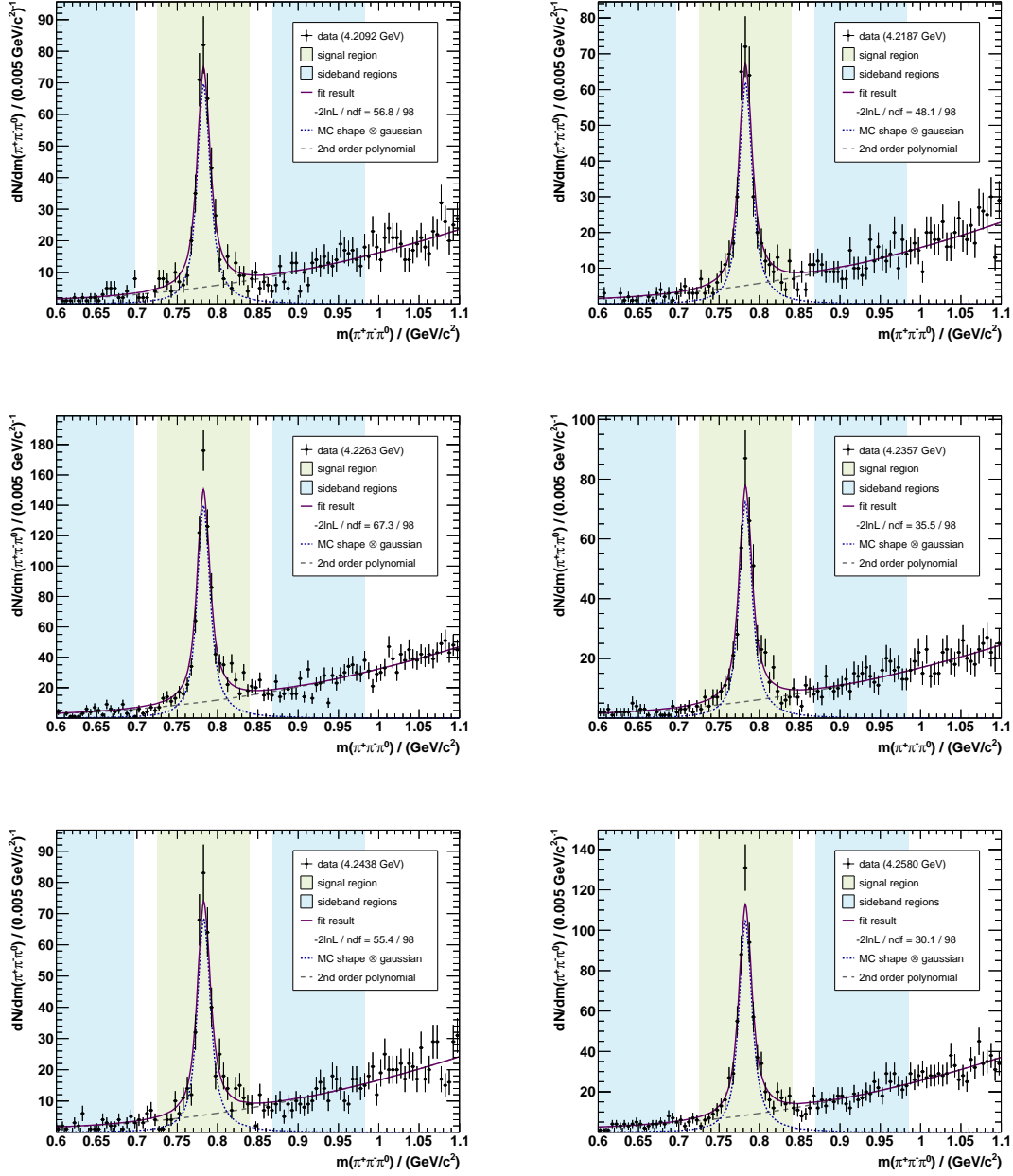


**Figure A.8.:** Invariant mass of the  $\omega$  system in the reconstruction of  $e^+e^- \rightarrow p\bar{p}(\omega \rightarrow \pi^+\pi^-\pi^0)$  for center-of-mass energies from 4.2092 GeV to 4.2580 GeV (left to right and top to bottom), fitted with the signal MC shape convolved with a Gaussian and a second order polynomial. Additionally the signal (green) and sideband regions (blue) are shown.

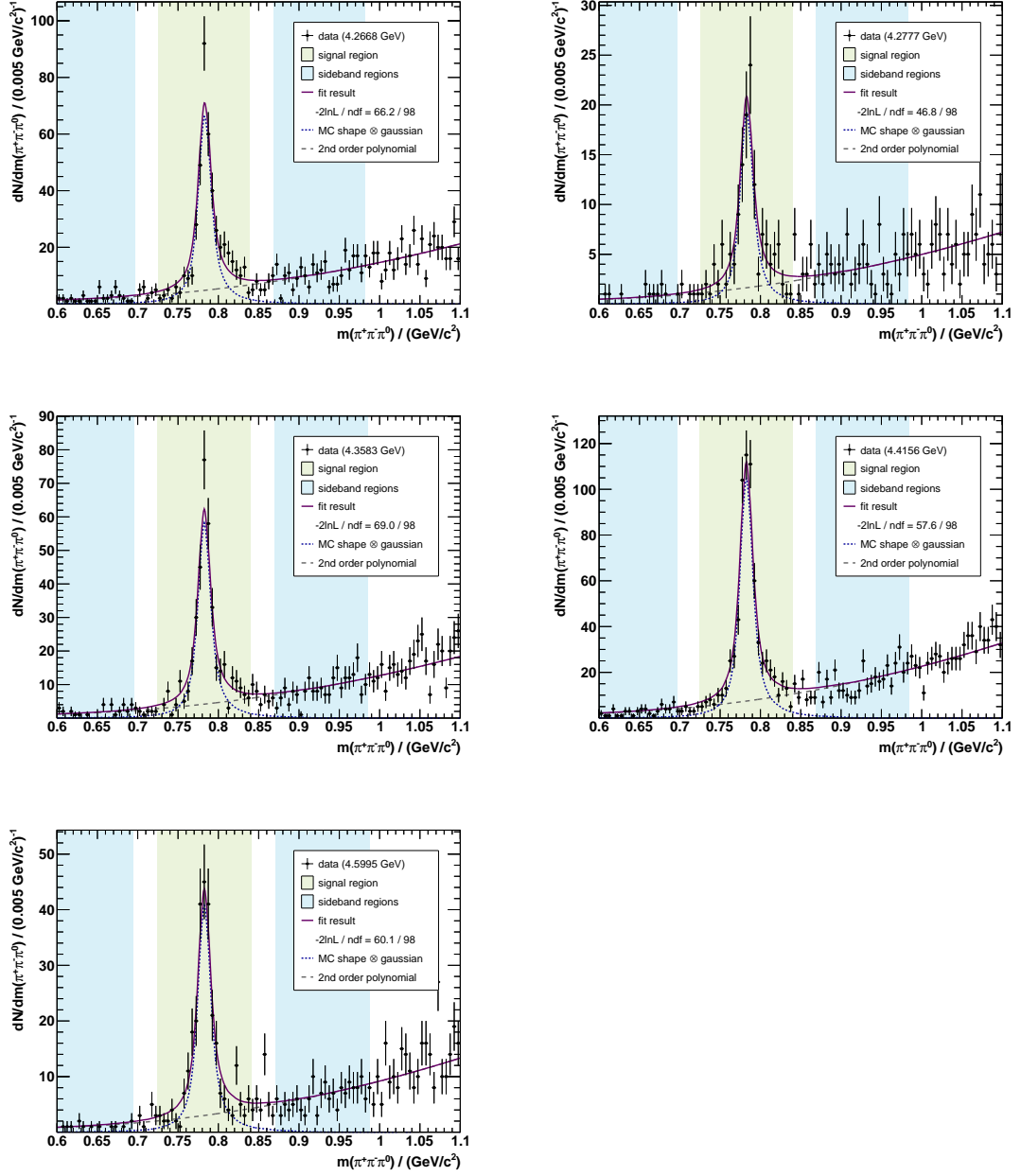


**Figure A.9.:** Invariant mass of the  $\omega$  system in the reconstruction of  $e^+e^- \rightarrow p\bar{p}(\omega \rightarrow \pi^+\pi^-\pi^0)$  for center-of-mass energies from 4.2668 GeV to 4.5995 GeV (left to right and top to bottom), fitted with the signal MC shape convolved with a Gaussian and a second order polynomial. Additionally the signal (green) and sideband regions (blue) are shown.

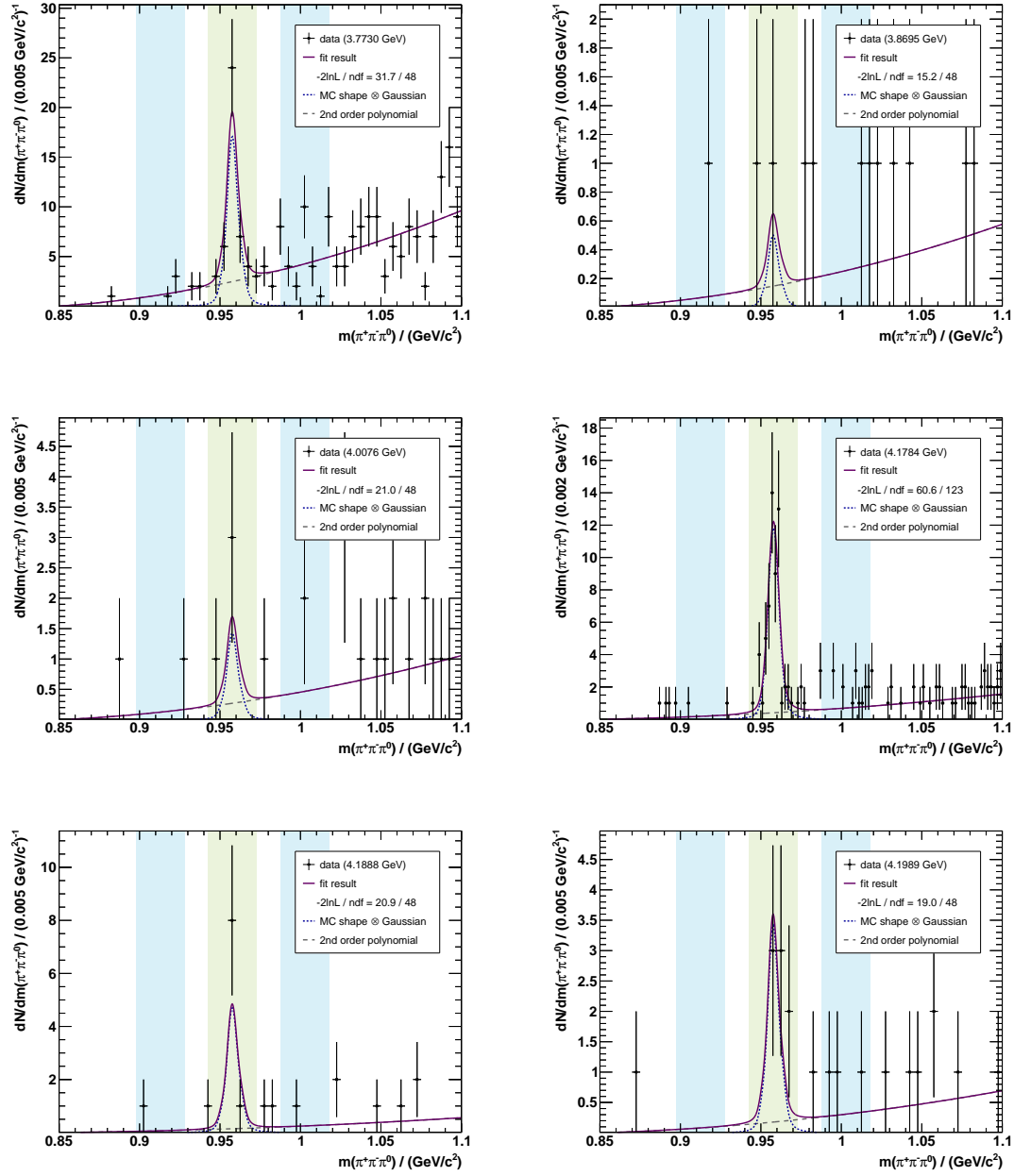


**Figure A.10.:** Invariant mass of the  $\eta\pi^+\pi^-$  system in the reconstruction of  $p\bar{p}\eta'$  for center-of-mass energies from 3.7730 GeV to 4.1989 GeV (left to right and top to bottom), fitted with the signal MC shape convolved with a Gaussian and a second order polynomial. Additionally the signal (green) and sideband regions (blue) are shown.

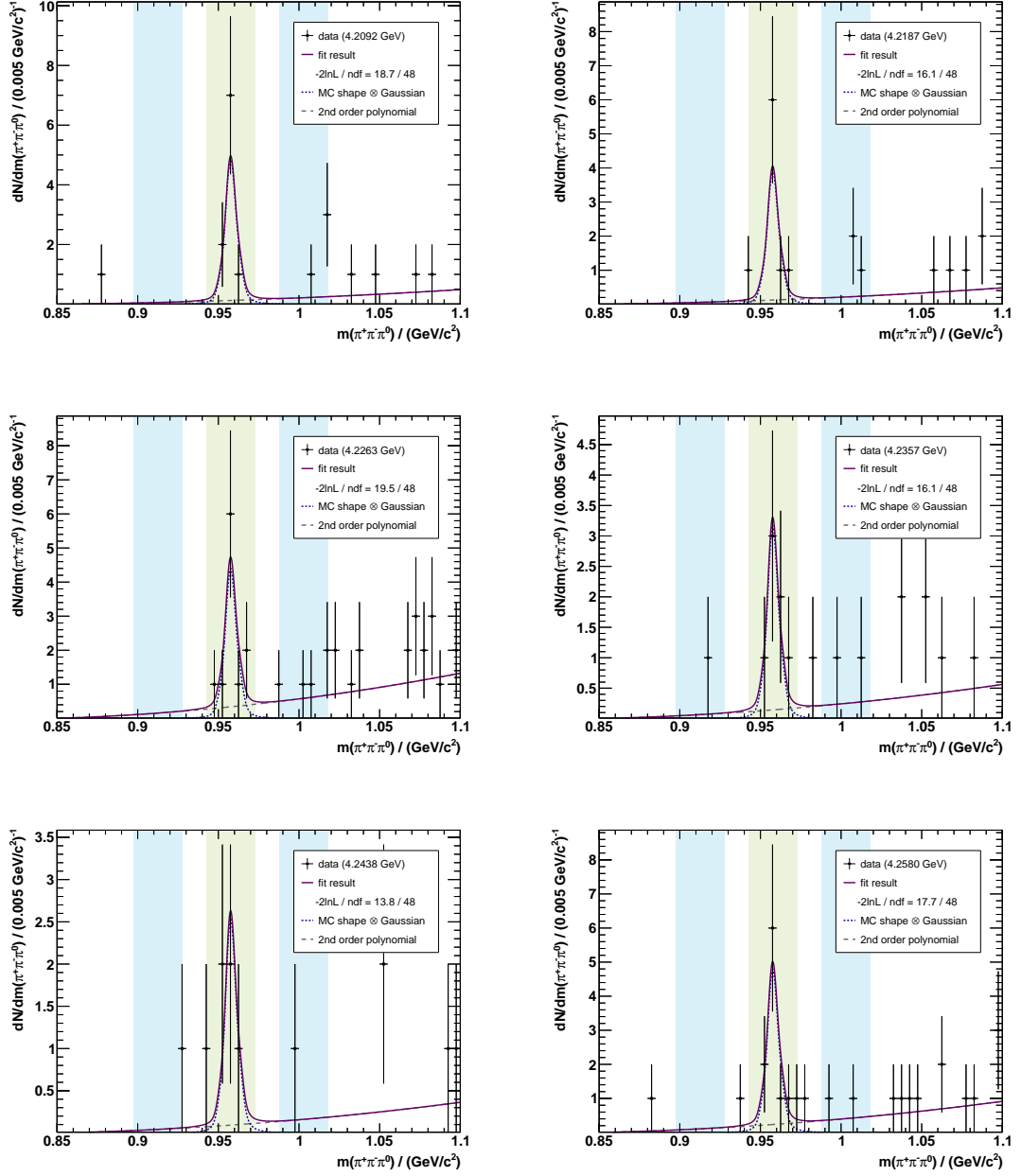


**Figure A.11.:** Invariant mass of the  $\eta\pi^+\pi^-$  system in the reconstruction of  $p\bar{p}\eta'$  for center-of-mass energies from 4.2092 GeV to 4.2580 GeV (left to right and top to bottom), fitted with the signal MC shape convolved with a Gaussian and a second order polynomial. Additionally the signal (green) and sideband regions (blue) are shown.

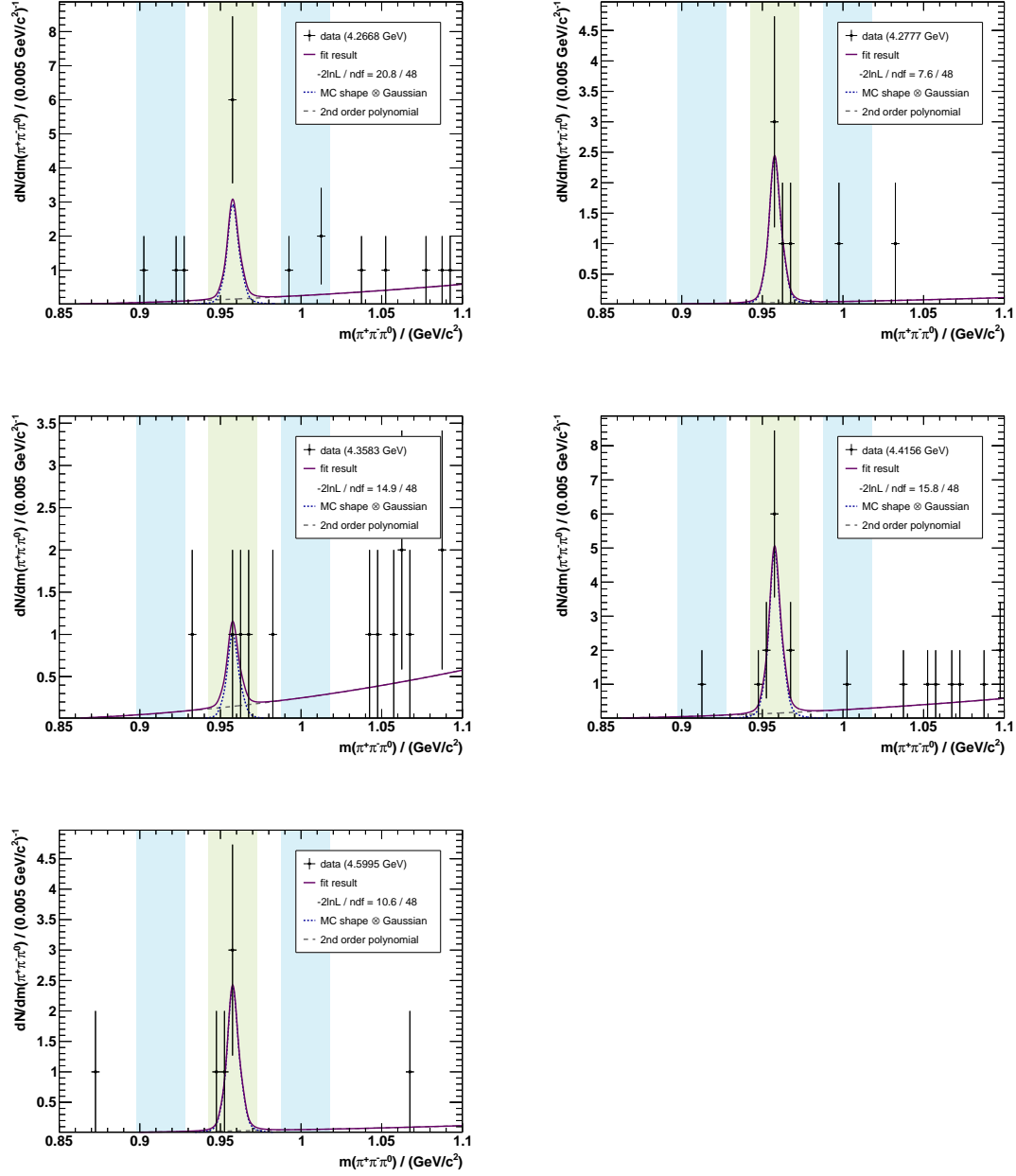


**Figure A.12.:** Invariant mass of the  $\eta\pi^+\pi^-$  system in the reconstruction of  $p\bar{p}\eta'$  for center-of-mass energies from 4.2668 GeV to 4.5995 GeV (left to right and top to bottom), fitted with the signal MC shape convolved with a Gaussian and a second order polynomial. Additionally the signal (green) and sideband regions (blue) are shown.

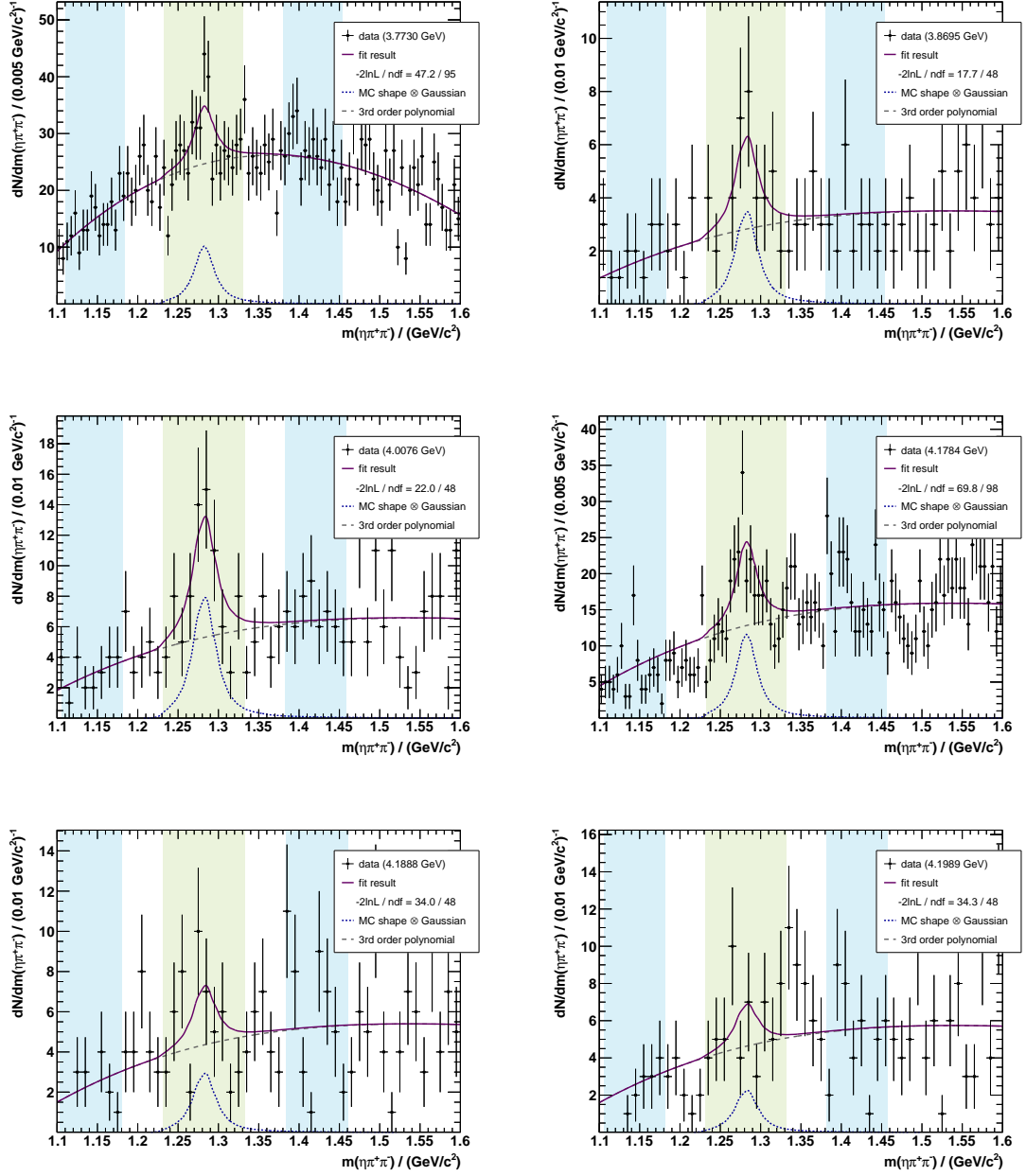


**Figure A.13.:** Invariant mass of the  $\eta\pi^+\pi^-$  system in the reconstruction of  $p\bar{p}f_1$  for center-of-mass energies from 3.7730 GeV to 4.1989 GeV (left to right and top to bottom), fitted with the signal MC shape convolved with a Gaussian and a third order polynomial. Additionally the signal (green) and sideband regions (blue) are shown.

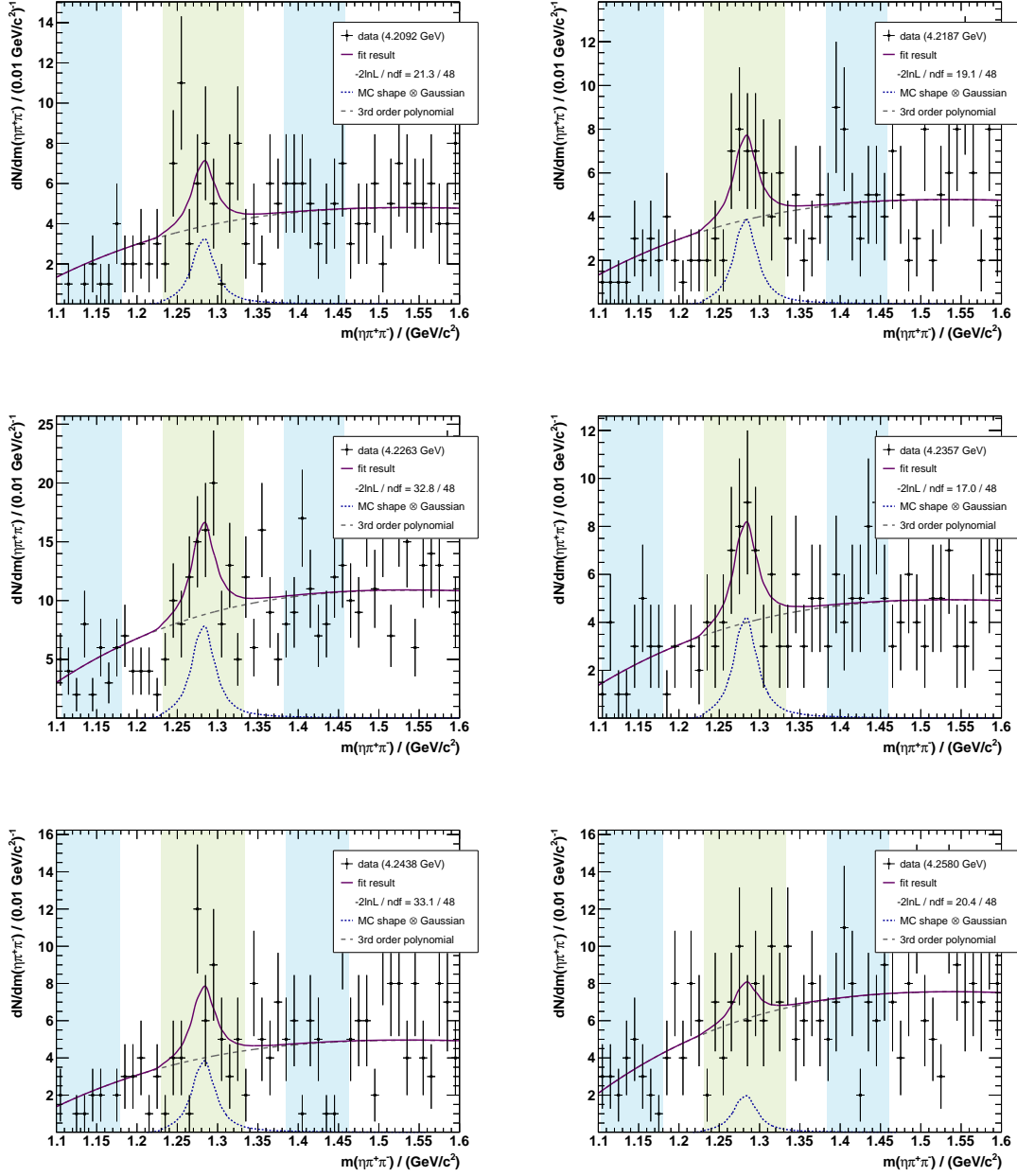


**Figure A.14.:** Invariant mass of the  $\eta\pi^+\pi^-$  system in the reconstruction of  $p\bar{p}f_1$  for center-of-mass energies from 4.2092 GeV to 4.2580 GeV (left to right and top to bottom), fitted with the signal MC shape convolved with a Gaussian and a third order polynomial. Additionally the signal (green) and sideband regions (blue) are shown.



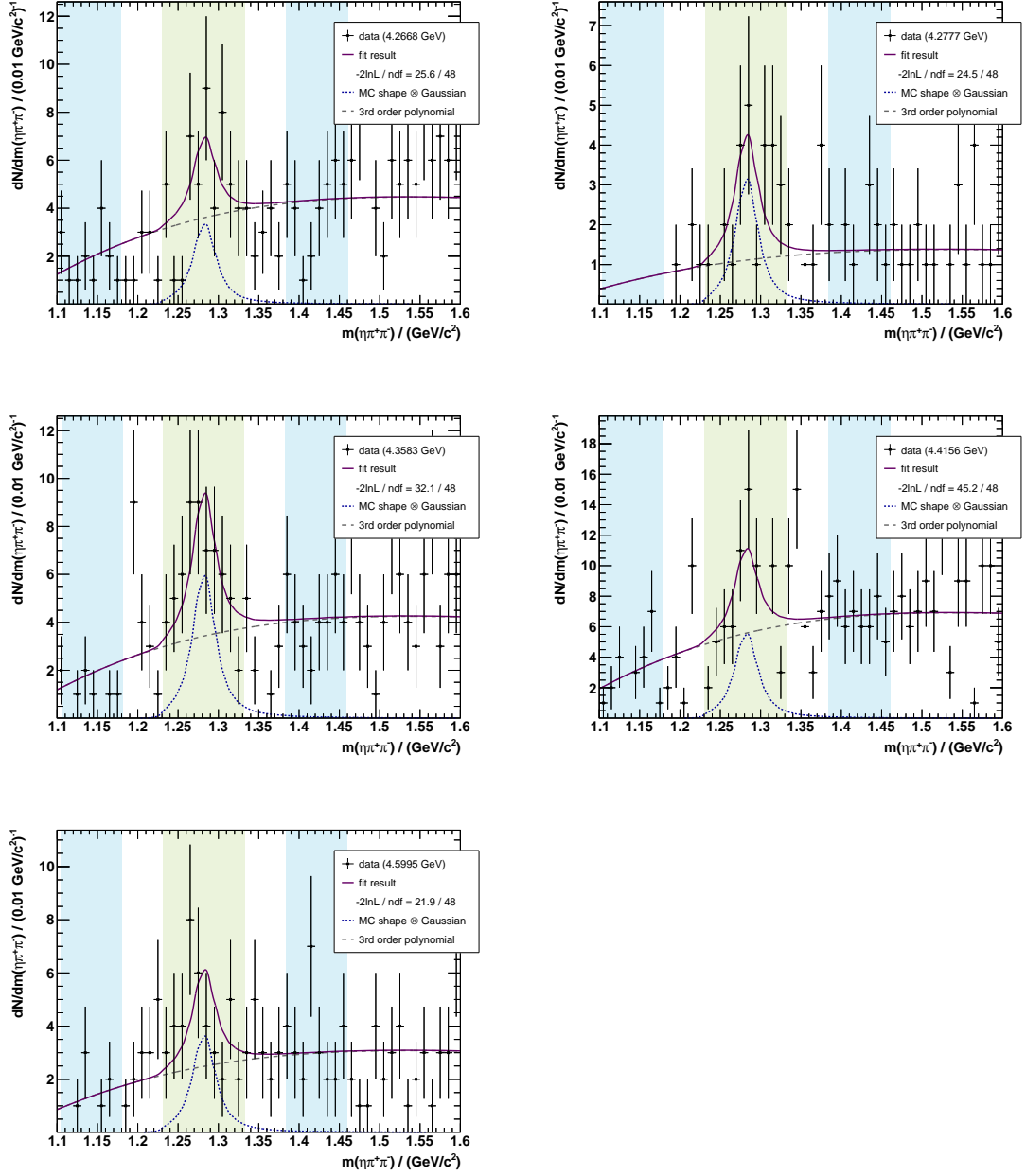


**Figure A.15.:** Invariant mass of the  $\eta\pi^+\pi^-$  system in the reconstruction of  $p\bar{p}f_1$  for center-of-mass energies from 4.2668 GeV to 4.5995 GeV (left to right and top to bottom), fitted with the signal MC shape convolved with a Gaussian and a third order polynomial. Additionally the signal (green) and sideband regions (blue) are shown.



# Bibliography

- [1] J. J. Thomson, “On bodies smaller than atoms,” *The Popular Science Monthly* **59** (1901) 323–335.
- [2] E. Rutherford, “The scattering of alpha and beta particles by matter and the structure of the atom,” *Phil. Mag. Ser.6* **21** (1911) 669–688.
- [3] J. Chadwick, “The Existence of a Neutron,” *Proc. Roy. Soc. Lond.* **A136** no. 830, (1932) 692–708.
- [4] M. Gell-Mann, “A Schematic Model of Baryons and Mesons,” *Phys. Lett.* **8** (1964) 214–215.
- [5] A. Einstein, “Die Grundlage der allgemeinen Relativitätstheorie,” *Annalen Phys.* **49** no. 7, (1916) 769–822.
- [6] **LIGO Scientific, Virgo** Collaboration, B. P. Abbott *et al.*, “Observation of Gravitational Waves from a Binary Black Hole Merger,” *Phys. Rev. Lett.* **116** no. 6, (2016) 061102, [arXiv:1602.03837 \[gr-qc\]](#).
- [7] **SLAC-SP-017** Collaboration, J. E. Augustin *et al.*, “Discovery of a Narrow Resonance in  $e^+e^-$  Annihilation,” *Phys. Rev. Lett.* **33** (1974) 1406–1408. [Adv. Exp. Phys.5,141(1976)].
- [8] **E598** Collaboration, J. J. Aubert *et al.*, “Experimental Observation of a Heavy Particle J,” *Phys. Rev. Lett.* **33** (1974) 1404–1406.
- [9] **Belle** Collaboration, S. K. Choi *et al.*, “Observation of a narrow charmonium-like state in exclusive  $B^\pm \rightarrow K^\pm \pi^+ \pi^- J/\psi$  decays,” *Phys. Rev. Lett.* **91** (2003) 262001, [arXiv:hep-ex/0309032 \[hep-ex\]](#).
- [10] **BaBar** Collaboration, B. Aubert *et al.*, “Observation of a broad structure in the  $\pi^+ \pi^- J/\psi$  mass spectrum around 4.26 GeV/c<sup>2</sup>,” *Phys. Rev. Lett.* **95** (2005) 142001, [arXiv:hep-ex/0506081 \[hep-ex\]](#).
- [11] **BESIII** Collaboration, M. Ablikim *et al.*, “Observation of a Charged Charmoniumlike Structure in  $e^+e^- \rightarrow \pi^+ \pi^- J/\psi$  at  $\sqrt{s} = 4.26$  GeV,” *Phys. Rev. Lett.* **110** (2013) 252001, [arXiv:1303.5949 \[hep-ex\]](#).

- [12] **Belle** Collaboration, Z. Q. Liu *et al.*, “Study of  $e^+e^- \rightarrow \pi^+\pi^- J/\psi$  and Observation of a Charged Charmoniumlike State at Belle,” *Phys. Rev. Lett.* **110** (2013) 252002, [arXiv:1304.0121](#) [hep-ex].
- [13] F. E. Close and P. R. Page, “Gluonic charmonium resonances at BaBar and BELLE?,” *Phys. Lett.* **B628** (2005) 215–222, [arXiv:hep-ph/0507199](#) [hep-ph].
- [14] S.-L. Zhu, “The Possible interpretations of  $Y(4260)$ ,” *Phys. Lett.* **B625** (2005) 212, [arXiv:hep-ph/0507025](#) [hep-ph].
- [15] D. Ebert, R. N. Faustov, and V. O. Galkin, “Masses of heavy tetraquarks in the relativistic quark model,” *Phys. Lett.* **B634** (2006) 214–219, [arXiv:hep-ph/0512230](#) [hep-ph].
- [16] L. Maiani, V. Riquer, F. Piccinini, and A. D. Polosa, “Four quark interpretation of  $Y(4260)$ ,” *Phys. Rev.* **D72** (2005) 031502, [arXiv:hep-ph/0507062](#) [hep-ph].
- [17] X. Liu, X.-Q. Zeng, and X.-Q. Li, “Possible molecular structure of the newly observed  $Y(4260)$ ,” *Phys. Rev.* **D72** (2005) 054023, [arXiv:hep-ph/0507177](#) [hep-ph].
- [18] C.-F. Qiao, “One explanation for the exotic state  $Y(4260)$ ,” *Phys. Lett.* **B639** (2006) 263–265, [arXiv:hep-ph/0510228](#) [hep-ph].
- [19] Q. Wang, C. Hanhart, and Q. Zhao, “Decoding the riddle of  $Y(4260)$  and  $Z_c(3900)$ ,” *Phys. Rev. Lett.* **111** no. 13, (2013) 132003, [arXiv:1303.6355](#) [hep-ph].
- [20] **BESIII** Collaboration, M. Ablikim *et al.*, “Precise measurement of the  $e^+e^- \rightarrow \pi^+\pi^- J/\psi$  cross section at center-of-mass energies from 3.77 to 4.60 GeV,” *Phys. Rev. Lett.* **118** no. 9, (2017) 092001, [arXiv:1611.01317](#) [hep-ex].
- [21] **BESIII** Collaboration, M. Ablikim *et al.*, “Measurement of  $e^+e^- \rightarrow \pi^+\pi^-\psi(3686)$  from 4.008 to 4.600 GeV and observation of a charged structure in the  $\pi^\pm\psi(3686)$  mass spectrum,” *Phys. Rev.* **D96** no. 3, (2017) 032004, [arXiv:1703.08787](#) [hep-ex]. [erratum: *Phys. Rev.* **D99**, no. 1, 019903(2019)].
- [22] **BESIII** Collaboration, M. Ablikim *et al.*, “Evidence of Two Resonant Structures in  $e^+e^- \rightarrow \pi^+\pi^- h_c$ ,” *Phys. Rev. Lett.* **118** no. 9, (2017) 092002, [arXiv:1610.07044](#) [hep-ex].
- [23] **BESIII** Collaboration, M. Ablikim *et al.*, “Study of  $e^+e^- \rightarrow \omega\chi_{cJ}$  at center-of-mass energies from 4.21 to 4.42 GeV,” *Phys. Rev. Lett.* **114** no. 9, (2015) 092003, [arXiv:1410.6538](#) [hep-ex].

- 
- [24] **BESIII** Collaboration, M. Ablikim *et al.*, “Evidence of a resonant structure in the  $e^+e^- \rightarrow \pi^+D^0D^{*-}$  cross section between 4.05 and 4.60 GeV,” *Phys. Rev. Lett.* **122** no. 10, (2019) 102002, [arXiv:1808.02847 \[hep-ex\]](#).
  - [25] **CLEO** Collaboration, Q. He *et al.*, “Confirmation of the  $Y(4260)$  resonance production in ISR,” *Phys. Rev.* **D74** (2006) 091104, [arXiv:hep-ex/0611021 \[hep-ex\]](#).
  - [26] **Belle** Collaboration, C. Z. Yuan *et al.*, “Measurement of  $e^+e^- \rightarrow \pi^+\pi^-J/\psi$  cross-section via initial state radiation at Belle,” *Phys. Rev. Lett.* **99** (2007) 182004, [arXiv:0707.2541 \[hep-ex\]](#).
  - [27] **BaBar** Collaboration, J. P. Lees *et al.*, “Study of the reaction  $e^+e^- \rightarrow J/\psi\pi^+\pi^-$  via initial-state radiation at BaBar,” *Phys. Rev.* **D86** (2012) 051102, [arXiv:1204.2158 \[hep-ex\]](#).
  - [28] **Belle** Collaboration, K. Abe *et al.*, “Measurement of the near-threshold  $e^+e^- \rightarrow D^{(*)\pm}D^{(*)\mp}$  cross section using initial-state radiation,” *Phys. Rev. Lett.* **98** (2007) 092001, [arXiv:hep-ex/0608018 \[hep-ex\]](#).
  - [29] **BaBar** Collaboration, B. Aubert *et al.*, “Measurements of  $e^+e^- \rightarrow K^+K^-\eta$ ,  $K^+K^-\pi^0$  and  $K_s^0K^\pm\pi^\mp$  cross-sections using initial state radiation events,” *Phys. Rev.* **D77** (2008) 092002, [arXiv:0710.4451 \[hep-ex\]](#).
  - [30] **BaBar** Collaboration, B. Aubert *et al.*, “A Structure at 2175 MeV in  $e^+e^- \rightarrow \phi f_0(980)$  Observed via Initial-State Radiation,” *Phys. Rev.* **D74** (2006) 091103, [arXiv:hep-ex/0610018 \[hep-ex\]](#).
  - [31] **Belle** Collaboration, X. L. Wang, Y. L. Han, C. Z. Yuan, C. P. Shen, and P. Wang, “Observation of  $\psi(4040)$  and  $\psi(4160)$  decay into  $\eta J/\psi$ ,” *Phys. Rev.* **D87** no. 5, (2013) 051101, [arXiv:1210.7550 \[hep-ex\]](#).
  - [32] **BESIII** Collaboration, M. Ablikim *et al.*, “Observation of  $e^+e^- \rightarrow \eta J/\psi$  at center-of-mass energy  $\sqrt{s} = 4.009$  GeV,” *Phys. Rev.* **D86** (2012) 071101, [arXiv:1208.1857 \[hep-ex\]](#).
  - [33] **BESIII** Collaboration, M. Ablikim *et al.*, “Measurement of the  $e^+e^- \rightarrow \eta J/\psi$  cross section and search for  $e^+e^- \rightarrow \pi^0 J/\psi$  at center-of-mass energies between 3.810 and 4.600 GeV,” *Phys. Rev.* **D91** no. 11, (2015) 112005, [arXiv:1503.06644 \[hep-ex\]](#).
  - [34] A. Einstein, “Die Feldgleichungen der Gravitation,” *Sitzungsberichte der Königlich Preußischen Akademie der Wissenschaften* (1915) 844–847.

- [35] G. Altarelli, “The Standard model of particle physics,” `arXiv:hep-ph/0510281` [hep-ph].
- [36] **Particle Data Group** Collaboration, M. Tanabashi *et al.*, “Review of Particle Physics,” *Phys. Rev.* **D98** no. 3, (2018) 030001.
- [37] S. N. Bose, “Planck’s law and light quantum hypothesis,” *Z. Phys.* **26** (1924) 178–181.
- [38] W. Pauli, “The Connection Between Spin and Statistics,” *Phys. Rev.* **58** (1940) 716–722.
- [39] P. A. M. Dirac, “On the Theory of quantum mechanics,” *Proc. Roy. Soc. Lond.* **A112** (1926) 661–677.
- [40] E. Fermi, “On the Quantization of the Monoatomic Ideal Gas,” `arXiv:cond-mat/9912229` [cond-mat.stat-mech].
- [41] M. E. Peskin and D. V. Schroeder, *An Introduction To Quantum Field Theory*. Westview Press, 1995.
- [42] S. Tomonaga, “On a relativistically invariant formulation of the quantum theory of wave fields,” *Prog. Theor. Phys.* **1** (1946) 27–42.
- [43] J. S. Schwinger, “On Quantum electrodynamics and the magnetic moment of the electron,” *Phys. Rev.* **73** (1948) 416–417.
- [44] J. S. Schwinger, “Quantum Electrodynamics. I A Covariant Formulation,” *Phys. Rev.* **74** (1948) 1439. [,36(1948)].
- [45] R. P. Feynman, “The Theory of positrons,” *Phys. Rev.* **76** (1949) 749–759. [,88(1949)].
- [46] R. P. Feynman, “Space - time approach to quantum electrodynamics,” *Phys. Rev.* **76** (1949) 769–789. [,99(1949)].
- [47] R. P. Feynman, “Mathematical formulation of the quantum theory of electromagnetic interaction,” *Phys. Rev.* **80** (1950) 440–457. [,198(1950)].
- [48] S. L. Glashow, “The renormalizability of vector meson interactions,” *Nucl. Phys.* **10** (1959) 107–117.
- [49] A. Salam and J. C. Ward, “Weak and electromagnetic interactions,” *Nuovo Cim.* **11** (1959) 568–577.
- [50] S. Weinberg, “A Model of Leptons,” *Phys. Rev. Lett.* **19** (1967) 1264–1266.

- 
- [51] F. Englert and R. Brout, “Broken Symmetry and the Mass of Gauge Vector Mesons,” *Phys. Rev. Lett.* **13** (1964) 321–323. [,157(1964)].
- [52] P. W. Higgs, “Broken Symmetries and the Masses of Gauge Bosons,” *Phys. Rev. Lett.* **13** (1964) 508–509. [,160(1964)].
- [53] **ATLAS** Collaboration, G. Aad *et al.*, “Observation of a new particle in the search for the Standard Model Higgs boson with the ATLAS detector at the LHC,” *Phys. Lett.* **B716** (2012) 1–29, [arXiv:1207.7214 \[hep-ex\]](#).
- [54] **CMS** Collaboration, S. Chatrchyan *et al.*, “Observation of a new boson at a Mass of 125 GeV with the CMS Experiment at the LHC,” *Phys. Lett.* **B716** (2012) 30–61, [arXiv:1207.7235 \[hep-ex\]](#).
- [55] D. J. Gross and F. Wilczek, “Ultraviolet Behavior of Nonabelian Gauge Theories,” *Phys. Rev. Lett.* **30** (1973) 1343–1346. [,271(1973)].
- [56] H. D. Politzer, “Reliable Perturbative Results for Strong Interactions?,” *Phys. Rev. Lett.* **30** (1973) 1346–1349. [,274(1973)].
- [57] R. Oerter, *The Theory of Almost Everything: The Standard Model, the Unsung Triumph of Modern Physics*. Plume, 2006.
- [58] **Super-Kamiokande** Collaboration, Y. Fukuda *et al.*, “Evidence for oscillation of atmospheric neutrinos,” *Phys. Rev. Lett.* **81** (1998) 1562–1567, [arXiv:hep-ex/9807003 \[hep-ex\]](#).
- [59] V. Trimble, “Existence and Nature of Dark Matter in the Universe,” *Ann. Rev. Astron. Astrophys.* **25** (1987) 425–472.
- [60] V. C. Rubin and W. K. Ford, Jr., “Rotation of the Andromeda Nebula from a Spectroscopic Survey of Emission Regions,” *Astrophys. J.* **159** (1970) 379–403.
- [61] E. Aubourg *et al.*, “Evidence for gravitational microlensing by dark objects in the galactic halo,” *Nature* **365** (1993) 623–625.
- [62] **HPQCD, UKQCD, MILC, Fermilab Lattice** Collaboration, C. T. H. Davies *et al.*, “High precision lattice QCD confronts experiment,” *Phys. Rev. Lett.* **92** (2004) 022001, [arXiv:hep-lat/0304004 \[hep-lat\]](#).
- [63] P. Colangelo and A. Khodjamirian, “QCD sum rules, a modern perspective,” [arXiv:hep-ph/0010175 \[hep-ph\]](#).
- [64] V. Crede and W. Roberts, “Progress towards understanding baryon resonances,” *Rept. Prog. Phys.* **76** (2013) 076301, [arXiv:1302.7299 \[nucl-ex\]](#).

- [65] S. Okubo, “ $\varphi$ -meson and unitary symmetry model,” *Phys. Lett.* **5** (1963) 165–168.
- [66] G. Zweig, “An SU(3) model for strong interaction symmetry and its breaking. Version 1,”.
- [67] G. Zweig, “An SU(3) model for strong interaction symmetry and its breaking. Version 2,” in *Developments in the Quark Theory of Hadrons, Volume 1. 1964 - 1978*, D. Lichtenberg and S. P. Rosen, eds., pp. 22–101. 1964.
- [68] J. Iizuka, “Systematics and phenomenology of meson family,” *Prog. Theor. Phys. Suppl.* **37** (1966) 21–34.
- [69] Institute of High Energy Physics, CAS, “BESIII Accumulates 10 Billion J/ $\psi$  events,” 2019. <http://english.ihep.cas.cn/bes/doc/3314.html>. found online on 10-14-2019 17:43.
- [70] T. Barnes, S. Godfrey, and E. S. Swanson, “Higher charmonia,” *Phys. Rev.* **D72** (2005) 054026, [arXiv:hep-ph/0505002](#) [hep-ph].
- [71] G.-J. Ding, “Are  $Y(4260)$  and  $Z_2^+ D_1 D$  or  $D_0 D^*$  hadronic molecules?,” *Phys. Rev.* **D79** (2009) 014001, [arXiv:0809.4818](#) [hep-ph].
- [72] L. Y. Dai, M. Shi, G.-Y. Tang, and H. Q. Zheng, “Nature of  $X(4260)$ ,” *Phys. Rev.* **D92** no. 1, (2015) 014020, [arXiv:1206.6911](#) [hep-ph].
- [73] D.-Y. Chen, J. He, and X. Liu, “Nonresonant explanation for the  $Y(4260)$  structure observed in the  $e^+e^- \rightarrow J/\psi \pi^+ \pi^-$  process,” *Phys. Rev.* **D83** (2011) 054021, [arXiv:1012.5362](#) [hep-ph].
- [74] N. Brambilla, S. Eidelman, C. Hanhart, A. Nefediev, C.-P. Shen, C. E. Thomas, A. Vairo, and C.-Z. Yuan, “The  $XYZ$  states: experimental and theoretical status and perspectives,” [arXiv:1907.07583](#) [hep-ex].
- [75] Y.-R. Liu, H.-X. Chen, W. Chen, X. Liu, and S.-L. Zhu, “Pentaquark and Tetraquark states,” *Prog. Part. Nucl. Phys.* **107** (2019) 237–320, [arXiv:1903.11976](#) [hep-ph].
- [76] D. M. Asner *et al.*, “Physics at BES-III,” *Int. J. Mod. Phys.* **A24** (2009) S1–794, [arXiv:0809.1869](#) [hep-ex].
- [77] C. Zhang, L. Ma, G. Pei, and J. Wang, “Construction and Commissioning of BEPCII,” in *Particle accelerator. Proceedings, 23rd Conference, PAC’09, Vancouver, Canada, May 4-8, 2009*, p. MO3RAI03. 2010. <http://accelconf.web.cern.ch/AccelConf/PAC2009/papers/mo3rai03.pdf>.



- 
- [78] **BESIII** Collaboration, M. Ablikim *et al.*, “Design and Construction of the BESIII Detector,” *Nucl. Instrum. Meth.* **A614** (2010) 345–399, [arXiv:0911.4960 \[physics.ins-det\]](#).
  - [79] Institute of High Energy Physics, CAS, “Photo/Video Gallery,” 2019. <http://english.ihep.cas.cn/bes/chnl/132/index.html>. found online on 10-14-2019 17:43.
  - [80] Institute of High Energy Physics, CAS, “BEPC & BEPCII,” 2019. <http://english.ihep.cas.cn/doc/1840.html>. found online on 10-16-2019 14:47.
  - [81] Q. Gang *et al.*, “Particle identification using artificial neural networks at BESIII,” *Chin. Phys.* **C32** (2008) 001.
  - [82] Y. Guan, X.-R. Lü, Y. Zheng, and Y.-F. Wang, “Study of the efficiency of event start time determination at BESIII,” *Chin. Phys.* **C38** no. 1, (2014) 016201, [arXiv:1304.6177 \[physics.ins-det\]](#).
  - [83] C.-Z. Yuan and S. L. Olsen, “The BESIII physics programme,” *Nature Rev. Phys.* **1** no. 8, (2019) 480–494.
  - [84] **BESIII** Collaboration, M. Ablikim, “Measurement of the integrated luminosities of the data taken by BESIII at  $\sqrt{s} = 3.650$  and  $3.773$  GeV,” *Chin. Phys.* **C37** (2013) 123001, [arXiv:1307.2022 \[hep-ex\]](#).
  - [85] **BESIII** Collaboration, M. Ablikim *et al.*, “Measurement of the center-of-mass energies at BESIII via the di-muon process,” *Chin. Phys.* **C40** no. 6, (2016) 063001, [arXiv:1510.08654 \[hep-ex\]](#).
  - [86] **BESIII** Collaboration, M. Ablikim *et al.*, “Study of  $e^+e^- \rightarrow \gamma\omega J/\psi$  and Observation of  $X(3872) \rightarrow \omega J/\psi$ ,” *Phys. Rev. Lett.* **122** no. 23, (2019) 232002, [arXiv:1903.04695 \[hep-ex\]](#).
  - [87] **BESIII** Collaboration, M. Ablikim *et al.*, “Cross section measurements of  $e^+e^- \rightarrow p\bar{p}\pi^0$  at center-of-mass energies between 4.008 and 4.600 GeV,” *Phys. Lett.* **B771** (2017) 45–51, [arXiv:1701.04198 \[hep-ex\]](#).
  - [88] **BESIII** Collaboration, M. Ablikim *et al.*, “Precision measurement of the integrated luminosity of the data taken by BESIII at center of mass energies between 3.810 GeV and 4.600 GeV,” *Chin. Phys.* **C39** no. 9, (2015) 093001, [arXiv:1503.03408 \[hep-ex\]](#).
  - [89] W.-D. Li, Y.-J. Mao, and Y.-F. Wang, “The BES-III detector and offline software,” *Int. J. Mod. Phys.* **A24S1** (2009) 9–21.

- [90] G. Barrand *et al.*, “GAUDI - A software architecture and framework for building HEP data processing applications,” *Comput. Phys. Commun.* **140** (2001) 45–55.
- [91] **GEANT4** Collaboration, S. Agostinelli *et al.*, “GEANT4: A Simulation toolkit,” *Nucl. Instrum. Meth.* **A506** (2003) 250–303.
- [92] Z.-Y. DENG *et al.*, “Object-Oriented BESIII Detector Simulation System,” *Chin. Phys.* **C30** (2006) 006.
- [93] R.-G. Ping *et al.*, “Tuning and validation of hadronic event generator for  $R$  value measurements in the tau-charm region,” *Chin. Phys.* **C40** no. 11, (2016) 113002, [arXiv:1605.09208 \[hep-ex\]](#).
- [94] R.-G. Ping, “Event generators at BESIII,” *Chin. Phys.* **C32** (2008) 599.
- [95] D. J. Lange, “The EvtGen particle decay simulation package,” *Nucl. Instrum. Meth.* **A462** (2001) 152–155.
- [96] S. Jadach, B. F. L. Ward, and Z. Was, “The Precision Monte Carlo event generator KK for two fermion final states in  $e^+e^-$  collisions,” *Comput. Phys. Commun.* **130** (2000) 260–325, [arXiv:hep-ph/9912214 \[hep-ph\]](#).
- [97] B. Andersson, G. Gustafson, G. Ingelman, and T. Sjostrand, “Parton Fragmentation and String Dynamics,” *Phys. Rept.* **97** (1983) 31–145.
- [98] B. Andersson and H.-m. Hu, “Few body states in Lund string fragmentation model,” [arXiv:hep-ph/9910285 \[hep-ph\]](#).
- [99] J.-K. Wang *et al.*, “BESIII track fitting algorithm,” *Chin. Phys.* **C33** (2009) 870–879.
- [100] R. E. Kalman, “A New Approach to Linear Filtering and Prediction Problems,” *Journal of Basic Engineering* **82** (1960) 35–45.
- [101] X.-H. Sun *et al.*, “Track segment finding with CGEM-IT and matching to outer drift chamber tracks in the BESIII detector,” *Chin. Phys.* **C40** no. 9, (2016) 096203, [arXiv:1604.03102 \[physics.ins-det\]](#).
- [102] C. M. Bishop, *Neural Networks for Pattern Recognition*. Oxford University Press, USA, 1996.
- [103] R. Brun and F. Rademakers, “ROOT: An object oriented data analysis framework,” *Nucl. Instrum. Meth.* **A389** (1997) 81–86.

- 
- [104] I. Antcheva *et al.*, “ROOT: A C++ framework for petabyte data storage, statistical analysis and visualization,” *Comput. Phys. Commun.* **182** (2011) 1384–1385.
  - [105] L. Yan *et al.*, “Lagrange multiplier method used in BESIII kinematic fitting,” *Chin. Phys.* **C34** (2010) 204–209.
  - [106] **BaBar** Collaboration, B. Aubert *et al.*, “A Study of  $e^+e^- \rightarrow p\bar{p}$  using initial state radiation with BABAR,” *Phys. Rev.* **D73** (2006) 012005, [arXiv:hep-ex/0512023 \[hep-ex\]](#).
  - [107] **BESIII** Collaboration, M. Ablikim *et al.*, “Study of the process  $e^+e^- \rightarrow p\bar{p}$  via initial state radiation at BESIII,” *Phys. Rev.* **D99** no. 9, (2019) 092002, [arXiv:1902.00665 \[hep-ex\]](#).
  - [108] F. James and M. Roos, “Minuit: A System for Function Minimization and Analysis of the Parameter Errors and Correlations,” *Comput. Phys. Commun.* **10** (1975) 343–367.
  - [109] D. J. Griffiths, *Introduction to Quantum Mechanics*. Cambridge University Press, 2017.
  - [110] K. J. Peters, “A Primer on partial wave analysis,” *Int. J. Mod. Phys.* **A21** (2006) 5618–5624, [arXiv:hep-ph/0412069 \[hep-ph\]](#). [,451(2004)].
  - [111] S. U. Chung, “Spin formalisms,” *CERN-71-08* (1971).
  - [112] J. D. Richman, “An Experimenter’s Guide to the Helicity Formalism,”.
  - [113] **Crystal Barrel** Collaboration, C. Amsler, F. H. Heinsius, H. Koch, B. Kopf, U. Kurilla, C. A. Meyer, K. Peters, J. Pychy, M. Steinke, and U. Wiedner, “Spin Density Matrix of the  $\omega$  in the Reaction  $\bar{p}p \rightarrow \omega\pi^0$ ,” *Eur. Phys. J.* **C75** no. 3, (2015) 124, [arXiv:1410.3743 \[hep-ex\]](#).
  - [114] S. U. Chung, “Formulas for Angular-Momentum Barrier Factors,” *BNL-QGS-06-101* (2015).
  - [115] B. Kopf, H. Koch, J. Pychy, and U. Wiedner, “Partial wave analysis for  $\bar{p}p$  and  $e^+e^-$  annihilation processes,” *Hyperfine Interact.* **229** no. 1-3, (2014) 69–74.
  - [116] M. Williams, “Numerical Object Oriented Quantum Field Theory Calculations,” *Comput. Phys. Commun.* **180** (2009) 1847–1852, [arXiv:0805.2956 \[hep-ph\]](#).
  - [117] F. Jegerlehner, “Electroweak effective couplings for future precision experiments,” *Nuovo Cim.* **C034S1** (2011) 31–40, [arXiv:1107.4683 \[hep-ph\]](#).

- [118] W.-L. Yuan, X.-C. Ai, X.-B. Ji, S.-J. Chen, Y. Zhang, L.-H. Wu, L.-L. Wang, and Y. Yuan, “Study of tracking efficiency and its systematic uncertainty from  $J/\psi \rightarrow p\bar{p}\pi^+\pi^-$  at BESIII,” *Chin. Phys.* **C40** no. 2, (2016) 026201, [arXiv:1507.03453 \[hep-ex\]](#).
- [119] **BESIII** Collaboration, M. Ablikim *et al.*, “Branching fraction measurements of  $\chi_{c0}$  and  $\chi_{c2}$  to  $\pi^0\pi^0$  and  $\eta\eta$ ,” *Phys. Rev.* **D81** (2010) 052005, [arXiv:1001.5360 \[hep-ex\]](#).
- [120] **BESIII** Collaboration, M. Ablikim *et al.*, “Study of  $\psi(3686) \rightarrow \pi^0 h_c, h_c \rightarrow \gamma\eta_c$  via  $\eta_c$  exclusive decays,” *Phys. Rev.* **D86** (2012) 092009, [arXiv:1209.4963 \[hep-ex\]](#).
- [121] C. Rover, C. Messenger, and R. Prix, “Bayesian versus frequentist upper limits,” in *Proceedings, PHYSTAT 2011 Workshop on Statistical Issues Related to Discovery Claims in Search Experiments and Unfolding, CERN, Geneva, Switzerland 17-20 January 2011*, pp. 158–163, CERN. CERN, Geneva, 2011. [arXiv:1103.2987 \[physics.data-an\]](#).
- [122] A. Gelman, J. B. Carlin, H. S. Stern, D. B. Dunson, A. Vehtari, and D. B. Rubin, *Bayesian Data Analysis*. Chapman and Hall/CRC, 2013.
- [123] K. Zhu, X. H. Mo, C. Z. Yuan, and P. Wang, “A mathematical review on the multiple-solution problem,” *Int. J. Mod. Phys.* **A26** (2011) 4511–4520, [arXiv:1108.2760 \[hep-ex\]](#).
- [124] **BESIII** Collaboration, M. Ablikim *et al.*, “Cross section measurement of  $e^+e^- \rightarrow \eta'J/\psi$  from  $\sqrt{s} = 4.178$  to 4.600 GeV,” [arXiv:1911.00885 \[hep-ex\]](#).
- [125] Q.-Y. Lin, H.-S. Xu, and X. Liu, “Revisiting the production of charmonium plus a light meson at PANDA,” *Phys. Rev.* **D86** (2012) 034007, [arXiv:1203.4029 \[hep-ph\]](#).

# List of Figures

2.1. Schematic illustration of the Standard Model of Particle Physics. . . . .	6
2.2. Schematic representation of the nonet of pseudoscalar mesons. . . . .	10
2.3. Schematic representation of the baryon decuplet and the baryon octet. . .	12
2.4. Schematic representation of the charmonium spectrum. . . . .	14
3.1. Pictures of the BESIII and BEPCII facilities. . . . .	18
3.2. Schematic drawing of the BESIII detector. . . . .	19
3.3. Visualization of the tracking system and particle identification by $dE/dx$ measurement. . . . .	20
3.4. Expected $\pi/K$ misidentification rate and separation efficiency of the time-of-flight system. . . . .	22
3.5. Energy resolution and particle identification capabilities of the EMC. . .	23
4.1. Luminosities of various BESIII data sets at center-of-mass energies above 3.7 GeV . . . . .	26
4.2. Illustration of the vertex fit for two charged tracks. . . . .	28
5.1. Invariant mass distributions of the $\eta$ and $\omega$ systems, summed up over 17 data samples. . . . .	32
5.2. Invariant mass distribution of the $\pi^+\pi^-\pi^0$ and $\rho\omega$ systems for the reconstructed decay $\omega \rightarrow \pi^+\pi^-\pi^0$ . . . . .	33
5.3. Invariant mass distribution of the $\eta$ and $\rho\eta$ systems for three reconstructed $\eta$ meson decay modes. . . . .	34
5.4. Invariant mass and $\chi^2$ distributions of three light meson decay modes: $\eta \rightarrow \gamma\gamma$ , $\eta \rightarrow \pi^+\pi^-\pi^0$ and $\omega \rightarrow \pi^+\pi^-\pi^0$ . . . . .	37
5.5. Invariant mass distributions of the $\eta$ and $\omega$ meson decay systems after applying all selection criteria, summed up over all 17 data samples. . . .	39
5.6. Invariant mass of the meson system in the reconstruction of the $\eta$ and $\omega$ mesons. . . . .	41
5.7. Efficiencies of the $\eta \rightarrow \gamma\gamma$ , $\eta \rightarrow \pi^+\pi^-\pi^0$ and $\omega \rightarrow \pi^+\pi^-\pi^0$ decay modes determined with a partial wave analysis or simply using the MC simulations. . . . .	47

5.8. Final results of the partial wave analysis for the $\eta \rightarrow \gamma\gamma$ decay mode at a center-of-mass energy of 3.7730 GeV. . . . .	48
5.9. Final results of the partial wave analysis for the $\eta \rightarrow \gamma\gamma$ decay mode at a center-of-mass energy of 4.1784 GeV. . . . .	49
5.10. Final results of the partial wave analysis for the $\eta \rightarrow \pi^+\pi^-\pi^0$ decay mode at a center-of-mass energy of 3.7730 GeV. . . . .	50
5.11. Final results of the partial wave analysis for the $\eta \rightarrow \pi^+\pi^-\pi^0$ decay mode at a center-of-mass energy of 4.1784 GeV. . . . .	51
5.12. Final results of the partial wave analysis for the $\omega \rightarrow \pi^+\pi^-\pi^0$ decay mode at a center-of-mass energy of 3.7730 GeV. . . . .	52
5.13. Schematic diagrams of the process $e^+e^- \rightarrow p\bar{p}m$ . . . . .	54
5.14. Relative difference of the radiative correction dependent quantity $\kappa$ . . . .	54
5.15. Calculated Born cross sections $\sigma^B$ for the $p\bar{p}\eta$ and $p\bar{p}\omega$ final states with corresponding statistical uncertainties. . . . .	56
5.16. Systematic study of the influence of the $\chi^2$ cut on the final result. . . . .	60
5.17. Systematic study of the arbitrarily chosen signal region confidence level $\alpha_{\text{sr}}$ . . . . .	62
5.18. Systematic study of the radiative correction procedure. . . . .	63
5.19. Systematic study of the remaining background description. . . . .	64
5.20. Born cross section $\sigma^B(e^+e^- \rightarrow \eta J/\psi)$ as available in the literature. . . . .	66
5.21. Non- $\eta$ sideband corrected invariant mass distribution of the $p\bar{p}$ system, summed up over all 17 data samples. . . . .	68
5.22. Born cross sections $\sigma^B(e^+e^- \rightarrow \eta J/\psi)$ and upper limits determined in this work compared to the database available in the literature. . . . .	68
5.23. Born cross sections $\sigma^B$ for the $p\bar{p}\eta$ and $p\bar{p}\omega$ final states, including statistical and systematic uncertainties. . . . .	70
5.24. Likelihood scans of the number of signal events in the invariant mass distributions of the meson system for the $\eta \rightarrow \gamma\gamma$ ( <b>top</b> ), $\eta \rightarrow \pi^+\pi^-\pi^0$ ( <b>middle</b> ) and $\omega \rightarrow \pi^+\pi^-\pi^0$ ( <b>bottom</b> ) decay modes for the high statistics data set at 3.7730 GeV ( <b>left</b> ) and the one with the smallest statistics at 4.2777 GeV ( <b>right</b> ). The asymmetric Gaussian fit results are shown by solid lines. . . . .	72
5.25. Likelihood distribution for a coherent ( <b>left</b> ) and incoherent ( <b>right</b> ) $\psi(4160)$ resonant contribution in the $p\bar{p}\eta$ ( <b>top</b> ) and $p\bar{p}\omega$ ( <b>bottom</b> ) cross section. Upper limits are calculated at 90 % confidence level indicated by dashed lines. Note the special formatting of the x-axis. . . . .	73
5.26. Upper limits for a possible coherent ( <b>left</b> ) and incoherent ( <b>right</b> ) resonant contribution with mass $m$ and width $\Gamma$ in the $p\bar{p}\eta$ ( <b>top</b> ) and $p\bar{p}\omega$ ( <b>bottom</b> ) cross sections. . . . .	76

6.1. Invariant mass distributions of the $\eta'$ and $f_1$ meson systems, summed up over 17 data samples. . . . .	78
6.2. Invariant mass distributions of the $\eta\pi^+\pi^-$ and the $p\bar{m}$ system for the $p\bar{p}\eta'$ and $p\bar{p}f_1$ final states. . . . .	79
6.3. $\chi^2$ and invariant mass distributions of the $\eta\pi^+\pi^-$ system for the $p\bar{p}\eta'$ and $p\bar{p}f_1$ final states. . . . .	80
6.4. Invariant mass distributions of the $\eta'$ and $f_1$ meson decay systems after applying all selection criteria, summed up over all 17 data samples. . . .	82
6.5. Invariant mass of the $\eta\pi^+\pi^-$ system in the reconstruction of the $\eta'$ and $f_1$ mesons. . . . .	83
6.6. Born cross sections $\sigma^B(e^+e^- \rightarrow p\bar{p}\eta')$ and upper limits. . . . .	86
6.7. Born cross sections $\sigma^B(e^+e^- \rightarrow p\bar{p}\eta')$ and upper limits. . . . .	87
7.1. Born cross sections $\sigma^B$ for the $p\bar{p}\eta$ and $p\bar{p}\omega$ final states, including the new high luminosity data samples from the systematic scan in 2019. . . . .	89
A.1. Invariant mass of the $\eta$ system in the reconstruction of $e^+e^- \rightarrow p\bar{p}(\eta \rightarrow \gamma\gamma)$ for center-of-mass energies from 3.7730 GeV to 4.1989 GeV. . . . .	95
A.2. Invariant mass of the $\eta$ system in the reconstruction of $e^+e^- \rightarrow p\bar{p}(\eta \rightarrow \gamma\gamma)$ for center-of-mass energies from 4.2092 GeV to 4.2580 GeV. . . . .	96
A.3. Invariant mass of the $\eta$ system in the reconstruction of $e^+e^- \rightarrow p\bar{p}(\eta \rightarrow \gamma\gamma)$ for center-of-mass energies from 4.2668 GeV to 4.5995 GeV. . . . .	97
A.4. Invariant mass of the $\eta$ system in the reconstruction of $e^+e^- \rightarrow p\bar{p}(\eta \rightarrow \pi^+\pi^-\pi^0)$ for center-of-mass energies from 3.7730 GeV to 4.1989 GeV. . . .	98
A.5. Invariant mass of the $\eta$ system in the reconstruction of $e^+e^- \rightarrow p\bar{p}(\eta \rightarrow \pi^+\pi^-\pi^0)$ for center-of-mass energies from 4.2092 GeV to 4.2580 GeV. . . .	99
A.6. Invariant mass of the $\eta$ system in the reconstruction of $e^+e^- \rightarrow p\bar{p}(\eta \rightarrow \pi^+\pi^-\pi^0)$ for center-of-mass energies from 4.2668 GeV to 4.5995 GeV. . . .	100
A.7. Invariant mass of the $\omega$ system in the reconstruction of $e^+e^- \rightarrow p\bar{p}(\omega \rightarrow \pi^+\pi^-\pi^0)$ for center-of-mass energies from 3.7730 GeV to 4.1989 GeV. . . .	101
A.8. Invariant mass of the $\omega$ system in the reconstruction of $e^+e^- \rightarrow p\bar{p}(\omega \rightarrow \pi^+\pi^-\pi^0)$ for center-of-mass energies from 4.2092 GeV to 4.2580 GeV. . . .	102
A.9. Invariant mass of the $\omega$ system in the reconstruction of $e^+e^- \rightarrow p\bar{p}(\omega \rightarrow \pi^+\pi^-\pi^0)$ for center-of-mass energies from 4.2668 GeV to 4.5995 GeV. . . .	103
A.10. Invariant mass of the $\eta\pi^+\pi^-$ system in the reconstruction of $p\bar{p}\eta'$ for center-of-mass energies from 3.7730 GeV to 4.1989 GeV. . . . .	104
A.11. Invariant mass of the $\eta\pi^+\pi^-$ system in the reconstruction of $p\bar{p}\eta'$ for center-of-mass energies from 4.2092 GeV to 4.2580 GeV. . . . .	105
A.12. Invariant mass of the $\eta\pi^+\pi^-$ system in the reconstruction of $p\bar{p}\eta'$ for center-of-mass energies from 4.2668 GeV to 4.5995 GeV. . . . .	106

A.13.Invariant mass of the $\eta\pi^+\pi^-$ system in the reconstruction of $p\bar{p}f_1$ for center-of-mass energies from 3.7730 GeV to 4.1989 GeV. . . . .	107
A.14.Invariant mass of the $\eta\pi^+\pi^-$ system in the reconstruction of $p\bar{p}f_1$ for center-of-mass energies from 4.2092 GeV to 4.2580 GeV. . . . .	108
A.15.Invariant mass of the $\eta\pi^+\pi^-$ system in the reconstruction of $p\bar{p}f_1$ for center-of-mass energies from 4.2668 GeV to 4.5995 GeV. . . . .	109



# List of Tables

2.1. Additive quantum numbers of the quarks. . . . .	9
2.2. Quark content of the lightest pseudoscalar mesons. . . . .	11
3.1. Relevant operational parameters of BEPCII. . . . .	17
3.2. Expected event rates of the BESIII trigger system. . . . .	24
4.1. Center-of-mass energies and luminosities of the data samples studied in this analysis. . . . .	27
4.2. Branching fractions and reconstruction patterns of the analyzed light hadron final states. . . . .	30
5.1. Topology of events from the generic MC sample at 4.1784 GeV, which survived all selection criteria in the reconstruction of the $p\bar{p}\eta$ final state. . . . .	35
5.2. Topology of events from the generic MC sample at 4.1784 GeV, which survived all selection criteria in the reconstruction of the $p\bar{p}\omega$ final state. . . . .	36
5.3. Blatt-Weisskopf barrier factors for angular momenta up to $L = 4$ . . . . .	45
5.4. List of intermediate resonances with quantum numbers $J^{PC}$ and associated decay particles used in the PWA to describe the $p\bar{p}m$ final states. . . . .	46
5.5. Born cross section $\sigma^B(e^+e^- \rightarrow p\bar{p}\eta)$ for the $\eta \rightarrow \gamma\gamma$ decay mode. . . . .	56
5.6. Born cross section $\sigma^B(e^+e^- \rightarrow p\bar{p}\eta)$ for the $\eta \rightarrow \pi^+\pi^-\pi^0$ decay mode. . . . .	57
5.7. Born cross section $\sigma^B(e^+e^- \rightarrow p\bar{p}\omega)$ for the $\omega \rightarrow \pi^+\pi^-\pi^0$ decay mode. . . . .	58
5.8. Systematic uncertainties in % for the $p\bar{p}\eta$ and $p\bar{p}\omega$ final states, which have been determined in previous works. . . . .	59
5.9. Systematic uncertainties in % dependent on the center-of-mass energy $\sqrt{s}$ in GeV for the $\eta \rightarrow \gamma\gamma$ decay mode. . . . .	64
5.10. Systematic uncertainties in % dependent on the center-of-mass energy $\sqrt{s}$ in GeV for the $\eta \rightarrow \pi^+\pi^-\pi^0$ decay mode. . . . .	65
5.11. Systematic uncertainties in % dependent on the center-of-mass energy $\sqrt{s}$ in GeV for the $\omega \rightarrow \pi^+\pi^-\pi^0$ decay mode. . . . .	65
5.12. Born cross sections $\sigma^B(e^+e^- \rightarrow \eta J/\psi)$ for the $\eta \rightarrow \gamma\gamma$ decay mode. . . . .	69
5.13. Upper limits of the Born cross sections $\sigma^B(e^+e^- \rightarrow \eta J/\psi)$ for the $\eta \rightarrow \gamma\gamma$ decay mode. . . . .	69

5.14. Asymmetric Gaussian parameters $\mu$ , $\sigma_L$ and $\sigma_R$ of fits to the likelihood scans for two $\eta$ meson decay modes. . . . .	74
6.1. Branching fractions for different decay modes of the $\eta'$ and the $f_1(1285)$ meson. . . . .	77
6.2. Topology of events from the generic MC sample at 4.1784 GeV, which survived all selection criteria in the reconstruction of the $p\bar{p}\eta'$ and $p\bar{p}f_1$ final states. . . . .	81
6.3. Born cross section $\sigma^B(e^+e^- \rightarrow p\bar{p}\eta')$ and upper limits. . . . .	84
6.4. Born cross section $\sigma^B(e^+e^- \rightarrow p\bar{p}f_1)$ and upper limits. . . . .	85
7.1. Born cross section $\bar{\sigma}^B(e^+e^- \rightarrow p\bar{p}\eta)$ and $\sigma^B(e^+e^- \rightarrow p\bar{p}\omega)$ for the new high luminosity data samples. . . . .	90

# Acknowledgments

In the last few words of this thesis, I would like to express my warmest gratitude to all those who have contributed to the success of this work.

First, I would like to thank Prof. Dr. Alfons Khoukaz for the possibility to be a member of his group for more than six years now. From my BSc and MSc thesis at the ANKE experiment, to opening a completely new chapter with exciting analyses at BESIII. It was an amazing journey, not only because of our trips to Beijing. Thank you for your guidance, support and patience wherever it was needed.

I would like to thank Prof. Dr. Anton Andronic and Prof. Dr. Jochen Heitger for taking over the responsibility as second and third examiner for my dissertation.

I would like to thank all the people of our incredible working group, past and present, Florian, Johannes B., Matthias B., Philipp, Anja, Kay, Hanna, Birte, Michael E., Lukas F., Julia, Cristopher, Paul, Silke, Daniel G., Laura, Catharina, Ann-Katrin, Benjamin, Patrice, Nils, Hamza, Johannes K., Daniel K., Esperanza, David, Sascha, Lukas L., Christian, Malte, Michael P., Salleh, Daniel S., Matthias S., Karsten, Julian, Lana, Alexander, Sophia, Frederik, Christina and Lisa. A special thanks to Nils for proof-reading all of this and being part an unforgettable trip through China. I hope you guys will enjoy future visits as much as i did. Ho.

Last but not least I would like to thank my whole family who always supported me in doing what I believed I had to do. Especially my wife, without her none of this would have been possible. Thank you for always standing up for me and making me the person I am today. I love you.



# Curriculum Vitæ

---

## Personal Details

First Name Marcel Andre  
Last Name Rump  
Date of Birth February 9th, 1991  
Place of Birth Münster, Germany  
Nationality German

## Academic Education

since 2016 **Doctoral Studies**, *Westfälische Wilhelms-Universität, Münster.*  
2013–2016 **Master of Science**, *Westfälische Wilhelms-Universität, Münster.*  
*The quasi-free two-pion production reaction  $pd \rightarrow d\pi^+\pi^- p_{spec}$  at ANKE*  
2010–2013 **Bachelor of Science**, *Westfälische Wilhelms-Universität, Münster.*  
*Identification of deuterons in proton-deuteron collisions at the ANKE experiment*

## School Education

2001–2010 Secondary School Immanuel Kant Gymnasium Münster  
2000–2001 Elementary School Ludgerusschule Hilstrup  
1997–2000 Elementary School Nikolaischule Wolbeck

## Working Experience

since 2016 **Research Assistant**, *Westfälische Wilhelms-Universität, Münster.*  
2011–2013 **Student Assistant**, *Westfälische Wilhelms-Universität, Münster.*

## Teaching Experience

2016–2019 Supervisor of the Advanced Laboratory Course *Gas detectors*  
2016–2018 Supervisor of two Bachelor- and two Master-Students during their thesis  
2011–2013 Supervisor of Student Learning Groups in *Physics I + II*

